Characterisation and Modelling of Brush Contacts

Vom Fachbereich Elektrotechnik
der
Helmut-Schmidt-Universität /
Universität der Bundeswehr Hamburg
zur Erlangung des akademischen Grades eines
Doktor-Ingenieurs
genehmigte

DISSERTATION
vorgelegt von

Marcos Fraile Gómez

aus Huesca (Spanien)

Hamburg 2005

Gutachter:
Prof. Dr.-Ing. Stefan Dickmann
Prof. Dr. rer. nat. Günter Guthöhrlein

Tag der mündlichen Prüfung: 14.06.2005

Danksagung

Die vorliegende Arbeit entstand während meiner Tätigkeit als freier Mitarbeiter der Robert Bosch GmbH in Stuttgart und in Zusammenarbeit mit der Fakultät für Elektrotechnik der Helmut-Schmidt-Universität (Universität der Bundeswehr Hamburg).

Allen, die zum Gelingen dieser Arbeit beigetragen haben, möchte ich an dieser Stelle herzlich danken.

Mein besonderer Dank gilt:

Herrn Prof. Dr.-Ing. S. Dickmann für die Betreuung dieser Arbeit, die hilfreiche Unterstützung und die Übernahme des Referats,

Herrn Prof. Dr. G. Guthöhrlein für die bereitwillige Übernahme des Korreferats,

Frau Dr.-Ing. S. Frohnert für die bereitwillige Übernahme der fachlichen Betreuung sowie für die konstruktiven Diskussionen, Verbesserungsvorschläge, und die Durchsicht des Manuskripts,

Herrn Dr.-Ing. M. Sinner-Hettenbach für die Initiierung dieser Arbeit und seine konstruktiven Hinweise, die wesentliche Anstöße in der ersten wichtigen Etappe waren.

Der Abteilung CR/ARE der Robert Bosch GmbH danke ich für die materielle und Unterstützung sowie allen anderen am Projekt beteiligten Abteilungen für die Mitwirkung.

Contents

List of frequently used symbols and abbreviations

a ..... radius of a spot
a_{c} ..... radius of a spot with equivalent area to an elliptical spot
a_i ..... radius of the i spot
$\overline{a}$ ..... mean radius of a spots cluster
A ..... area of the conductor
A_1 ..... external equipotential area
A_{a} ..... apparent area
A_{b} ..... load bearing area
A_{br} ..... brush area
A_{c} ..... conducting area
A_{rot} ..... rotor area
B ..... radius of an equipotential surface in a spherical spot
C ..... form factor of the hump
C_1 ..... first conductor of one contact
C_2 ..... second conductor of one contact
C_{glob} ..... global thickness coefficient of the model
C_H ..... humidity coefficient of the model
C_n ..... angular speed coefficient of the model
c_p ..... specific heat
C_T ..... temperature coefficient of the model
d ..... radius of a spherical spot

$\overrightarrow{E}$ ..... electric field
E ..... mean of the Young's modulus in one contact
E_1 ..... Young's modulus of the first component in one contact
E_2 ..... Young's modulus of the second component in one contact
F_r ..... friction force
F_i ..... force on each spot
$f(\gamma)$ ..... form factor of an elliptic spot
G_0 ..... independent coefficient of the tendency analysis
G_H ..... humidity coefficient of the tendency analysis
G_n ..... angular speed coefficient of the tendency analysis
G_T ..... temperature coefficient of the tendency analysis
H ..... relative humidity
H_m ..... hardness of the material
I ..... current
I_k ..... current through spot k
I_num ..... current calculated from FEM-simulations
J ..... current density
k ..... arbitrary constant
L ..... load applied to the contact
l ..... length of the ohmic part of the resistance
l_br ..... length of the ohmic part of the brush
l_rot ..... length of the ohmic part of the rotor
M ..... sum of the surface protuberances
N ..... number of spots
n ..... angular speed
n_elec ..... number of spots caused by fritting
n_mech ..... number of spots caused by the pressing load
P_H ..... humidity exponent of the model
P_n ..... angular speed exponent of the model
P_T ..... temperature exponent of the model
r ..... metric radius /radius of curvature

R_{ab} ..... measured quantity for determining R

R_{br} ..... constriction resistance on the brush

$R_{br,ana}$ ..... constriction resistance on the brush calculated with the analytical expressions

$R_{br,num}$ ..... constriction resistance on the brush calculated with the FEM-simulations

R_{c} ..... constriction resistance

$R_{c,ana}$ ..... constriction resistance calculated with analytical expressions

$R_{c,num}$ ..... constriction resistance calculated with FEM-simulations

R_{ch} ..... channel resistance

R_{cl} ..... cluster resistance

$R_{cl,ana}$ ..... cluster resistance calculated with the analytical expressions

$R_{cl,Br}$ ..... cluster resistance on the brush

$R_{cl,Br,ana}$ ..... cluster resistance on the brush calculated with the analytical expressions

$R_{cl,num}$ ..... cluster resistance calculated with the FEM-simulations

$R_{cl,rot}$ ..... cluster resistance on the rotor

$R_{cl,rot,ana}$ ..... cluster resistance on the rotor calculated with the analytical expressions

R_{num} ..... total resistance calculated from the FEM-simulations

R_{Ohm} ..... ohmic resistance

$R_{Ohm,br}$ ..... ohmic resistance on the brush

$R_{Ohm,rot}$ ..... ohmic resistance on the rotor

R_{s} ..... spreading resistance

$R_{s,br}$ ..... spreading resistance on brush

$R_{s,copper}$ ..... spreading resistance on copper

$R_{s,graphite}$ ..... spreading resistance on graphite

$R_{\mathrm{s,rot}}$ ..... spreading resistance on rotor
$R_{\mathrm{spots,ana}}$ ..... serial connection of constriction and channel resistances
r' ..... mean radius of curvature
r_1 ..... radius of curvature of the surface 1
r_2 ..... mean radius of curvature of the surface 2
S ..... contact sphere
S_{ij} ..... distance between spots i and j
t_{ox} ..... thickness of the tarnish film
T ..... ambient temperature
T_L ..... local temperature
U_{ab} ..... measured voltage for determining R
U_{fritting} ..... fritting applied voltage
v ..... speed of the sliding surface
$W(e)$ .... probability density function that two protuberances could contact

Å ..... Ångström unit = 10^{-10} m
α ..... x-axis on an elliptic spot
β ..... y-axis on an elliptic spot
γ^2 ..... α/β ratio between the axes of an elliptic spot
μ ..... height of equipotential surfaces in an elliptical spot
μ' ..... parameter of the resistance integrals between equipotential surfaces
ν_1 ..... Poisson's ratio for the surface material 1
ν_2 ..... Poisson's ratio for the surface material 2
ξ ..... area of a-spot cluster
ρ ..... resistivity
ρ_{f} ..... film resistivity
ρ_{copper} ..... copper resistivity
ρ_{ch} ..... channel resistivity
ρ_{graphite} ..... graphite resistivity
ρ_1 ..... resistivity of the conductor 1
ρ_2 ..... resistivity of the conductor 2

σ ..... tunnel resistivity

σ_s ..... yield limit of the hardened material

φ ..... electric potential

φ_{ij} ..... potential difference between contact i and infinity due to unit current through contact j

ϱ ..... material density

ς ..... empirical parameter to describe the exponential dependence of the contact area with the load

Υ ..... empirical parameter to describe the dependence of the contact area with the load and the hardness

Chapter 1

Introduction

Today, electric motors are present in many aspects of our live. They are found in household appliances, computers, power tools, and automobiles. The average car is equipped with about 120 small electric drives. Most of them are still working with the same principle as the first electric drive. The reason is, that this principle is still the most efficient solution regarding specifications and costs for small and medium size electric motor applications.
Electric motors and generators in general convert electric energy in mechanical energy and vice versa. Electric energy is used to build up magnetic fields which are reversed periodically. This is done - for this dominant number of motor types - by a sliding contact between carbon and copper. This sliding contact can lead - when improperly designed - to increased radio frequency electromagnetic noise produced by arcing at the motor brushes. The same effect reduces the lifetime of the motor significantly by eroding the brushes. To avoid this effect on the one hand a proper electromagnetic design is needed to reduce the remaining energy in the coils specially during commutation of the electromagnetic fields. On the other hand, a careful design of the brush contact is necessary to avoid abrupt changes and drifting of the contact's properties.
In practice, the DC motors are subject to different environmental situations, influencing their performance. Changes in atmospheric temperature and humidity have a significant influence on the electrical and mechanical properties of a sliding contact and thus on the motor's performance and lifetime.
Therefore these influences have to be taken into account when designing a new motor in order to fit the requirements given by the respective application.
For up-to-date engineering approaches by system simulation a model de-

scribing the behaviour of a sliding contact in all its relevant parameters is needed. This would lead to the possibility to optimise the motor within its application already before time-consuming and expensive practical tests. This work deals with the brush slip ring contact modelling, regarding the environmental variables like humidity, temperature and angular speed as parameters.

This report is divided in four sections as follows:

Chapter 2, "Theoretical Basis" approaches the sliding contact problem with the constriction theory as basis. The explanation starts with the contact definition, clarifying its mechanical characteristics as real area of contact, contacting spots and oxide layer. After this introduction, the electrical consequences of these contact properties are explained as the conduction through small spots and the existence of an electric breakdown effect through the oxide layer. The breakdown effect is explained as a combination of the classical contact theories (fritting) and the semiconductor theory. Then, the constriction theory is explained summarising the different equations. They are based on the constriction theory applied to a circular spot, an elliptical spot and a cluster of spots. Then, all these equations are checked for a sliding contact, comparing the static contact with the sliding one. Finally, possible variable influences and dependencies are discussed, referring to bibliographic sources.

Chapter 3, "Numerical Verification of the Theory" deals with the simulation of the different analytical equations given in the previous chapter. These simulations are performed by using a FEM-simulator, reaching numerical solutions for different contact geometries. These numerical results are based on the Maxwell equations and boundary conditions. The different constriction equations that will be used in the model are checked. These checked resistance equations correspond to a circular spot, an elliptical spot and a cluster of spots. In all cases, a comparison between the analytical and numerical results is done, calculating the different errors between results. Thus, the applicability of the analytical equations is tested comprising the different constriction equations. Finally, the applicability of the constriction theory is confirmed through the numerical simulations.

Chapter 4, "Test Bench" presents the measurements, going from the experimental set-up to the measured results. The experimental set-up is introduced, explaining the electric circuit and the devices used. Taking into account the set-up characteristics, the involved parameters are explained, clarifying their regulation and measurement. Then, the first measurement steps are described as reproducibility, hysteresis cycle, error calculation, programming characteristics, and finalising with the test algorithm. All the systematic measurements are done by applying this test algorithm. Before

presenting the summarised results, a selected measurement is given in detail. Afterwards, the measurements are presented in two describing forms: on the one hand as UI-curves, and on the other hand as a tendency analysis. With these two presentations, the measurements are analysed. Finally, the observed influences and dependencies of the different parameters are summarised.
Chapter 5, "Model" discusses the implemented model and its results. First, the model is introduced showing its equivalent circuit. The clarification follows with each electric device, explaining each represented effect as constriction, ohmic, channel and cluster resistances. In addition, each device takes into account different influences as temperature increase at rotor surface, specific resistivities of copper and graphite, spot radius, oxide thickness and contact load. In order to know the model in detail, a list of all the relevant equations for the devices and influences is given. After all the equations used are summarised, the model parameters are presented and classified. To adjust the model to the measurements, the free parameters of the model are optimised by a hierarchical optimisation process. The model results are presented following the optimisation steps, comparing the UI-curves of the measured and modelled values. Finally, the optimised range is presented and discussed.
Chapter 6, "Conclusions" summarises the accomplished facts along the investigation. Finally possible extensions of the investigation are proposed.

Chapter 2

Theoretical Basis

2.1 Introduction

Although the electric motor was first patented by Davenport in 1837, a functional-physical brush-sliding ring contact model has not been developed yet. The contact voltage drop between brush and rotor is a key parameter in the design of an electric motor. However, the quantity of parameters involved in its analysis, together with its non-linear behaviour, lead to an accentuated complexity of its study.
A previous step necessary to explain a sliding contact main characteristics is to describe a stationary contact. Then, the general concepts of electric contacts have to be introduced. Firstly, a definition of the electric contact will be provided. Secondly, the surface in contact will be described. The fact that the solid surfaces are not flat surfaces produces an effect of conduction through small spots. These small spots do not have a constant resistance. As a consequence of this, resistance will have to be specifically calculated for every spot's case. Another factor to be taken into account when analysing a metallic contact is the oxide barrier. Since an electric motor is usually exposed to atmospheric conditions, its metal surfaces are oxidised. Moreover, an insulating layer initially stops the conduction, so a breakdown effect is present on the contact behaviour. This is why the third point is based on the explanation of the electric breakdown. The breakdown theory of electric contacts is an old attempt to explain this effect. In order to have a newest and alternative point of view, two different theories are outlined. The first one is the classical electric contact theory. The second one is a modern breakdown theory developed in the microelectronic field. After the explanation of the related physical effects, resistances for different geometries

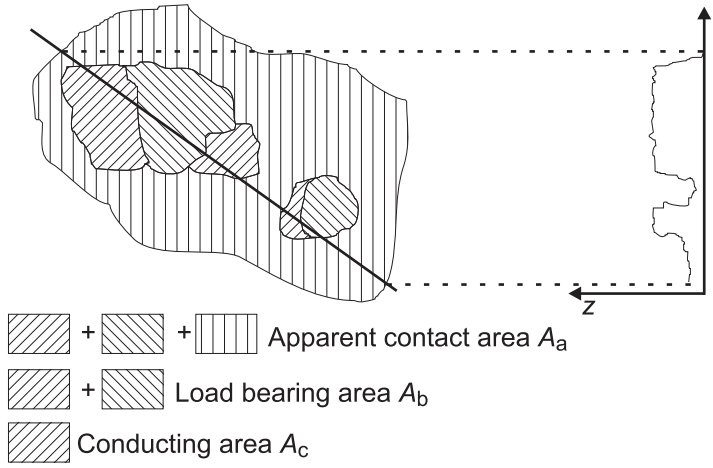

Fig. 2.1: Typical contact areas.

will be calculated. Still dealing with the electrical implications of the spots existence, the next point is about the influence between the spots. After this stationary contact explanation, the case of sliding contacts will be discussed. Finally, a relation between macroscopic and microscopic parameters which influence the electric contact will be established.

2.2 Electric Contact

The electric contact is the junction between two conductors, which are able to carry electric current. When an insulating layer separates the contact conductors, it is called *open contact*. In this case, the contact is not able to carry the electric current. In order to have a stable electric contact a force is needed. This force presses and maintains the two parts together. This force is named *load*.

All solid surfaces are rough on the microscale. Surface microroughness consists of peaks and valleys whose shape, height variations, average separation and other geometrical characteristics depend on fine details of the surface generation process. Contact between two bodies thus occurs at discrete spots produced by the mechanical contact of protuberances on the two surfaces. For all solid materials, the area of true contact is thus a small fraction of the nominal contact area. The *apparent area* A_a is defined as the whole covered area. The *load bearing area* A_b is the area where the two materials involved in the contact are in touch. The *contact area* A_c is the part of the A_b where

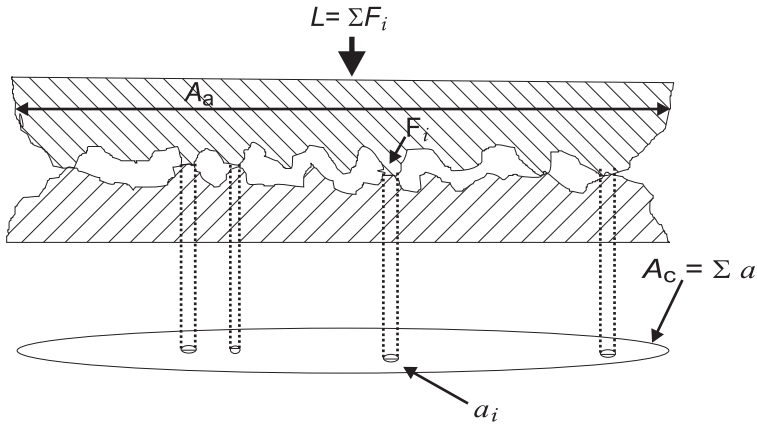

Fig. 2.2: Schematic of rough surfaces in a normal contact.

the electric current is able to flow.
The mode of deformation of contacting protuberances is either elastic, plastic or mixed elastic-plastic depending on local mechanical contact stresses and on material properties such as elastic modulus (Young's modulus) and hardness.
In an electrical interface where the mating components are metals, the contacting surfaces are often covered with oxide or other electrically insulating layers. Thus, the A_b is covered by insulating films called *tarnish films*. In general, the interface becomes electrically conductive only when metal-to-metal contact spots are produced. This is achieved where:

- electrically insulating films are ruptured or displaced at contacting surface protuberances by mechanical stress or because
- an electric breakdown occurs due to the applied electric field.

It can be said that every contact is composed of a finite number of contact points which are carrying the current (Fig. 2.2). These points are called *a-spots*. In fact, only a much smaller part of the A_b is electrically conducting, and it is called *conducting area* A_c. This means that on every contact there are three different areas. Taking their definitions into account, they can be ordered as follows: $A_\mathrm{c} < A_\mathrm{b} < A_\mathrm{a}$.
A two spot's contact is shown in Fig. 2.3. The current comes from the conductor C_1, goes through the two spots and outlets through the conductor C_2. The conductors are semi-infinite, so C_1 continues infinitely above the figure and C_2 continues infinitely below the figure. Thus, all current lines go

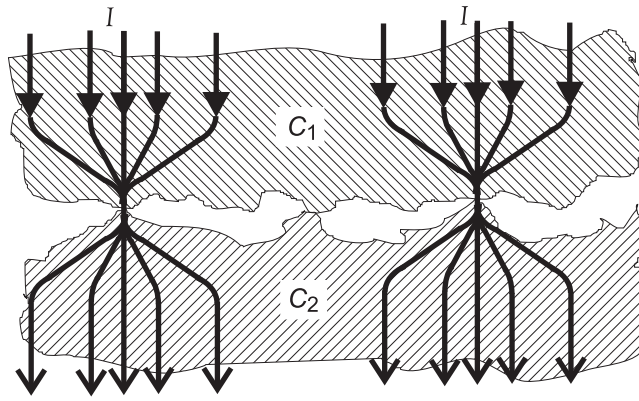

Fig. 2.3: Schematic diagram of a bulk electrical interface.

inside and outside parallel to each other. However, as the current lines come closer to the spots, they become increasingly bent. The flow lines bundle together to pass through the separate contact spots. As the current lines are bent together through narrow areas, an increase of resistance is caused. This increase of resistance is the *constriction resistance* R_c (see section 2.5).

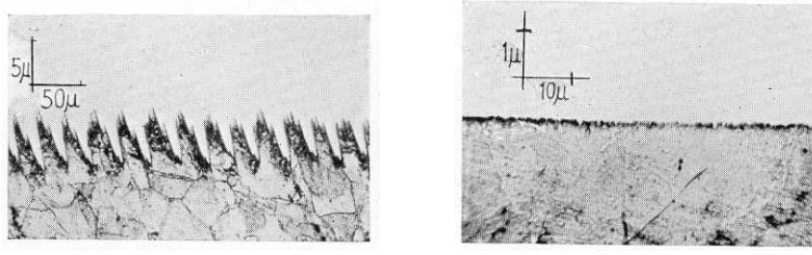

(a) Taper section of finely turned Cu surface. Irregularities are about 5 µm high.

(b) Taper section of steel surface polished in 600 grade carborundum paper. Irregularities are about 0.1 µm high.

Fig. 2.4: Taper sections of different materials [13].

2.3 Contact Surface

When two bodies are pressed together, the roughness of their surfaces causes the contact to be restricted to a set of microscopic real contact areas. The

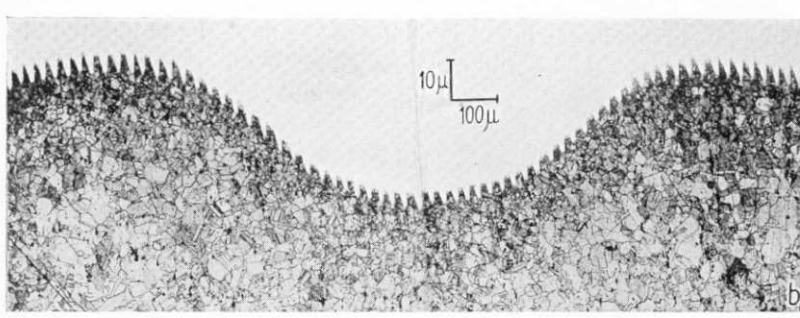

Fig. 2.5: Taper section of deep indentation in annealed grooved Cu surface showing persistence of grooves after extensive bulk deformation [13].

early studies of Greenwood and Williamson and also of Holm found out that Hertz's theory could also be applied to describe the mechanical contact between surfaces [30, 34, 13]. Hertz's theory relates the real contact area to Young's modulus (E), Poisson's ratio (ν) and curvature radius (r). According to this theory, the size and spatial distribution of actual contact areas depend on the detailed geometry of the contacting rough surfaces [5, 34, 30, 71, 23, 13, 43].
The contact between two surfaces is composed by microspots. Even the hills & valleys found on carefully polished surfaces are large compared with the size of a molecule. For example, on a polished aluminium surface there are little hillocks of about 1 µm [11]. Bowden and Tabor polished different material surfaces [13]. In Fig. 2.4 there are two examples of this. The first one is Cu that has gone through an oblique sectioning, a standard method developed in order to improve the study of surface irregularities. The irregularities are 5 µm high. The second one is polished steel. The difference between the humps found on this polished surface and those on the non-polished Cu is about of one order of magnitude.
Then, when two bodies are in contact, the contact area agrees with the Hertz law [34, 71, 76, 11, 13, 43]. Some surface irregularities behave in a plastic manner with a light load. For example, with tool steel the load necessary to initiate plastic deformation is of the order of $1{\cdot}10^{-5}$ N [11]. When metal surfaces are in contact, even under quite small loads, the material around the finer surface protuberances is subjected to stresses that readily exceed the elastic limit. There is an example of this in Fig. 2.5, where a high load has been applied to the central zone. We can see that the protuberances keep the same shape along the surface. These plastic zones appear where the two

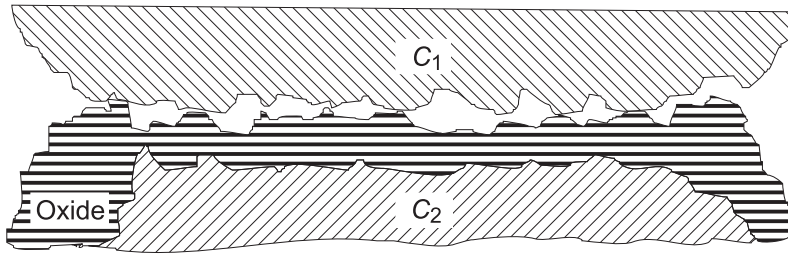

Fig. 2.6: Sketch of two conductors making contact with the presence of one oxide layer.

conductors are in contact, then the conduction is achieved through these zones. The size of these zones determines the size of the a-spots [11, 43, 76].

2.4 Breakdown of an Insulating Layer

In an air environment the conductors suffer from oxidation. This oxidation develops a surface oxide layer. A Graphite-Cu contact represents the standard brush-slip ring contact. Fig. 2.6 shows a sketch of the situation in which C_1 is Graphite and C_2 is Cu. In this case Cu undergoes oxidation, whereas Graphite does not develop this insulating surface layer. In this case the conduction is then obstructed by this layer. When an electric field is applied, the charges accumulate on the conductor surface. When this accumulation is huge enough a breakdown happens and current can flow.
Breakdown in solids can be caused by different mechanisms. The discharge of the electrostatic energy stored in the material through the conducting channel determines mainly where the insulating layer will be removed. The critical parameter is the field strength $\overrightarrow{E}$ in the insulating layer. If it is too large, breakdown occurs. After reaching the critical electric field, a sudden flow of current may destroy the dielectric to a mass of non-regular structure, within very short times (10^{-8} s) [25]. The critical electric field depends on many parameters. The most important ones (besides the basic material itself) are the production process, thickness, temperature, internal structure (defects), age, characteristics of the environment where it is used (especially humidity) and the time during which it experienced field stress. It is usually found that destruction of the insulating layer occurs at applied fields larger than 10^7 V/m [34, 71]. Lower fields do not lead to destruction, but to sporadic, non-permanent discharges.
Thermal breakdown is caused at low frequencies by the Joule heat of the

leakage current and at very high frequencies by dielectric losses. At low frequencies, the Joule heat leads to thermal instability and current runaway due to rapid, often exponential, rise of the conductivity with temperature. The breakdown fields decrease rapidly with increasing temperature and time of voltage application [24].

Reference	$\lvert\overrightarrow{E}\rvert$ (V/m)	Material
[25]	$2 \cdot 10^7$	Oil
[25]	$2\text{-}4 \cdot 10^7$	Glass, ceramics
[25]	$2\text{-}7 \cdot 10^7$	Mica
[25]	$18 \cdot 10^7$	Oiled paper
[25]	$5\text{-}90 \cdot 10^6$	Polymers
[34]	$0.6\text{-}1.6 \cdot 10^8$	Cu_2O
[16]	$2.5 \cdot 10^8$	PMMA[a]
[58]	$4.75 \cdot 10^8$	SiCO
[58]	$4.5 \cdot 10^8$	SiN
[58]	$4 \cdot 10^8$	SiCN
[16]	$3\text{-}12 \cdot 10^8$	SiO_2

[a] Polymethylmethacrylate

Table 2.1: Literature data of electric field values of breakdown.

Electric breakdown can be initiated by a variety of processes such as impact ionisation, field emission, double injection, and, possibly by insulator-to-metal transition. Breakdown in insulators is usually ascribed to the interaction of impact ionisation, charge carrier injection into the insulator, and the effect of space charges. In thin regular films, breakdowns are found to occur randomly in space and in time, involving only a very small part of the insulator. The typical range of electric field at which breakdown occurs in insulators varies from 10^7 to more than 10^9 V/m [8, 58].

2.4.1 Electric Contact Theory: Fritting

The electric breakdown theory in electric contacts was elaborated by Holm and used as standard in all subsequent publications by other authors.
An ideal situation can be seen in Fig. 2.7. The scenario can be described as follows: two conductors are separated by a high resistivity tarnish film of about 100 Å thickness [71, 36]. The starting voltage is low but increases constantly with time. In this initial situation the resistance is high because of the high specific resistivity of the film. As the voltage steps up the electric field in the insulator increases. When there is a voltage of about 1 V, the

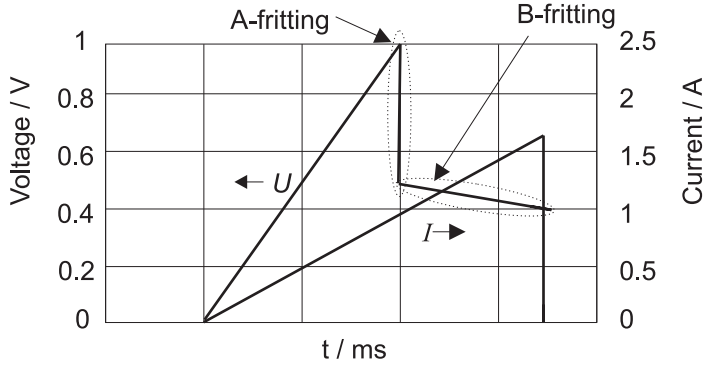

Fig. 2.7: Transient current and voltage on a stationary contact (Ag-Graphite) [70].

fritting happens. At that moment there is an electric field of 10^8 V/m in the film. With an electric field of this range, a sudden increase of the current and a decrease of the voltage is observed [9, 34, 71]. This effect is called fritting and is a kind of electric breakdown. This film breakdown, leading to immediate melting of the insulating layers [34, 9, 71, 36], is usually referred to as *A-fritting*. A-fritting occurs when the voltage across the metallic components through the insulating film is larger than the so-called *melting voltage*. This melting voltage is usually of the order of 1 V [40, 34, 71]. After this oxide breakdown has taken place, a huge current density flows through a small area. Then, by means of the Joule effect, a high heat is generated. Thus, the oxide of the tarnish film is released, and a metal channel appears through the film. In Fig. 2.7 two voltage decreases are shown. The second one in time is a slow one with some ripples. For small change of the incoming current there is an adaptation of the channel geometry. This adaptation effect is named *B-fritting*.

Two measured examples of A-fritting are shown in Fig. 2.8. The measurements were carried out between Cu and Au, with Cu carrying the tarnish film (tarnish film thickness of 100 Å) [34, 71, 36]. The crossed rod contact had a diameter of 3 mm. The resistance was constant at low voltages. As the current increases, the resistance decreases by the tunnel effect (line A and B). The current intensifies and when the voltage is about 1.8 V the A-fritting is activated. At this point there is a decrease of the voltage as well as a decrease of the resistance (lines D and C). These drops cannot be caused by a temperature effect, since the undamaged film is not exposed to high temperatures.

The B-fritting is depicted in Fig. 2.9. The scenario is an Au contact with

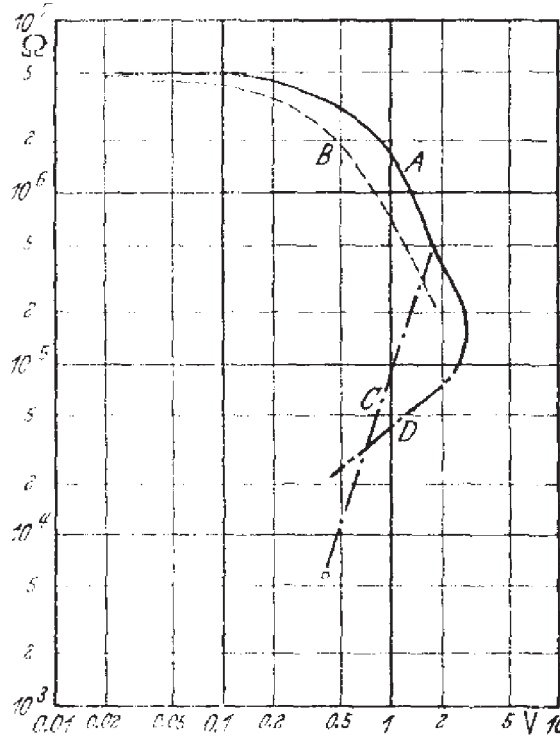

Fig. 2.8: *RU*-characteristics of a crossed rod metal contact (Cu against Au) with a film, finally subjected to A-fritting [34, 71, 36].

a steadily increasing current. The A-fritting already happened before the start point. In this figure the B-fritting seems to appear at 0.2 V. The first B-fritting phase is the rough channel adaptation: there is a gross voltage increase and a resistance decrease. After this rough channel adaptation, a reversible phase appears. At this point, the channel has a stable structure and a reversible adaptation. Then, resistance and voltage decrease at the same time and the *RU*-curve is reversible [36]. This physical phenomenon is explained by the increase in the diameter of the channel between conductors [36, 34, 71, 70, 9, 66]. The measurements indicate that, once a metallic channel is formed through the film between two conductors, the increase of current causes an increase in the channel diameter. If the current decreases, the effective cross-sectional area decreases too.

In summary, there are two effects: on the one hand, the breakdown itself

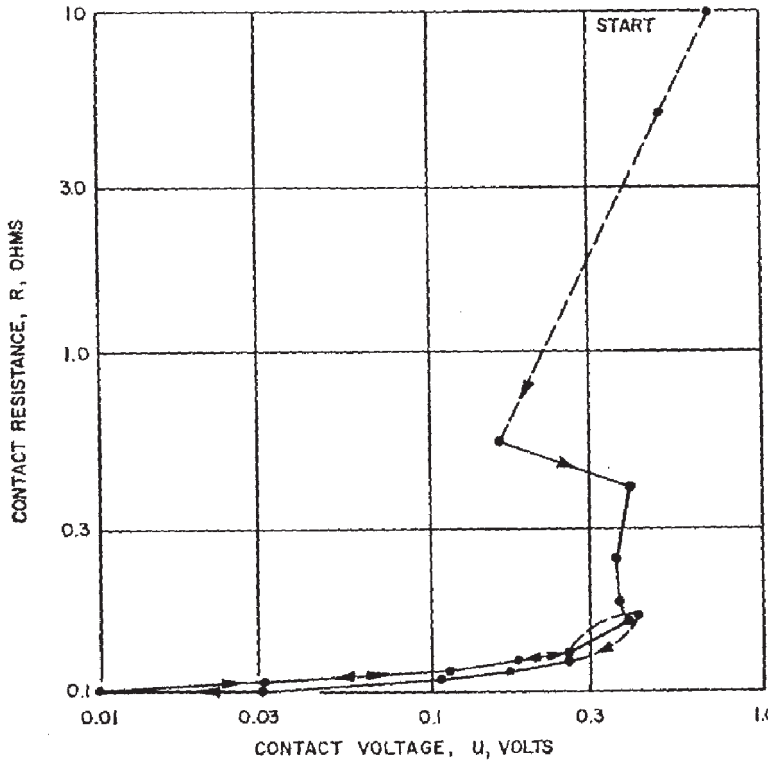

Fig. 2.9: *RU*-characteristics of a crossed rod metal contact (Cu against Au) with a film, finally subjected to B-fritting [36].

and, on the other hand, the adaptation of the channel geometry:

A-fritting: It is the formation of a new spot. The process is originated by the injection of electrons into a path in the undamaged film and is accomplished with the formation of one channel.

B-fritting: It is the adaptation of an existing spot to increasing currents through widening of the conducting areas. This type of fritting is the result of the Joule heat.

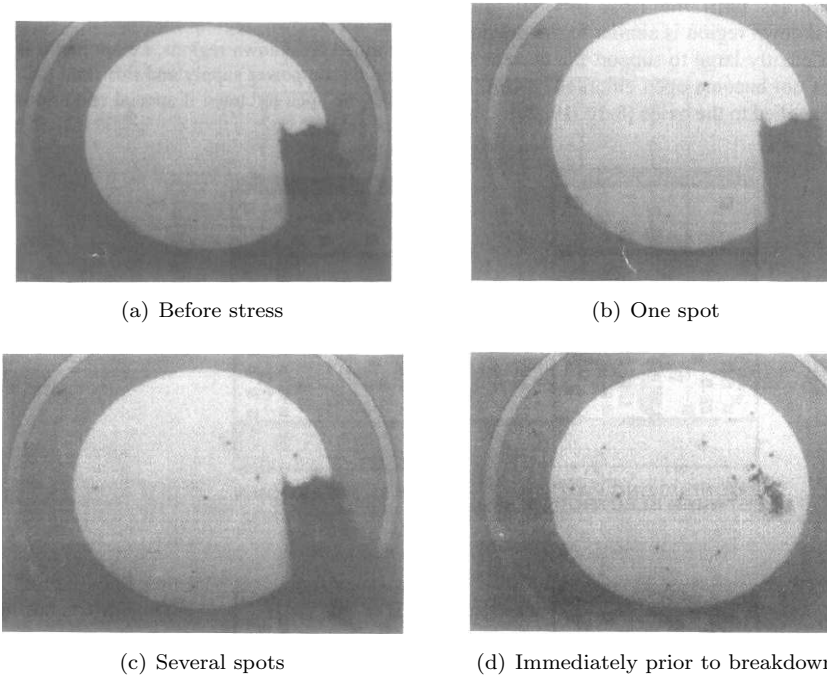

(a) Before stress

(b) One spot

(c) Several spots

(d) Immediately prior to breakdown

Fig. 2.10: Formation of spots in a capacitor [22]. Spots form on the surface of the aluminium, covered by polysilicon gate material, every time a partial discharge occurs. This oxide was 80 nm thick and the applied voltage was 87 V. The time between the observation of the first breakdown event and final dielectric breakdown was about 100 s.

2.4.2 Semiconductor Theory: Oxide Breakdown

There is another field in which the oxide breakdown has been a recently focused topic, namely, the CMOS technology, which has studied the breakdown of the oxide gate. By innovations in the CMOS process (lithography, etching, deposition), the size of structures in this technology has been reduced dramatically. The size of the gate oxide is comparable to the range of the tarnish film thickness. In a microelectronic technology, if the oxide is thick and the gate materials are thin, it is possible to see the individual spots. Fig. 2.10 contains an example of spot formation during each partial discharge. There is a capacitor where the oxide is 80 nm thick. A series of individual discharges (87 V) was applied for about 100 s. After each partial discharge, a spot appears showing the melting process associated with the

breakdown region [22]. Each partial discharge was accompanied by a fast transient discharge-charge signal. During the partial discharge events the gate voltage temporarily dropped to a lower voltage, typically about 10% of the stress voltage.

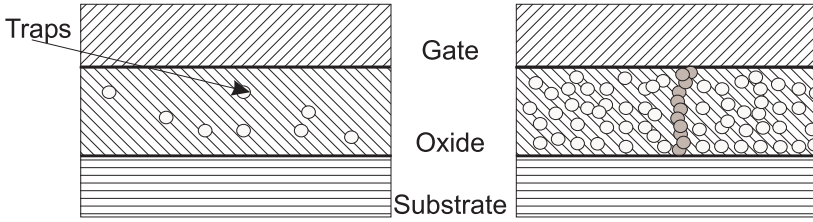

(a) Formation of traps in the oxide.

(b) Creation of conduction path through traps in the oxide.

Fig. 2.11: Soft breakdown formation.

The theory of the breakdown is based on trap[1] generation. The process is as follows: at high electric fields, the electrons arriving at the gate have been accelerated in a high electric field ($6 \sim 8 \cdot 10^8$ V/m) [59]. When these hot electrons reach the gate electrode, some of them transfer their entire energy to a deep-valence band electron. As soon as an electron receives this energy, it is then promoted to the lowest available electron energy state, which is the conduction band edge of the anode [69, 35]. Once the electron reaches the conduction band, it creates a hot hole, which tunnels into the oxide [69, 73]. The holes that enter into the oxide are trapped in it [69, 47, 73]. Once the trap has been created, there is an increase of current density. Therefore, there are more high-energy electrons entering into the gate, which can create more hot holes. Thus, there is positive feedback until breakdown occurs [35, 73].
The density of traps is treated with a percolation model [74, 19, 10, 22]. The basic idea is that traps are spawned in random locations in the oxide and a conduction path is formed when adjacent traps span the thickness of the gate oxide. This phenomenon is modelled using spheres in a Monte Carlo simulation. Every time a sphere touches another, the spheres conduct. When there is a continuous chain of linked spheres connecting the top and bottom surfaces of the gate oxide, breakdown occurs. Degraeve used this model to verify that the distribution of breakdown behaved according to

[1] Defects within the oxide are usually called traps because the degraded oxide can trap charges. Traps are usually neutral, but quickly become positively charged near the anode, and negatively charged near the cathode [22, 61, 69].

Weibull curve [19], and also showed the dependence of Weibull slope on oxide thickness.
Oxide breakdown starts when traps are formed in the oxide. At first, the traps are non-overlapping and thus do not conduct (Fig. 2.11(a)), but as more and more traps are created in the oxide, they start to overlap. The traps concentration increases until a percolation limit is reached [50]. At that point, there is a high probability that the traps overlapping creates a conducting path through the oxide [19]. Once these traps form a conduction path from the gate to the substrate, breakdown occurs [19], as shown in Fig. 2.11(b). This type of breakdown is called *Soft Breakdown* (SBD).

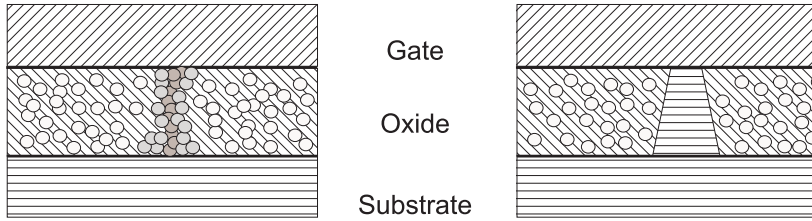

(a) Increased traps in oxide after conduction. (b) Cross section of the oxide after HBD.

Fig. 2.12: Formation of the hard breakdown.

Once there is conduction, new traps are created by thermal damage, which consequently allows an increasing conductance as shown in Fig. 2.12(a) [46]. There is a cycle of conduction, producing increased heat and increased conduction, as well as producing thermal runaway [46]. Finally, there is a lateral propagation of the breakdown spot [20]. The silicon within the breakdown spot starts to melt, and oxygen is released. Then, a Cu filament is formed in the breakdown spot [46]. This type of breakdown is called *Hard Breakdown* (HBD) and can pictorially be seen in Fig. 2.12(b).
Baitun applied this theory through an experiment obtaining the results shown on Fig. 2.13. In this experiment, Baitun applied a constant current on a capacitor for 30 min. After that, a high voltage was applied. The number of occurring breakdowns cases were counted in order to obtain the probability of breakdown. The line represents the calculated value of the breakdown probability. The discrete values are measured. We can observe that the theory predicts the experimental data.

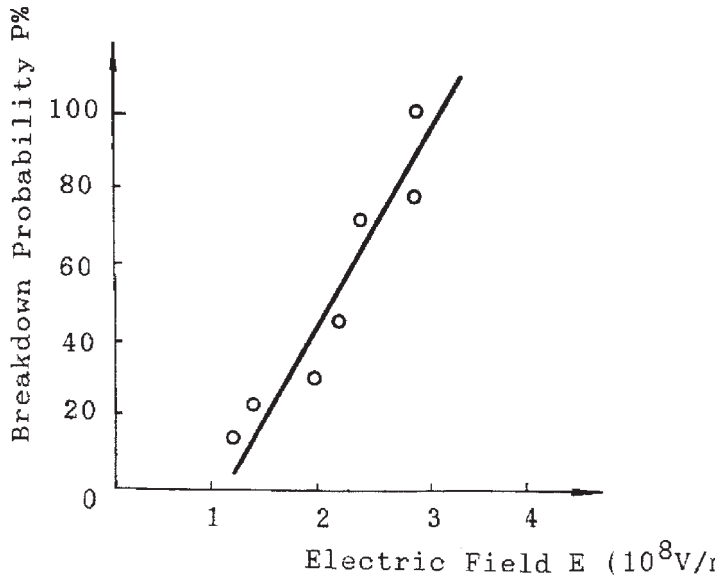

Fig. 2.13: Probability of a breakdown effect vs. the electric field through the oxide [4].

2.4.3 Comparison of the Two Models

The two models describe an electric breakdown. In both models, the electric field through the oxide reaches a huge value with a low voltage, as a consequence of the tiny thickness of the oxide. This huge electric field is the origin of the breakdown. In this situation, the electrons have a high probability to go through the conductor-insulator potential barrier. In both cases, the consideration of the current through the oxide is the first step to achieve the charge trap. This current leaves trap holes in the oxide.
Moreover, in both theories, the high electric field causes an increase of temperature although it cannot be considered as the origin of the breakdown. In addition, in both descriptions the charges in the insulator cause the electric field to increase. Having a positive loop, a growing electric field leads to an increasing charge trapping.
Furthermore, there is another similarity concerning the melting of the channel. The two theories describe a release of the oxide after the breakdown. As soon as the oxide disappears from the conducting channel, a metal channel is formed. In Fig. 2.10, the different originated spots can be easily noticed.

Thus, there has to be a difference between the material where the channel has been created and the other insulator zones.
Finally, after the conducting path is formed, the situation changes, and this high current generates heat. Together with the current, the heat causes an excitation of the oxide material. The final conducting path after a B-fritting is in fact a mixture of all the materials present in the environment.
The two models distinguish between two types of breakdown effect. Also, both models lead to the same result: a first channel is developed by the high electric field: after this, a positive cycle generates a metallic channel through the oxide. Thus, an analogy could be established between both theories:

- A-Fritting = Soft Breakdown (SBD)
- B-fritting = Hard Breakdown (HBD)

The second step (B-fritting) results from of the Joule heat. This current generates heat in order to cause the oxide runaway and a stable conducting channel through the film. The geometry of the channel varies depending on the current value.

2.5 Constriction Resistance of a Single Spot

In order to predict the contact resistance, the constriction resistance of one spot is going to be calculated. It will be shown that the total resistance is dominated by this constriction value. The first attempt is made with a spherical symmetry. The only target of this scenario is to show the best procedure to calculate the resistance of one spot. It is an ideal situation and it is as close to reality as possible.

2.5.1 Spherical Spot

In the following case, two symmetrical and semi-infinite conductors of the same material and a spherical contact (S) (Fig. 2.14) are considered.
The contact is a sphere S with an infinite conductivity and radius d. The lines of current flow are distributed radially and symmetrically around S. Thus, the equipotential lines are concentric spheres around sphere S.
The constriction resistance dR in one conductor between the hemispheres with the radii r and $r + dr$ is

$$dR = \frac{\rho\, dr}{2\pi r^2} \quad . \tag{2.1}$$

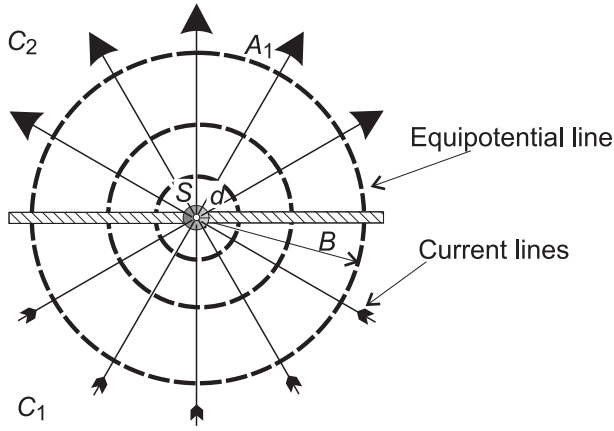

Fig. 2.14: Current constriction with spherical symmetry. Where C_1 and C_2 are the conductors 1 and 2 respectively, S is the contacting sphere of radius d, and B is the radius of the external sphere with area A_1.

To calculate the constriction resistance of one spot in one conductor, the integration goes from d to B (where $B >> d$), so

$$R = \frac{\rho}{2\,\pi} \int_{\mathrm{d}}^{\mathrm{B}} \frac{dr}{r^2} = \frac{\rho}{2\,\pi} \left(\frac{1}{\mathrm{d}} - \frac{1}{\mathrm{B}} \right) \approx \frac{\rho}{2\,\pi\,\mathrm{d}} \quad . \tag{2.2}$$

The final result shows that the resistance is inversely proportional to the spot size. Thus, the more the spot size decreases, the more the resistance increases.

2.5.2 Circular Spot

The case of two cylindrical conductors of radius r and made of the same material is closer to reality. The two conductors are connected with each other through their circular base areas. The contact is assumed as a circular a-spot between two cylindrical conductors. All the contact components are concentric. The a-spot has a radius a, and the two conductors have a radius $r >> a$ (Fig. 2.15).
The mathematical problem of constricted current flow is handled in several textbooks [72, 42]. For a circular constriction between two semi-infinite solids with $r >> a$, it is found that the equipotential surfaces in the conductors

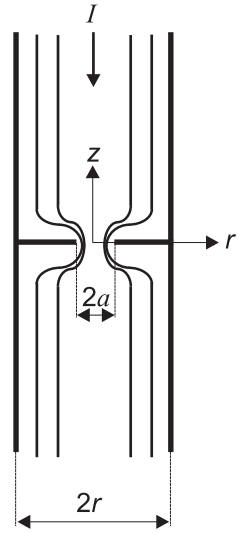

Fig. 2.15: Electrically conducting cylinder of radius r carrying a circular constriction of radius a.

consist of ellipsoids defined by the equation

$$\frac{r^2}{a^2+\mu^2}+\frac{z^2}{\mu^2}=1, \tag{2.3}$$

where μ is the height of the equipotential ellipse and r, z are cylindrical coordinates. The resistance between the equipotential surface μ and the spot is given as

$$R_\mu \;=\; \frac{\rho}{2\,\pi}\int_0^{\mu}\frac{d\mu'}{(a^2+\mu'^2)} \;=\; \frac{\rho}{2\,\pi\,a}\arctan\left(\frac{\mu}{a}\right) \quad , \tag{2.4}$$

where ρ is the specific resistivity of the conductor.
Fig. 2.16 shows the different equipotential lines for different μ. These μ values are expressed as functions of the spot radius. We can see the described equipotential ellipsoids around the spot. Furthermore, the different current fractions are shown as function of the integration angle with the vertical central axis. The bigger fraction of the current concentrates in big angles.
In case that μ is large compared with a, the constriction resistance for each

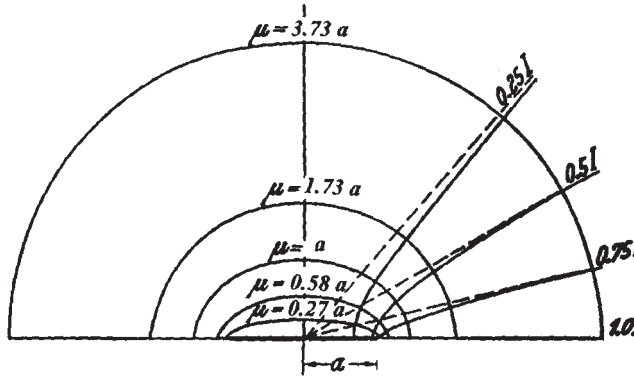

Fig. 2.16: Equipotential surfaces and current flow lines near an electric constriction. The parameter μ is the vertical axis of the vertical ellipsoidal surface, and a is the radius of the spot. The curves corresponding to current flow identify the boundaries enclosing the current fraction indicated.

conductor (called *spreading resistance* R_s) becomes

$$R_\mathrm{s} = \frac{\rho}{4\,a} \quad . \tag{2.5}$$

The difference between this result and the one in Eq. 2.2 is a consequence of the different conducting geometries.
In the case of different contact materials, the electric constriction resistance then becomes

$$R_\mathrm{c} = \frac{(\rho_1 + \rho_2)}{4\,a} \quad , \tag{2.6}$$

where ρ_1 and ρ_2 being the specific resistivity of the respective materials. In our case we have Graphite and Cu as contact materials. As $\rho_\mathrm{graphite} >> \rho_\mathrm{copper}$, the total constriction resistance of the contact Graphite-Cu is determined by the Graphite [71].

2.5.3 Ellipticity Spot

In conditions where the surface microtopography of mating bodies is not isotropic, the a-spots could not be treated as circular “on the average”. The

a-spot is approximately an elliptic bridge, so the influence of the shape has to be investigated.
From the point of view of the mathematical problem of a constricted current flow but this time through an elliptical spot, Smythe [72] found that the equipotential surfaces in the conductors are semi-ellipsoids with the equation

$$\frac{x^2}{\alpha^2+\mu^2} + \frac{y^2}{\beta^2+\mu^2} + \frac{z^2}{\mu^2} = 1 \quad , \tag{2.7}$$

where μ is the height of the semi-ellipsoids and the elliptical architecture has as semi-axes α and β. For the sake of simplicity, the axes coincide with directions of x and y.

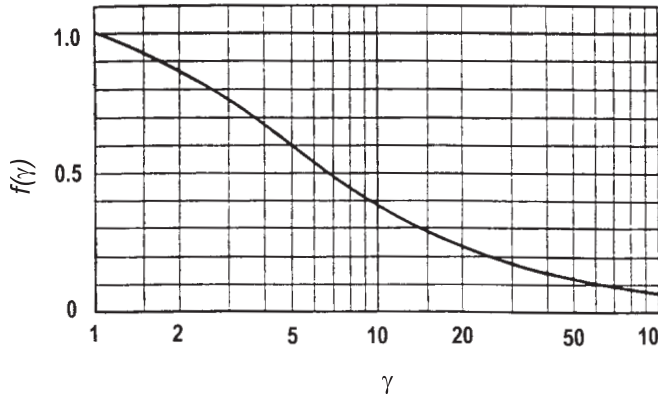

Fig. 2.17: The function $f(\gamma)$ in a general case [34].

The spreading resistance between the equipotential surface with vertical axis of length μ and the spot is given as [34]

$$R_\mathrm{s} = R_\mu = \frac{\rho}{2\pi}\int_0^\mu \frac{d\mu'}{\sqrt{(\alpha^2+\mu'^2)(\beta^2+\mu'^2)}} \quad . \tag{2.8}$$

With $\mu \longrightarrow \infty$, this equation may be expressed similarly to the spreading resistance of the circular case in Eq. 2.5 as

$$R(\alpha,\beta) = \frac{\rho}{2\pi}\int_0^\infty \frac{d\mu'}{\sqrt{(\alpha^2+\mu'^2)(\beta^2+\mu'^2)}} = \frac{\rho}{4\,a_\mathrm{c}} f(\gamma) \quad , \tag{2.9}$$

where γ is the square root of the aspect ratio of the spot axes[2]. The function $f(\gamma)$ is a form factor and the quantity a_c is the radius of a circular spot with an area identical to that of the elliptical a-spot.
The form factor $f(\gamma)$ for the case of $\mu = \infty$ is shown in Fig. 2.17. The ellipticity factor γ is 1 when a circular spot is considered. In the case of a circular spot, the factor f is the unit, so the resistance is a circular one. The more elliptical the spot is, the more the factor γ grows. However, as the spot's ellipticity increases, the form factor decreases; this decrease results in a decrease of the resistance.
In the case of a large elliptic spot ($\gamma > 2$), Eq. 2.9 could be written as [34]

$$f(\gamma) = \frac{4}{\pi\gamma} \ln(2\gamma) \quad . \tag{2.10}$$

The shape function of this formula is shown in Fig. 2.18. It can be compared with Fig. 2.17, where, for a circular spot, the figures do not coincide. However, for a great γ there is the same form factor.

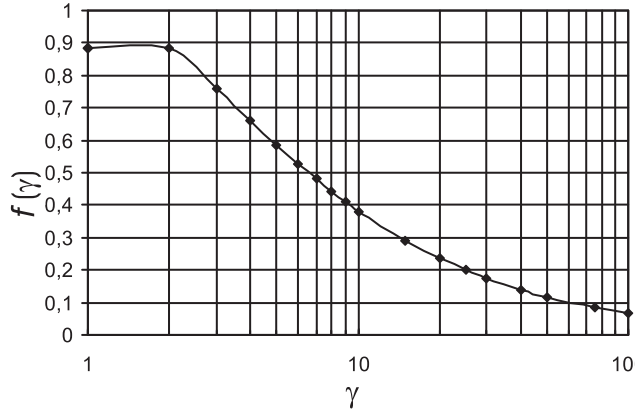

Fig. 2.18: The shape function $f(\gamma)$ from Eq. 2.10.[34]

2.6 Cluster of Spots

A_c is a function of the unevenness of the surfaces. For a constant number of a-spots, a smaller A_c implies a higher spot density. This situation is possible

[2] $\gamma^2 = \alpha/\beta$ or $\gamma = a_c/\beta = \alpha/a_c$

on a contact [34, 71, 23]. In this case the interaction between spots has to be taken into account. The total resistance consists of two parts [34, 71, 30, 15]:

- the individual resistances of each spot,
- the interaction of each spot with the other ones.

On the first steps of his theory, Holm [33] derived an equation taking into account the cluster contribution. The total resistance was the sum of the self resistance of each spot and the interaction resistance. This equation is rarely used perhaps because it cannot be found in Holm's more accessible publications. Another attempt to find out the resistance of one spot's cluster was made by Greenwood [30]. On next steps, we are going to see different approximations in order to reach these equations.
Contact between nominally flat surfaces is made on small zones. Within these zones, there are clusters of microcontacts (Fig. 2.1). The position of the clusters is determined by the large-scale waviness of the surface, and the microcontacts, by the small-scale surface roughness. As a result of this, the constriction resistance will be partly determined by the number and size of the microcontacts and partly by their grouping into clusters. So the resistance can be described as a summation of the self resistance and the

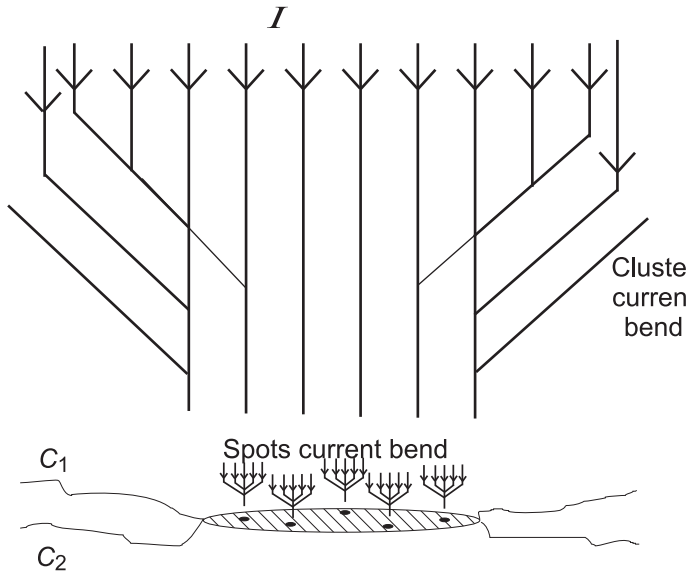

Fig. 2.19: Cluster and spot current bend in an A_c.

interaction resistance [33, 30, 6, 32, 17, 15, 18, 41].

2.6.1 Holm's Calculation

The scenario is a cluster of spots far away from all the other clusters. The two conductors are made of different materials, one of them with higher specific resistivity than the other (upper material). So the voltage drop is mainly located in the upper one. Far away from the contact, the current is distributed along the conductor area. As the current is coming closer to the contact, there is a change in the distribution (Fig. 2.19). The current bends towards the cluster, increasing the current density on the cluster vertical. This first current bend is named *cluster current bend*. This first accumulation of the current is produced by the effect of all the spots together; in other words, this cluster current bend is an effect caused by the presence of the cluster. When the current is in the closest area to the contact, it is distributed in each spot. This new distribution will be known as the *spots current bend*. This spot current bend is equivalent to the constriction resistance of a single spot calculated above. From the point of view of the potential, the general effect originated by a cluster is shown in Fig. 2.20. As a first approximation, a circular cluster can be treated as one big spot. Thus, in analogy with the spot's constriction resistance, the cluster resistance becomes

$$R_{\mathrm{cl}} \;=\; \frac{\rho}{4\,\xi} \quad , \tag{2.11}$$

where ξ is the radius of the cluster. Holm defines the cluster radius as the surface radius where all the spots are uniformly distributed. So the final constriction resistance is

$$R \;=\; R_{\mathrm{s}} + R_{\mathrm{cl}} \;=\; \rho\left(\frac{1}{4\,N\,a} + \frac{1}{4\,\xi}\right) \quad , \tag{2.12}$$

where a is the mean radius of a-spots and N the number of spots. Holm calculated an error of 10%. Greenwood estimated that this was pessimistic

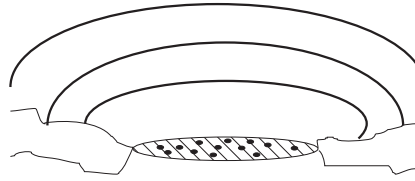

Fig. 2.20: Potential lines of the cluster current bend.

and that the error is smaller [30]. Greenwood's calculations also suggested that the details concerning the number and the spatial distribution of the a-spots are irrelevant for the evaluation of contact resistance in many applications where electric contact occurs reasonably uniformly over the nominal contact area. Greenwood defined ξ as *Holm radius*.

2.6.2 Greenwood's Calculation

Greenwood studied the influence between spots. Our scenario is a cluster that is far away from other clusters and whose size is small. Its dimensions are small enough to make the different spots interact between each other. The cluster consists of N microspots. The current flowing through k contact is I_k. In order to analyse the influence of the current, we define φ_{ij} $(i \neq j)$ as the influence on the spot i made by the current of the spot j. So φ_{ij} stands for the mutual resistance of contacts i and j, and the term φ_{ii} stands for the self-resistance of the contact i.
Greenwood determined that the influence of the spot j on the spot i is $\varphi_{ij} \sim \rho/2\pi S_{ij}$ where S_{ij} is the distance between the contacts. Also, if we suppose that the self-influence of a spot on its current is proportional to the self-resistance, then the self-influence of the spot i is $\varphi_{ii} \sim \rho/4a_i$.
For a cluster of resistances, the distribution of current is one that minimises the energy, or, in other words, the factor that minimises the heat generation.

$$W = \sum_i U_i I_i = \sum_{i=1}^{N} \sum_{j=1}^{N} \varphi_{ij} I_i I_j \quad . \tag{2.13}$$

When the spots are far apart they have no interaction between each other and the current through each spot will be proportional to the self-resistance inverse $1/\varphi_{ii}$ so $I_i \sim k/\varphi_{ii}$. Assuming this to be approximately true in the general case, the relation becomes

$$I = \sum_{i=1}^{N} I_i \sim k \sum_{1}^{N} \frac{1}{\varphi_{ii}} \quad , \qquad\qquad W = k^2 \sum_{i=1}^{N} \sum_{j=1}^{N} \frac{\varphi_{ij}}{\varphi_{ii}\varphi_{jj}} \quad , \tag{2.14}$$

and finally

$$R = \frac{W}{I^2} = \left(\sum_{i=1}^{N} \sum_{j=1}^{N} \frac{\varphi_{ij}}{\varphi_{ii}\varphi_{jj}} \right) \Big/ \left(\sum_{i=1}^{N} \frac{1}{\varphi_{ii}} \right)^2 \quad . \tag{2.15}$$

Bearing in mind the parameter values

$$\varphi_{ii} = \frac{\rho}{4a_i} \quad \text{and} \quad \varphi_{ij} = \frac{\rho}{2\pi S_{ij}} \qquad (i \neq j) \quad , \tag{2.16}$$

Eq. 2.15 becomes by substituting

$$R = \frac{\rho}{4\sum a_i} + \frac{\rho}{2\,\pi}\left(\sum_{\substack{i=1\\ i\neq j}}^{N}\sum_{j=1}^{N}\frac{a_i a_j}{S_{ij}}\right) \Big/ \left(\sum_{i=1}^{N} a_i\right)^2 . \tag{2.17}$$

Eq. 2.17 is called the position Greenwood equation. This expression is simple but for a big spot number its application is impracticable. If no correlation between the size of a contact and its position is assumed, the individual radii in the double summation can be replaced by their mean value. The equation of the resistance becomes

$$R \;=\; R_{\mathrm{s}} + R_{\mathrm{cl}} \;=\; \frac{\rho}{4\,N\,\overline{a}} \;+\; \frac{\rho}{2\,\pi\,N^2}\sum_{\substack{i=1\\ i\neq j}}^{N}\sum_{j=1}^{N}\frac{1}{S_{ij}}. \tag{2.18}$$

Where $\overline{a}$ is the mean contact radius. Eq. 2.18 is called the statistical Greenwood equation. Taking Eq. 2.18 into account and considering a cluster comprising a very large number of spots uniformly distributed within a circle of radius ξ (*Holm's radius*) the equation becomes

$$R \;=\; R_{\mathrm{s}} + R_{\mathrm{cl}} \;=\; \rho\left(\frac{1}{4\,N\,\overline{a}} + \frac{8}{3\,\pi^2\,\xi}\right). \tag{2.19}$$

Since $8/3\pi^2 = 0.2702$, this seems to be close to Holm's cluster equation 2.12. The cluster results obtained by Greenwood have been tested with different simulation tools and different empirical data [55, 56, 15]. Nakamura made an evaluation with a Finite Element Analysis (FEM) [55]. Clusters of two and four conducting spots were simulated. All the spots had the same radius and the distance between the spots was the parameter. All the simulations agreed with Greenwood's results.
H. Nishiyama made a thorough study using simulations methods [56]. A comparison between these equations and a simulation within a Boundary Element Method (BEM) was established. In the study the sizes of spots were varied as well as the distances between each other. For distances between

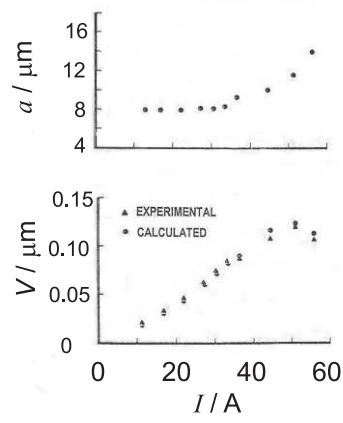

Fig. 2.21: Comparison between measured and calculated voltage vs. current. The voltage was calculated considering the variation of the a-spot radius according to the influence of the Joule heat [77, 71].

spots bigger than the double of their mean radius, the Greenwood and Holm equations agree with the real value.
Then the conclusion of Greenwood, Nakamura and Nishiyama was that the exact location of a-spots can be neglected when the a-spot distribution is not limited to the boundary of the apparent area. The results of the investigations mentioned above suggest that for many engineering purposes, a knowledge of the Holm radius may be sufficient to estimate the contact resistance.
Also, Timsit compared the results of the measured UI- curve with the standard Holm and Greenwood cluster equations [77, 71]. The results were that for a spot radius of about 50 nm the cluster models are not valid. With an a-spot radius of 8 µm the results fulfil the measurements. Moreover, Timsit tested the dependence of the spot radius on the contact temperature and current. In Fig. 2.21 we can find the measured and calculated voltage values vs. the applied current. In the upper graphic the mean a-spot radius is shown for different currents. The spot radius was constant up to a value of about 30 A.

2.7 Sliding Contact

Up to now the stationary contact has been introduced. The most part of its concepts also are applicable to the sliding contact [36, 34, 71]. In Fig. 2.22 a

comparison between a stationary contact and a sliding one is shown [80]. This test was done between Cu and Graphite. The parameters of the experiment were a speed of 2.6 m/s, a current density of 6 A/cm^2 and a contact load of 2.5 N/cm^2. Taking into account these measurements, we can see that the general behaviour of the contact is the same. The main difference between the two cases is that the voltage drop in the sliding contact is bigger. That also was measured in different research works [34, 71, 36].

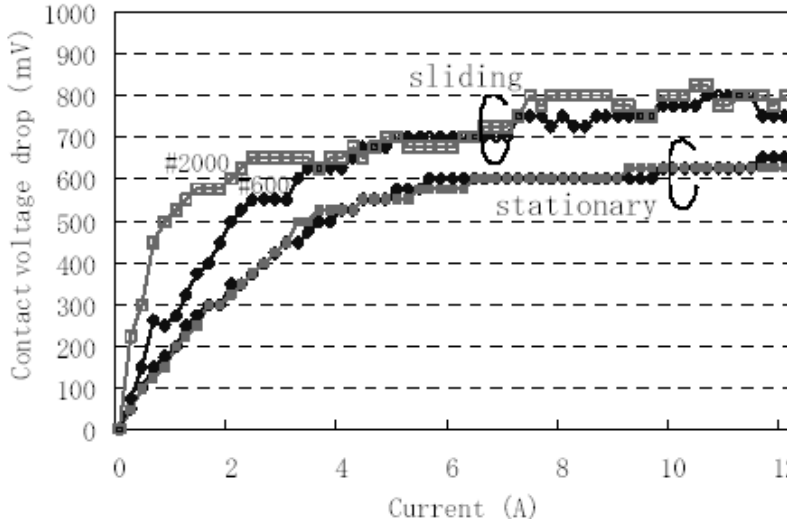

Fig. 2.22: Comparison curves of an stationary and a sliding contact. (Ar 80% + O_2 20%) [80].

In addition, the rotors were cleaned with different emery papers (#600, #2000). In the stationary contact, that is not relevant as far as results are concerned. In the sliding contact, differences appear at low currents. The contact voltage drop depends on the surface roughness conditions due to a low lubricating effect. A higher roughness leads to a higher clearing effect (wear). This great wear makes the oxide layer thinner [71, 36], and causes a greater number of lost particles [48, 27]. These lost particles make possible a major number of bridges between the surfaces. Therefore, there is a smaller voltage drop when the roughness of the surfaces is bigger. In the stationary contact this difference does not exist, as the clearing effect is not present.
A different effect can be observed at the higher range of currents. Considering this phenomenon, it can be supposed that the oxide film, which causes the lubricating effect, is hardly formed on the surface in low current levels.

When a high level of current is achieved, the oxide layer is wide enough not to follow the conductor surface roughness. So in both cases the oxide waviness is the same. The waviness of the surfaces was tested after the sliding with an O_2 atmosphere composition of 20%. The final waviness in both cases (#2000, #600) was the same.
Regarding the wear rate, a low friction coefficient is needed in order to have a lower wear rate. The tribological metal-metal contact does not fulfil this condition. In a common sliding contact, the rotor of a motor is always made of a metallic material. As the usual sliding contacts work in air, the oxide layer is present in the metallic surfaces. For example, two clean metallic surfaces sliding in vacuum will cold weld and in a short period of time the surfaces will be destroyed. This is true even for electrographite against electrographite. When the two surfaces are sliding, a cloud of dust appears and the surfaces are worn out in minutes [34]. Thus, an oxide film is needed, covering the contacting surfaces.
An oxide layer is needed on the surface, so that the fritting effect also is present on the contact behaviour. In addition, in a sliding contact the oxide influence causes two main differences described as follows:

- Friction is present on a sliding contact, so there is an extra heat source. At the same time, this oxide layer leads to a small friction coefficient. We have seen that this is a favourable factor. Furthermore, the friction heat is directly proportional to this coefficient. In practice, on a wide range of speeds, Joule heat has a bigger influence on contact temperature than friction heat [36, 45]. We have seen in Fig. 2.22 that not until the current reaches a certain value does the oxide appear on the surface. For applications where a large sliding speed is registered, this parameter has to be taken into account.

- A higher electric field is needed to establish an a-spot [34]. The time needed for an accumulation of charges on the oxide is smaller, so the accumulation rate on the contact time has to be higher. That corroborates the Ueno measurements mentioned before [80].

Another effect has to be taken into account, it is the electromigration. The oxide layer on the Cu surface is not regular, the big temperature on the track path makes the Graphite welt on the Cu surface. So the surface layer on the track is composed by different materials, some of them coming from the brushes (Table 2.2). This effect is increased by the wear, so this material transport is bigger in a sliding contact. Moreover, the conduction takes place through channels in which the temperature is high enough to release the oxygen [46] and also to result in an accelerated electromigration

Element	Cathode	Anode
Cl	32	40
C	109	117
Ag	26	53
O	39	53
Cu	63	93
Number of samples	5	6

Table 2.2: Average element composition[a] of slip ring track surfaces [38].

[a]The element composition is proportional to the atomic per cent.

of mass through the a-spot [65]. Thus, these channels are mainly composed of conducting materials.
A careful design of the brush holders also is needed. The mechanical aspects of sliding electric contacts play an important role [70, 71, 36].
Another difference between a stationary contact and a sliding contact is the form of the spots. In a sliding contact, spots have not a circular form [71, 36]. Johnson photographed a spot (Fig. 2.23(b)). The brush composition was 0.50 to 0.85 mass fraction of Ag. The current density was $75\,\mathrm{A/cm^2}$ and the speed was 13 m/s. The spot had an elliptical form and a contact spot ellipticity of $\gamma = 3$ was assumed. Other authors have derived formulas regarding the constriction resistance for rectangular spots [36]. However, the result is the same as the shape factor between the circular and the elliptical spot. In addition, the composition of the spot was analysed and it was found to be mainly Ag.
Other authors have observed the shape of the spots. Holm studied Cu-Graphite contacts, and determined that the value of the ellipticity was three. Timsit photographed a spot in a sliding contact with an ellipticity between 2 and 3 [78]. Furthermore, he photographed a spot in a stationary contact [77], and found it to be circular. Also, Kuhlmann photographed spots of a system in which the slide ring was Cu and the brushes Graphite-Ag [44]. She studied spots with different Ag compositions and the mean ellipticity was 1.6.
Johnson measured the chemical composition of the track [38]. The brushes had a 0.75 mass fraction of Ag. The mean composition of the track was tested with a SEM (Table 2.2). On both surfaces the C concentration was high, but the concentration of O was higher on the anode than on the cathode. The slip ring surface was composed by C, Cu, O, Cl and Ag.

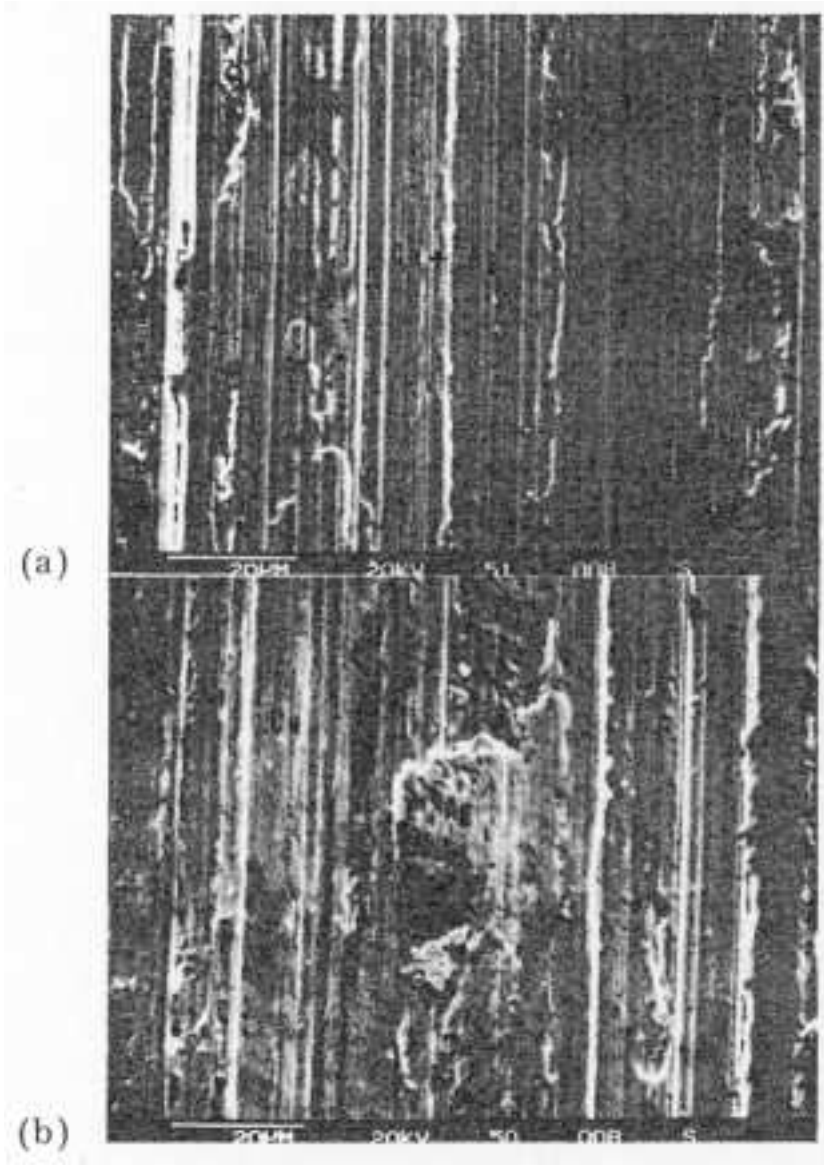

Fig. 2.23: Electron micrographs of slip ring inside the sliding tracks [38].
a) cathode track with Ag and Cu present at all locations.
b) anode track with Ag deposition in the centre of the photograph.

2.8 Parameter Transformation

The equations presented on the foregoing sections use constriction parameters, whereas the experimental test bench uses regulating ones. Then, the relation between these different types of parameters has to be explained. In the experimental set-up, we can regulate the temperature and humidity in the conditioning chamber and the rotating speed of the slip ring. Taking into account the previous sections, we know that the constriction parameters are:

- Oxide thickness t_{ox}
- Local temperature T_L
- Spot radius a
- Area of contact A_c
- Spot number N

whereas the regulating parameters are the ones that we use in our test bench:

- Load L
- Current I
- Ambient temperature T
- Humidity H
- Angular speed n

Fig. 2.24 shows a schematic of the transformation function. We need to obtain an applicable equation from the constriction theory. The resistance of the sliding contact is already obtained with its parameters. These constriction parameters are not measurable in a working system. Thus, if we obtain the transformation function from the environmental situation to the constriction, we can get the electrical system behaviour. The other option is to obtain the transformation function from the resistance with environmental parameters to obtain the constriction resistance. The system will be described by means of these equations.
This is not an trivial step, so it will be performed with different engineering tools and with some tests. In next section points, the different dependencies and tendencies will be presented.

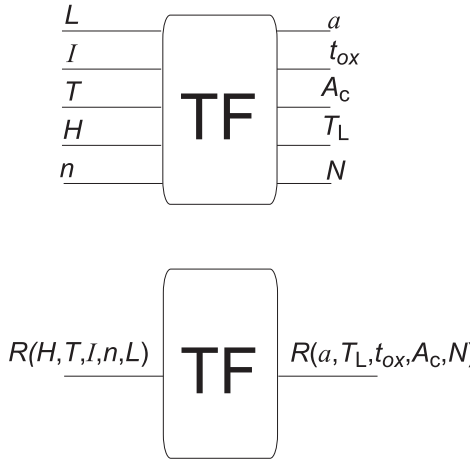

Fig. 2.24: Changes needed between theoretical and experimental parameters.

2.8.1 Film Thickness

The film thickness depends on the oxidation effect. During oxidation, the local temperature influences the oxidation of the material. The differences in film thickness for different humidities are explained by the existence of two different oxide layers [37, 26, 39].
The first one consists of oxide which is strongly attached to the collector ("thin film"). This layer will be oxide in air, but will contain Graphite, another lubricant and other substances which might be carried in the air [37]. Johnson measured this layer and it was about 1.5 to 3 nm thick [39]. It is believed that this film separates the brush from the slip ring in areas where elastic contact is made.
The second one is a "thick film" which results from occasional welds formed between the contact materials. This film is a moisture layer, composed of individual lumps of material whose thickness (0.5 to 150 µm) varies from place to place [39]. Gao measured this film and obtained a thickness bigger than 10 nm that was variable depending on humidity [26]. Johnson studied the influence of the load on this oxide film and determined that the increase of the load causes the breakage on the second type of surface film and a decrease in resistance. Gao and Kuhlmann studied these dependencies as well and confirmed Johnson's conclusions [26]. These results agree with results of crossed-rod experiments, revealing that contact film resistance increases when facing increasing hydrocarbon vapour pressure and decreases with in-

creasing load force.
In a sliding contact, the load is directly related to friction force. This friction force is responsible for the wear on the sliding contact. Due to this wear, small particles of the tarnish film are worn out. This wear out of the tarnish film originates a decrease of the oxide thickness. When applying a higher speed, the sliding surface suffers a bigger wear. Therefore, the angular speed is a parameter which determines this oxide thickness. Considering these observations, the oxide thickness function is

$$t_{\mathrm{ox}} = t(L, H, n) \tag{2.20}$$

2.8.2 Local Temperature

The influence of temperature has been studied in different research works. Johnson, for instance, studied its influence with a range of $20,600\,^{\circ}\mathrm{C}$ [39]. The dependence of the resistivity and the hardness of the materials on the temperature was tested. For a range of contact temperatures of about $155,614\,^{\circ}\mathrm{C}$, the contact resistance varied with $\pm\ 100\,\mathrm{m}\Omega$. The increase of temperature was originated due to friction (F_{r}) and the electric current, according to

$$T_L = T(F_{\mathrm{r}}, I). \tag{2.21}$$

The friction heat depends on the angular speed (n) of the sliding contact and the load (L). At low speeds, the friction heat can be ignored in favour of the Joule heat [34, 36, 45]. The heat produced within an a-spot can thus be dissipated by conducting through the bodies in contact, by the air and by each material.
Greenwood and Williamson observed contact temperature between stationary surfaces [31]. They found a surprising huge temperature on the contact surfaces. After this huge temperature was achieved, a decrease in resistance and in temperature was observed. The only plausible explanation found was the connection through small spots and the melting of the contact spots. As the spots melt, they grow from the initial channel size. There is a lower spot resistance, and a smaller current density exists on the spot. This smaller current density causes a smaller Joule effect and a lower temperature. In addition to this, Bowden and Williamson observed temperatures of about $950\,^{\circ}\mathrm{C}$ [14, 31]. These temperatures were registered in an Au-Au contact[3],

[3] the melting point of Au is 1063°C.

so there was not any oxide film between the conductors. This temperature also was reached with a voltage drop of 0.35 V. Holm had tested these parameters as well [34]. In view of these huge contact temperatures, the ambient temperature is not considered as a main parameter in the contact modelling [71, 34].
Greenwood and Williamson developed a wide theoretical approach to the problem. Nowadays, other authors such Timsit and Slade also have used this theoretical expressions [77, 71]. Timsit used Monte Carlo simulations to determine the growth of the a-spot radius depending on the current flowing through the contact. Timsit found out that currents below 30 A cause the growth of the spot until the a-spot radius is constant and about 8 µm.
Oebert and Isberg made some Finite-Element-Method (FEM) simulations of different a-spot radius and different materials [7]. They found out that pulses of 10^{-7} s and 122 A could readily cause maximum temperatures in the contact spot (with 0.5 V of maximal voltage drop). The maximum temperature increases with decreasing contact spot diameter. They tested the steady situation (with constant current), and the temperature was constant inside the spot. Zlonkiewicz reached the same conclusion after developing a mathematical model of the contact [82].

2.8.3 Radius of the a-spots

The radius of the spots is a function of the local roughness of the materials. In addition, we have to remember the existence of an oxide layer. The actual contact is made between the Cu oxide and Graphite. If we remember Fig. 2.22, the difference between the different polished sliding contacts becomes evident if the current through the contact is less than 4 A. As a higher current goes through the contact and a thick oxide layer is generated, there is no difference between the curves.
The mechanical parameters of surfaces, like Young´s modulus (E) and the radius of curvature ($4r$), are the relevant parameters to measure the form and size of the a-spots. The electrical and environmental parameters can cause an increase of the contact dimensions but only where materials are already in contact.
Malucci developed a statistical model in order to determine the size of the spots and its number [49].

$$a = \frac{A_c}{A_a} \frac{2}{W(e) < 1/M >}, \tag{2.22}$$

where a is the average size, A_a is the apparent area, A_c is the contact area, $W(e)$ is the probability density function that two protuberances could con-

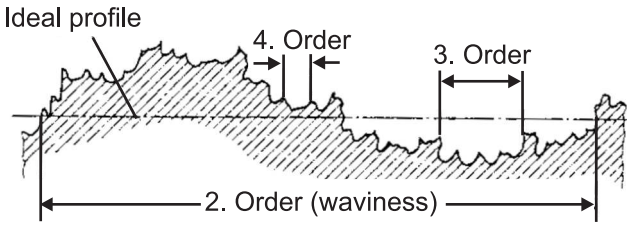

Fig. 2.25: Profile description with comparison of the different waviness orders [41].

tact, M is the sum of the surface protuberances and $< 1/\mathrm{M} >$ its inverse average. Malucci carried out Monte Carlo simulations varying the load and material surface characteristics (waviness, material). However, the existence of a surface film was not taken into account.
Slade and Timsit carried out some experimental observations and studied the influence of the mechanical parameters (radius of curvature r, Young´s modulus E, Poisson´s ratio ν). They found out a formula for the radius of an a-spot [71, 77]. If two elastic surfaces of radii of curvatures r_1 and r_2 are pressed together by a force L, the radius a is given by the expression

$$a = \sqrt[3]{r'L/K} \quad , \tag{2.23}$$

where

$$r' = r_1 r_2/(r_1 + r_2) \qquad , \qquad K = 4E/3$$

and

$$1/E = (1 - \nu_1^2)/E_1 + (1 - \nu_2^2)/E_2 \quad .$$

E_1 and E_2 are the Young's modulus and ν_1 and ν_2 are the Poisson's ratio for the materials of surfaces 1 and 2 respectively. In the presence of oxide films, the a-spots are formed through fissures in these films. Moreover, they found out that the a-spot radius in an Al-Al contact with a load of about 0.5 N has an initial radius of 2.9 µm and the a-spot grows to a limit of about 7 µm in an oxygen atmosphere.
Kragelskii developed another a-spot radius equation [43]. He calculated the compressive deformation a_i, which corresponds to the transition of a single

Slip ring Material	Diameter of the probe cm	Contact load N	Diameter of a-spots µm	Contact pressure 10^8 N/m^2
Cu	0.38	11.0	90 - 70	0.9 - 1.3
Cu	0.38	11.0	100	1.2
Cu	0.38	5.0	120	0.8
Cu	0.27	4.35	70	0.93
Graphite	0.5	6.0	126	0.63

Table 2.3: Spot diameter in the contact of an electrographite brush on a Cu or Graphite ring [34].

protrusion from an elastic state to a plastic one. The result is

$$a_i = 5.35(1-\nu^2)^2 Cr\frac{L\sigma_\mathrm{s}}{E^2} \quad , \tag{2.24}$$

where E is the Young's modulus of the material, r is the radius of the curvature of the lump, σ_s is the yield limit of the material, C is a form factor of the hump, L is the load and ν is the poisson's ratio. The a-spots radius was observed for different loads. Experiments show that the growth of the number of contact spots is considerably more intense than the growth of the area of a single spot.
Keil, Merl and Vinaricky did a wide research work [41]. The material surface was classified in different roughness orders as depicted in Fig. 2.25. In this figure the waviness orders 5 and 6 are not shown because they could not be drawn. According to this classification, they named the a-spots "micro-spots". This name comes from the order of magnitude of these finest contact areas. This conclusion was achieved considering the observations of Holm [34], Kragelskii and Demkin [43], as well as Bowden and Tabor [11]. The conclusion of the a-spot radius dependence to the load can be represented as follows

$$a_i \;=\; a_i(r_1, r_2, E_1, E_2, \nu_1, \nu_2) \backsim L_i^{1/3} \quad . \tag{2.25}$$

r_1 and r_2 are the radii of the micro-spots, E_1 and E_2 are the elasticity modules, ν_1 and ν_2 are the Poisson's numbers of the respective materials, L_i is the load on the contact area and a_i is the radius of the micro-contact area.
Dyson and Hirst studied the contact between two sliding surfaces in order to know the real contact area [23]. The implemented system was a metal-glass

surface. The contact surface of the metal was examined through the glass by phase contrast microscopy. The a-spots size was studied for different applied loads [15 − 30 N], using an Ag steel metal surface. It was concluded that, for different forces, the size of the a-spots was always about 3 µm. The differences registered using different loads resulted from the number of a-spots and not from their size [41, 11, 23]. In order to understand this behaviour, a plastic deformation of the contact areas was supposed. The conclusion was that the mechanism of friction and wear between mating surfaces under moderate loads takes place only in small sections of the apparent area. As the applied load is supported on a small A_c, the processes are essentially small in scale but severe in intensity.
Holm tested a Graphite-Cu system for a sliding contact (Table 2.3). He used a load range going from 4.35 to 11 N. We can observe that the number of spots is not a constant value. The sizes of the spots are always about a few microns.
Timsit made some measurements on aluminium cylinders [78]. The voltage drop across the contact was measured. The electrical couple was operated in a conditioning chamber filled with pure oxygen gas at a pressure of the order of 0.13 Atm. He could photograph a spot of about 20 µm of diameter and an ellipticity of 2.
As we have seen above, there are different formulas to obtain the spot radius. The different authors adjust their different model parameters to different observed measurements. Then, it has to be considered that the different parameters have a physical value. All these models are designed in order to adapt their parameters to an observed value. Any author who tried to model the electric contact would use these equations. These authors simply use an observed value or adapt their a-spot radius to a value inside a range in order to have good results. In both kinds of analyses, thermal-electrical

Reference	a-spot Radius µm	Material	Type
Öberg/Isberg [7]	10	Cu	Used
Timsit [77]	5-16	Cu	Used
Runde/Hodne/Totdal [64]	5-40	Al-Al	Observed
Kuhlmann/Makel [44]	12-30	Cu-Graphite-Ag	Observed
Timsit [79]	5·10⁻3- 10	Al-Al	Observed
Holm [34]	35-63	Cu-Cu	Observed
Binder [9]	7-50	Cu-Graphite	Used
Schreurs/Johnson [68]	50	Cu-Graphite-Ag	Observed

Table 2.4: Different a-spot radii.

and mechanical, the a-spot radius is about µm range. In Table 2.4 we can see different a-spot radii. Some of them are used in the calculations of different models or studies. The others are obtained by optical observations of the surfaces.

2.8.4 Contact Area

In fact, the true contact area is smaller than the apparent area in contact. Thus, a-spots must support local pressures that are comparable with the strengths of the materials of the contacting bodies [77, 34, 71, 38]. We have seen that the true contact area is determined by plastic deformation of the protuberances on the surface [12]. Under this assumption, the area of mechanical contact A_c is related to the load L applied to the electrical interface and to the plastic flow hardness H_m of the softer material as follows

$$A_c = A(H_m, L) = L/H_m \quad . \tag{2.26}$$

This expression affirms that the true area of mechanical contact between two surfaces is independent of the area of nominal contact of the surfaces. Moreover, the A_c depends only on the contact force and the hardness of the contacting bodies. A clarifying example of this can be established considering two interfaces made of identical materials and with identical surface roughness, but different dimensions (for example, $1\,cm^2$ and $100\,cm^2$). Both interfaces suffer the same load L. As the materials have the same surface roughness, they have the same density of surface protuberances. Thus, if the smaller contact is generated through contact by n protuberances, the larger interface is necessarily generated through contact by 100n protuberances. The average mechanical stress applied on each protuberance in the smaller interface is then L/n, whereas the same quantity in the larger interface is only $L/100n$. If the protuberance deformation is fully plastic, contact area at each protuberance in the smaller interface will be 100 times larger on the average than that of the larger interface. However, the total contact area is identical for both interfaces.
Holm deduced another similar expression in relation to the bearing area [34]. In order to infer this expression, Holm applied the same mechanical principles. The difference between Holm's equation and Eq. 2.26 lies in empirical observations and it is

$$A_b = \Upsilon \frac{L}{H_m} \quad , \tag{2.27}$$

where Υ is an empirical parameter. Finally, Holm calculated this parameter

for carbon brush on the collector $\Upsilon = [0.1, 0.3]$. We have to pay attention to the fact that Holm calculated this in relation to the bearing contact area. Greenwood and Williamson developed a model to show the dependence of the contact area on the contact load. They proposed a general formula as $A_c \backsim L^{\varsigma}$ [31]. By means of parameter ς, they could describe the cases in which there were plastic and elastic effects. When ς is about one, then a plastic behaviour is described by this last dependence. After wide empiric experiences, the ς calculated was 0.9.

2.8.5 Number of Spots

The number of spots (N) depends on two factors: the mechanical one (contact load, hardness) and the electrical one (fritting, current). The total number of spots is a result from the summation of the spots caused by mechanical contact and the ones caused by fritting.

$$N = N(\text{mechanical factors, electrical factors}). \tag{2.28}$$

The load applied on the two conductors makes the contact possible. This load has a direct influence on the A_c (Eq. 2.26). With a small load, there is a small number of "mechanical" a-spots. If the load is higher, this number increases. Another parameter to be considered is the breakdown of the tarnish films. The breakdown effect depends on the local electric field. This local electric field is a result of the relation between the tarnish film thickness, the incoming current, the surface waviness and the location of the spots. As the oxide thickness increases, the fritting effect decreases. The number and position of the spots together with the incoming current determine the electric field stresses on the tarnish film. Thus, the location of the spots is relevant as well. Thus, the number of nodes is

$$N = N(A_c, t_{ox}, I, S_{ij}) \quad . \tag{2.29}$$

Chapter 3

Numerical Verification of the Theory

3.1 Introduction

The theory presented on the previous chapter is based on measurements and observations. The calculations involved are plenty of approximations and hypothesis. Nowadays, there are simulation tools that allow us to examine

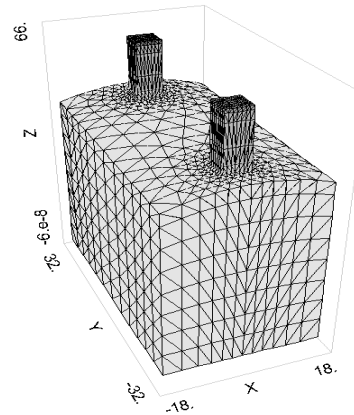

Fig. 3.1: Grid of the two brushes over a rotor in a three-dimensional simulation.

the validity of the approximations. All these points will be checked out through Finite-Element-Method (FEM) simulations. The software used is the FlexPDE tool. FlexPDE is a script-based finite element model builder and a numerical solver.
In the next sections, the theory previously presented will be verified in the same order to have an exact analogy. The first simulation is a circular spot in a two-dimensional Cartesian space. This simulation will be performed in order to corroborate that the constriction resistance is located in the closest area to the spot. The second model will be a circular spot in a three-dimensional space. The three-dimensional geometry is implemented in cylindrical coordinates. That allows us to perform the current integral, and consequently, to obtain the resistance value. The last model of a circular spot will be carried out in three-dimensional Cartesian coordinates. In order to validate this model and the theory, the constriction resistance values will be compared with the previous results. In order to finish the individual spot study, an elliptical spot will be simulated.
Afterwards, a cluster of spots will be implemented by using the previous three-dimensional Cartesian model. Therefore, the cluster resistance will be checked with different distances between spots.

3.2 General FEM-Simulation Characteristics

The theory deals with complex problems, so their mathematical formulation is tedious and is not always applicable. At this point, the use of numerical techniques is a good solution. FEM-simulation is a very powerful tool to get the numerical solution of complex problems. The basic concept is that a structure may be divided into smaller elements of finite dimensions called "Finite Elements". The original structure is then considered as an assemblage of these elements connected at a finite number of points called "Nodes". The properties of the elements are formulated and combined to obtain the behaviour of the entire body. Fig. 3.1 shows the division of two brushes with a slip ring into different "Finite Elements".
The equations of equilibrium for the entire structure are then obtained by combining the equilibrium equation of each element in such a way that the continuity is ensured at each node. The necessary boundary conditions are then imposed and the equations of equilibrium are solved to obtain the required quantities.
The fritting theory is developed in a resistance model with no time dependence, so we will simulate static situations. The implemented FEM model solves the Laplace equation for the electric potential (ϕ). As it is known, the particular solution of every problem depends on the boundary conditions.

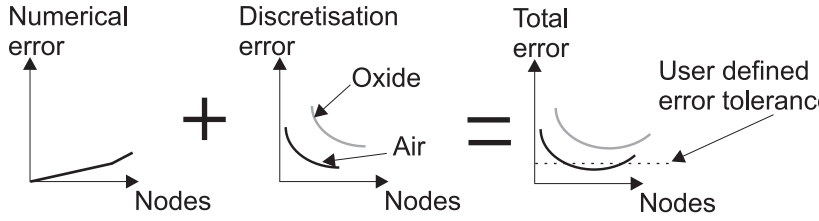

Fig. 3.2: Error as function of the node number.

Thus, on these calculations boundary conditions are playing an important role, and have to be defined accurately. The general electrical situation is a contact composed by two conductors: a brush (Graphite) and a rotor (Copper). The brush is always located on the upper part of the geometry and the rotor on the bottom part. Between the two conductors, there is an oxide layer crossed by a channel. This channel is the spot. Between the two conductors a potential is applied in distant zones from the oxide layer. Thus, the potential is applied on the top and the bottom of the geometry, and the oxide layer is located on the middle of the materials.
The different materials are defined by different conductivity and specific resistivity values ($\rho_{\text{copper}} = 1.7 \cdot 10^{-8}\,\Omega \cdot m$, $\rho_{\text{graphite}} = 3 \cdot 10^{-5}\,\Omega \cdot m$, $\rho_{\text{oxide}} = 0.02\,\Omega \cdot m$) [29, 28, 67]. Thus, the electric current flows through the spots and not through the oxide. Furthermore, the software does not allow us to use the current as a parameter. The current is a result from the electromagnetic simulation. The potential difference is applied between the two poles of the geometry, and, through integration, the current will be calculated. Moreover, each integration surface cuts the entire geometry horizontally. A succession of integrals has been calculated at diverse vertical points in order to verify the simulation. As it was mentioned on the previous paragraph, the program increments the number of nodes on all the space until the error in each piece is low enough. Thus, the node number is bigger near the spot (Fig. 3.4(a)). This increase is generated because of the more complex geometry in this zone and the bigger potential gradient. In addition, the integration surfaces are all horizontal but the current density is not always perpendicular to the integration surfaces. Near the voltage contacts[1], the current density is vertical, and the potential lines are horizontal. However, near the spot zone, the current density is not a vertical flux. This causes a worst integration value near the spot. Finally, the more inaccurate current values come from the integrals on the spot surface.

[1] Top and bottom of the geometries

The number of nodes increases as the complexity of the electromagnetic situations grows. A FEM-simulation divides the geometry in elements until the total error is below the simulation error tolerance. Fig. 3.2 presents the total error behaviour in relation to the number of nodes. The total error is a bathtub curve as a function of the number of nodes. The total error is composed by the numerical error and the discretisation error [52, 53, 54]. The numerical error comes from the calculation of the different matrix coefficients and their conditioning. Thus, the numerical error increases as the number of nodes rises. The discretisation error comes from the meshing of the geometry. A geometry is better described with a bigger number of nodes. Therefore, the discretisation error decreases if the number of nodes increases. Fig. 3.2 shows the effect of each error on the total simulation error. In addition, two different curves are depicted, one for a simulation with oxide layer and one for a simulation with air. The oxide layer brings more complexity to the meshing, generating more discretisation error. This causes two different curves, each one reaching different simulation minimums. The error tolerance is defined by the user. It is the level used by the simulator in order to know when the net refinement is sufficient. In these cases, the air simulation could finish, but the oxide simulation will never end.

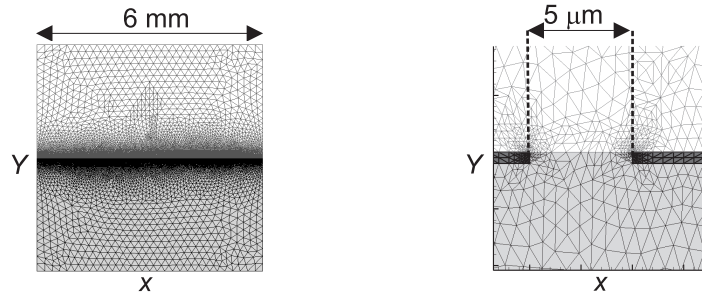

(a) General xy geometry.

(b) Zoom of the spot zone.

Fig. 3.3: FEM-simulation with oxide layer.

Therefore, in simulations of complex geometries, some simplifications have been made. In our research, the size of oxide thickness is tiny in comparison with all the other geometry sizes. This oxide layer does not influence the constriction resistance value, but influences the simulation. The FEM tool has to divide this layer in tiny pieces until the error is smaller than the total simulation error. The result is a huge number of nodes inside the oxide layer, that leads to a too big simulation error. Different solutions were tried, and finally, a void layer was implemented. So, there are no nodes inside the oxide

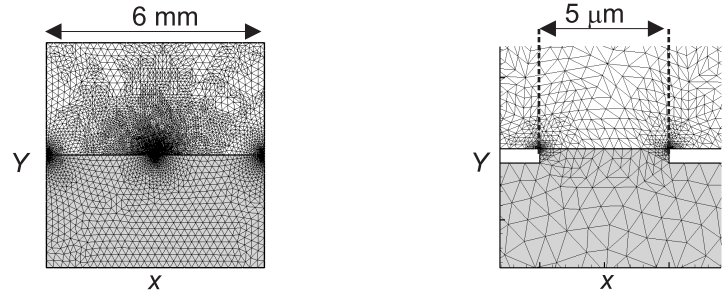

(a) General xy geometry.

(b) Zoom of the spot zone.

Fig. 3.4: FEM-simulation without oxide layer.

layer and the constriction resistance can be obtained.
An example is shown in Figures 3.3 and 3.4. On the one hand, the figures(a) show the general geometry of the simulation, and on the other hand, the figures(b) show a zoom of the spot zone. The brush is made of graphite and the rotor is made of copper. In both figures, the upper zone is the brush, and the bottom zone is the rotor. Between the two contact components, there is a spot and one oxide layer. The spot is located in the middle of a brush and a rotor. The sizes are the same as the ones present in the results (the spot radius was 5 µm, and the oxide layer thickness was 1000 Å).
Fig. 3.3 shows a simulation where the oxide layer is defined. Fig. 3.3(a) shows a dark zone around the entire oxide layer. The darkness is caused by the huge number of nodes in it. With this dimensions and the dark zone, it is difficult to distinguish the spot zone. Thus, a zoom was done in Fig. 3.3(b), in which the oxide layer can be seen. If we look carefully, it can be noticed that there are nodes inside the oxide. In addition, the density of nodes rises in the region of the spot.
Fig. 3.4 shows a simulation with an empty oxide layer. It shows no uniform dark zone near the oxide layer. In other words, the number of nodes around the entire oxide layer is not huge. There are only three dark zones: one in every corner of the brush or rotor with the air layer, and one in the spot zone. Fig. 3.4(b) shows a zoom of the simulation geometry where the oxide layer can be seen. Inside the oxide layer, there are no nodes. Outside the oxide layer, the number of nodes depends only on the external geometry, and not on the oxide thickness. This can be concluded from Fig. 3.4(a).
If we compare Fig. 3.3 and Fig. 3.4, there are big differences. Firstly, in the figures(a), where the dark zones are totally different. The one with oxide layer has a huge number of nodes around the oxide layer. The other has a

	Without Oxide	**With Oxide**
Nodes	7871	122285
Cells	3780	61082
Time / min : s	00:15	16:30

Table 3.1: Differences in a 2D-FEM-simulation with and without oxide layer.

huge number of nodes only when there is a corner in the geometry. Secondly, in the figures(b) the oxide layer has nodes or not inside. In the boundary layer between the oxide and the contact materials, there are big differences between the two geometries. The numerical differences between the two simulations are shown in Table 3.1. The increase in the number of nodes is about 1500 %. Moreover also the simulation time is different in both cases. These results are from a two-dimensional simulation, in the case of a three-dimensional one, the increase will be bigger. A more complex simulation using an oxide layer becomes an impossible task due to this huge increasing number of nodes. A simple three-dimensional simulation was performed with and without an oxide layer within a current could be integrated. In both simulations the current values were the same as the conduction is through the spot and not through the oxide.

3.3 Constriction Resistance of a Single Spot

The first equation to be tested is the constriction resistance of one spot. The first attempt is carried out considering a circular spot, so Eq. 2.5 is the first to be tested. This equation will be tested with three different geometries. As in our theory chapter, the first attempt is done with a two-dimensional model. This number of dimensions does not allow us to reach quantitative results. However, it brings us a clear electromagnetic situation and a qualitative resistance value. The second one is a three-dimensional simulation in cylindrical coordinates, taking advantage of the symmetry of the geometry. This model permits us to compare the values of the constriction resistance. The third one is a three-dimensional Cartesian model. In order to validate both three-dimensional geometries (cylindrical and Cartesian), the constriction resistance values should be consistent. Furthermore, this geometry provides us the possibility to test the equations for the elliptical spot and the cluster.

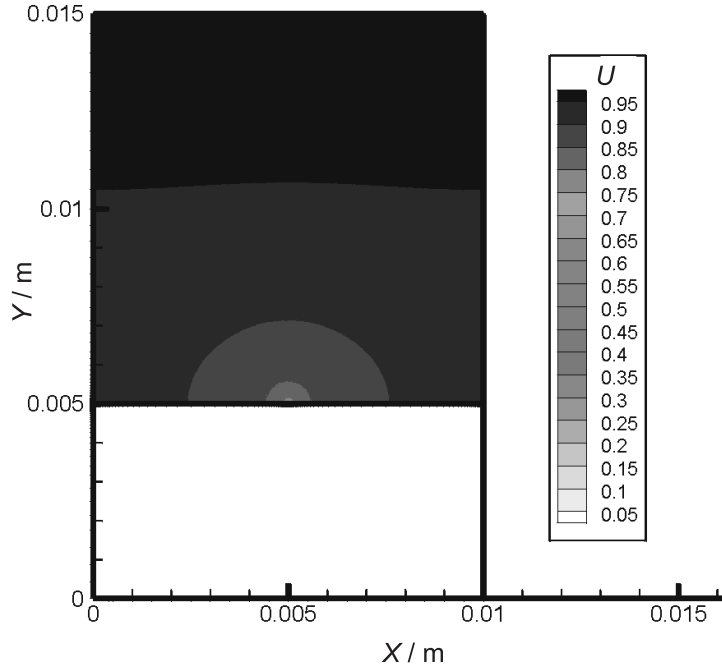

Fig. 3.5: FEM-simulation of one spot between a brush and a rotor.

3.3.1 Two-Dimensional Simulation

In order to prove the validity of the equations, a first step is to check the constriction resistance of a circular spot. A simulation was done with (x,y) as coordinates. The materials used were Cu and Graphite. The sizes in the simulation were: an oxide layer of 100 Åand a spot radius of 5 µm. A voltage of 1 V was applied between the upper brush surface and the bottom rotor surface.
Fig. 3.5 shows the potential lines between the two sides of the geometry. The potential lines are not distributed equally over the geometry. The majority of the potential drops in the closer zone to the spot, developing ellipses as affirmed by the constriction theory. The ellipses have the spot as their shared centre. Looking at the figure, it seems that the constriction resistance only exists in the brush, and not in the rotor. This is caused by the different material resistivities. The constriction resistance also exists in the rotor, but it does not appear in Fig. 3.5 because of its small value in comparison with the brush resistance.

In addition, we tested the differences in constriction resistance for different spot radius. As the spots radius grows, the constriction resistance decreases. That can be seen because the voltage drop near the spot zone decreases or, in other words, the ellipses decrease its height inside the brush, and increase its radius over the oxide layer. The limit case is when the spot radius is the simulated brush width. In this case, there are no ellipses, and the resistance is equal to an ohmic resistance described by

$$R_{\mathrm{Ohm}} = \frac{\rho \cdot l}{A} \quad . \tag{3.1}$$

3.3.2 Two-Dimensional Simulation using symmetry

A three-dimensional model was implemented in order to calculate the constriction resistance. The simulation was done in cylindrical coordinates. The limitation was that the geometries should have an axis of symmetry. With this implementation, the meshing was done in two-dimensions, and then the equations extended to three-dimensions. The advantage of this geometry is that it is based on a simple simulation. That leads to a quicker model development and a more exact simulation. The geometry was composed by three cylinders sharing the axis of symmetry. The rotor and brush were big cylinders in comparison with the spot. With this implementation, the current density has no phi component.
Fig. 3.6 shows the implemented geometry with an enlarged channel height. The depicted geometry range goes only from the axis of symmetry to the end of the geometry. So the line with r=0 constitutes the axis of symmetry. A voltage of 1 V was applied between the top and bottom surfaces. The spot radius was 5 µm, brush and rotor heights were 1 mm and their radii were 0.8 mm. As predicted in section 3.2, the number of nodes is bigger in the nearest zone to the spot. In Fig. 3.6, there are white lines crossing the graphic. They have been named on the right-hand side of the figure and ordered from top to bottom. These names mark the different integration surfaces. The program will integrate the current density over each surface to obtain the total current.
We are going to calculate the simulated and theoretical constriction resistances, and to compare their values. The theoretical calculations will be called analytical values, and they will be differentiated with the “ana” subindex. The simulation values come from a numerical solution, so they will be differentiated with the “num” subindex. The theoretical constriction resistance is calculated by way of Eq. 2.6, and it is

$$R_{\mathrm{c,ana}} = 1.500088\,\Omega \quad . \tag{3.2}$$

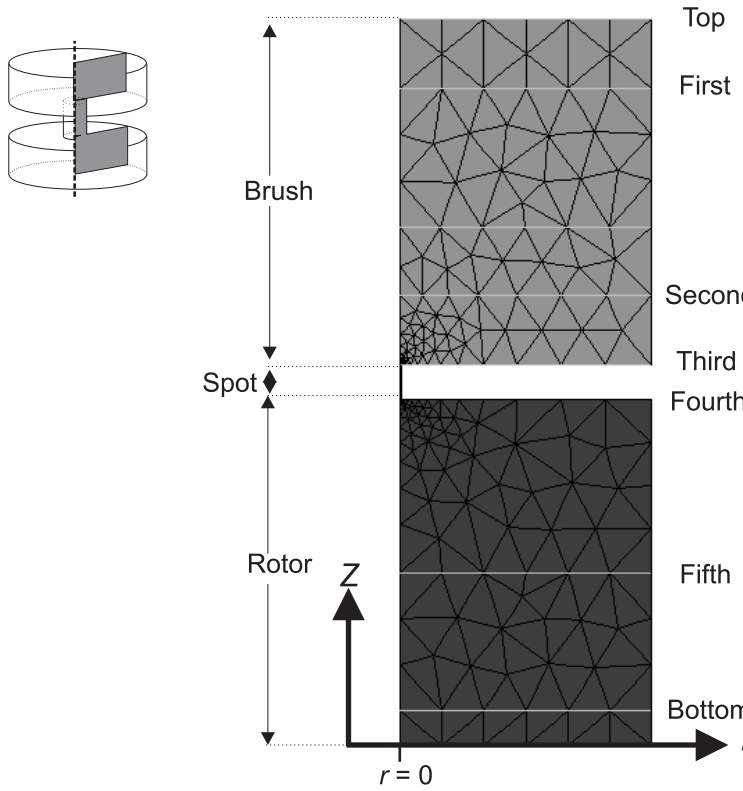

Fig. 3.6: Depicting of the contact geometry in the cylindrical coordinates case.

The total simulation resistance is

$$R_{\text{num}} = \frac{U}{I_{\text{num}}} \quad , \tag{3.3}$$

where U is the applied voltage, and I_{num} is the total current. This total current is the simulation current that results from integration. On the other hand, the total resistance is

$$R_{\text{num}} = R_{\text{Ohm,br}} + R_{\text{s,br}} + R_{\text{ch}} + R_{\text{s,rot}} + R_{\text{Ohm,rot}} \quad , \tag{3.4}$$

where $R_{\text{Ohm,br}}$ and $R_{\text{Ohm,rot}}$ are the ohmic resistances of the respective contact materials (not in the closer zone to the spot), $R_{\text{s,br}}$ and $R_{\text{s,rot}}$ are the

spreading resistances of the respective contact materials (Eq. 2.5), and R_{ch} is the resistance of the channel between the two materials. The channel resistance is

$$R_{\mathrm{ch}} = \frac{\rho_{\mathrm{ch}} \cdot t_{\mathrm{ox}}}{\pi \cdot a^2} \quad , \tag{3.5}$$

where t_{ox} is the oxide layer thickness, and ρ_{ch} is the specific resistivity of the channel material. The ohmic resistances are

$$R_{\mathrm{Ohm,br}} = \frac{\rho_{\mathrm{br}} \cdot l_{\mathrm{br}}}{A_{\mathrm{br}}} \quad \text{and} \quad R_{\mathrm{Ohm,rot}} = \frac{\rho_{\mathrm{rot}} \cdot l_{\mathrm{rot}}}{A_{\mathrm{rot}}} \quad , \tag{3.6}$$

where l_{br} and l_{rot} are the lengths of the ohmic part of the brush and rotor, A_{br} and A_{rot} are the areas of brush and rotor respectively. Finally, the constriction resistance is

$$R_{\mathrm{c,num}} = R_{\mathrm{s,br}} + R_{\mathrm{s,rot}} = R_{\mathrm{num}} - R_{\mathrm{ch}} - R_{\mathrm{Ohm,br}} - R_{\mathrm{Ohm,rot}} \quad , \tag{3.7}$$

and in addition, the error percentage is defined as

$$\%Error = 100 \cdot \frac{R_{\mathrm{c,ana}} - R_{\mathrm{c,num}}}{R_{\mathrm{c,ana}}} \quad . \tag{3.8}$$

Table 3.2 shows the simulation results. The I_{num} is the current obtained through the integrations. Thus, a value is given for every surface. The numerical resistance is

$$R_{\mathrm{num}} = \frac{U}{I_{\mathrm{num}}} \quad , \tag{3.9}$$

and it results from the simulation. $R_{\mathrm{c,num}}$ is the constriction resistance calculated from the FEM-simulation. The current values are all in the same range. There is only one current different of 0.66 A, and it is the current from the third integration area. This area is located exactly over the upper surface of the channel. In comparison with the other integration surfaces, this surface covers the bigger number of nodes. This node number increase is a consequence of the more complex geometry, as well as a bigger potential gradient. In a FEM simulation, it means a bigger number of finite elements, thus, a bigger number of equations to be solved, and finally, a bigger simulation error (section 3.2). The fourth surface is exactly below the channel. However, the third surface has a bigger error than the fourth integration surface, because the brush material has a bigger potential gradient. This bigger

potential gradient causes a bigger number of nodes, and a bigger numerical error. This is clear from Fig. 3.3 and Fig. 3.4. In addition, this also is clear from the simulation point of view. The FEM simulator solves the equation:

$$\triangle U = \nabla^2 U = 0 \quad . \tag{3.10}$$

As we have seen in Fig. 3.5, the voltage drop is mainly located in the brush side. So the complicated electromagnetical situation is located in the brush, and it is in this zone where the simulator has to solve more equations.
All in all, that the error is small enough to say the Eq. 2.5 describes the constriction resistance properly.

Integration Surface	I_{num} A	R_{num} Ω	$R_{\text{c,num}}$ Ω	**Error** %
Top	0.66570	1.50217	1.50216	0.1
First	0.66565	1.50229	1.50227	0.1
Second	0.66724	1.49871	1.49868	0.1
Third	0.65840	1.51883	1.51882	1
Fourth	0.66637	1.50066	1.50065	0.02
Fifth	0.66637	1.50066	1.50064	0.02
Bottom	0.66556	1.50249	1.50247	0.1

Table 3.2: Simulation values for the cylindrical geometry.

3.3.3 Three-Dimensional Simulation

A three-dimensional Cartesian model was necessary in order to check the previous model and the theory. Furthermore, it would be used to check the ellipticity factor and the cluster constriction resistance. These two cases cannot be checked with the previous geometries, as the geometry has not the same symmetry axis. Thus, the cylindrical model was no more applicable.
The geometry used was the same as the previous model: three cylinders connected by a common axis. This common axis also is each individual axis (Fig. 3.7).
There are two equal cylinders (brush and rotor) connected through the spot cylinder. The upper cylinder is the brush, and the lower one is the rotor. The brush and rotor radii were 3 mm, and the spot radius was 5 µm. As in the previous example, Fig. 3.7 shows ten integration surfaces. These simulations will have a bigger simulation error than the ones with the cylindrical geometry. This was a limitation caused by the huge number of nodes. The simulation time lasted for one weekend, because of the huge number of nodes.

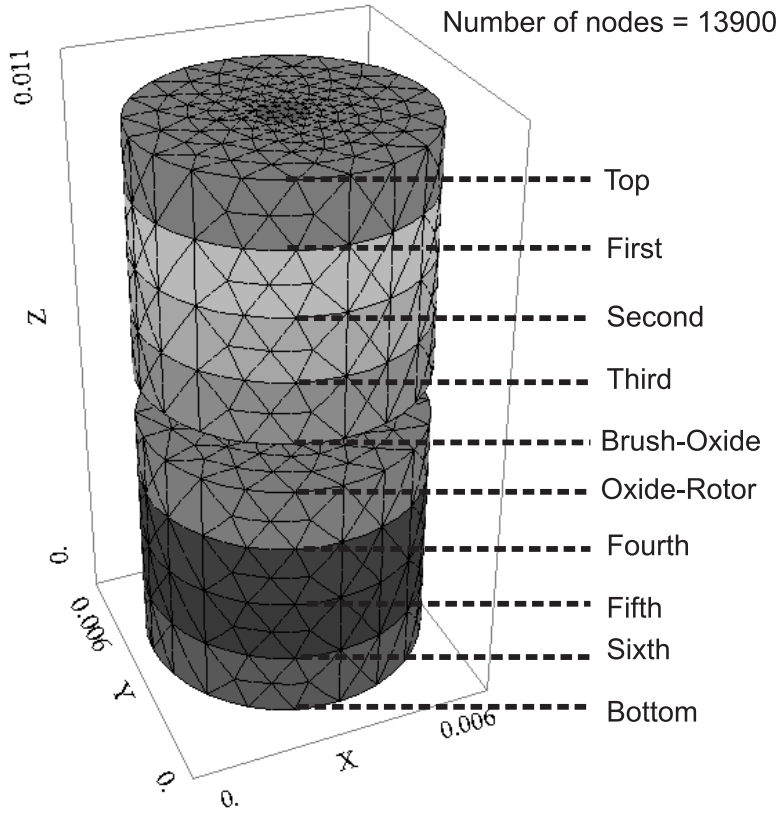

Fig. 3.7: Three-dimensional geometry in Cartesian coordinates. (number of nodes 138,000)

Table 3.3 shows the simulation results. The mean error of this table is bigger than the mean error of Table 3.2. If we remember that previous table, the mean current was about 0.66 A, and the most different current was 0.658 A. In this rectangular coordinates geometry, the smallest error is on the third surface. In addition, the mean error is smaller in the brush than in the rotor. On the other hand, the surfaces located exactly on the spot surface have a bigger error than all the other surfaces. In these surfaces, the number of nodes is bigger (Fig. 3.3(b) and Fig. 3.4(b)). This increase in the number of nodes is an exponential increase, so the error also increases in an exponential proportion. All these results conform to Fig. 3.2. The number of nodes in

Line of measurement	I_{num}	$R_{\text{c,num}}$	**% Error**
Top	0.68038	1.46954	2
First	0.68038	1.46954	2
Second	0.67744	1.47592	2
Third	0.66693	1.49919	0.1
Brush-Oxide	0.72689	1.37549	8
Oxide-Rotor	0.86824	1.15153	23
Fourth	0.61154	1.63499	9
Fifth	0.68998	1.44909	3
Sixth	0.68332	1.46321	2.5
Bottom	0.68138	1.46738	2.2

Table 3.3: Simulation values for the 3D geometry.

the rotor is smaller than that in the brush. The rotor is in the beginning of the curve, so the integration has a big error. The brush is in the middle of the curve and the third surface is in the valley of the error curve. Finally, the surface integrals present a huge increase of the node number, causing the biggest error. It can be concluded that the ideal integration surfaces are on the brush, in a vertical distance from the spot bigger than $200 \cdot a$.
In conclusion, the value differences between the simulations of the cylindrical geometry and the rectangular one are reasonable. Furthermore, both models are validated. As in the cylindrical simulation, the error is small enough to conclude, that Eq. 2.5 is a good description of the constriction resistance.

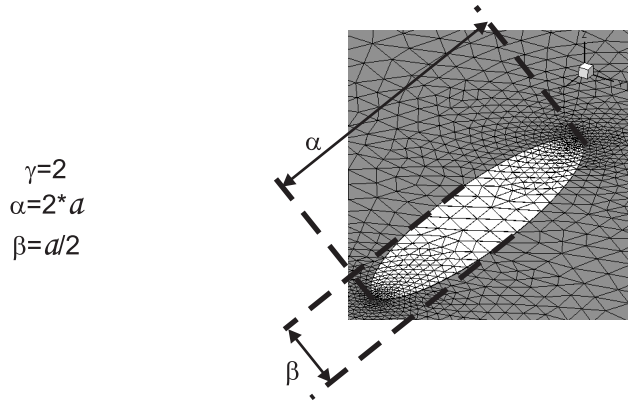

Fig. 3.8: Elliptical spot with γ=2.

3.3.4 The Ellipticity Factor

In order to verify the ellipticity factor, a three-dimensional simulation was developed. This simulation was performed with the previous geometry (Fig. 3.7), varying the spot form. The cylindrical spot was defined by its ellipticity γ. The spot is in this case a cylinder with elliptical base. Thus, the thickness of the oxide layer coincides with the height of the spot cylinder. The ellipses are defined by two different axes that are

$$\alpha = a \cdot \gamma \qquad \text{and} \qquad \beta = a/\gamma \quad , \tag{3.11}$$

where a is the spot circular radius. Fig. 3.8 shows an example with $\gamma = 2$, and $a = 5\,\mu\text{m}$. In this case, α is equal to $10\,\mu\text{m}$, and β is equal to $2.5\,\mu\text{m}$. As we can see, β becomes smaller as the ellipticity increases. Therefore, it was impossible to simulate ellipticity factors bigger than 10. When the ellipse axis was too small, the simulation could not conclude, because of the huge number of nodes. Leaving aside this limitation, the bibliographic sources give a γ range between three and six. Thus, it is a valid ellipticity range for our simulation model.

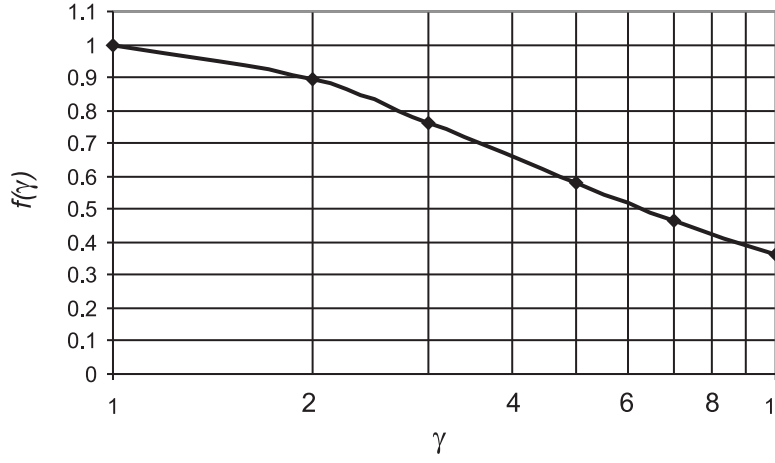

Fig. 3.9: Resistance ratio vs. ellipticity.

Other simulations were done with a fixed β, and an increasing γ. Therefore,

we could simulate approximated ellipticities from 10 to 100. The results with an increasing ellipticity confirm the theoretical predictions.
The total resistance value was obtained as in the previous simulations. The theory says that the constriction resistance of an elliptical spot is

$$R_{\mathrm{c}}(\alpha,\beta) = R_{\mathrm{c}}(\gamma) = R_{\mathrm{c}}(a)\cdot f(\gamma) \quad , \tag{3.12}$$

where $R_{\mathrm{c}}(a)$ is the resistance of a circular spot, and $f(\gamma)$ is an ellipticity factor. Thus, we want to obtain the ellipticity factor, and it is

$$f(\gamma) = \frac{R_{\mathrm{c,num}}(\gamma)}{R_{\mathrm{c,num}}(\gamma=1)} = \frac{R_{\mathrm{c,num}}(\gamma)}{R_{\mathrm{c,num}}(a)} \quad . \tag{3.13}$$

If we compare Fig. 3.9 with Fig. 2.17 (a representation of the theoretical study), we can see that they are equal. Finally, it could be affirmed that the constriction resistance of an elliptical spot can be described with the ellipticity factor correction.

3.4 Cluster Constriction Resistance

The constriction resistance of a cluster of spots remains yet to be checked. This is the final concept of the fritting theory. In this case, the constriction resistance has two terms: the parallel connection of individual spot resistances, and the term of the group effect. Different equations describe this behaviour (Eq. 2.12, Eq. 2.17, Eq. 2.18, Eq. 2.19), and we are going to study their validity.
We used a cluster composed by nine spots (Fig. 3.10). The spots were located in matrix form with d as the parameter. The distance between two adjoining columns or rows is always d. Thus, the distance between the spots (S_{ij}) is always a trigonometric function multiplied by d. The spots radius was 5 µm, and the radii of the brush and rotor were 5 mm. Fig. 3.11 shows an example of a nine spot's matrix. With this environment, all the explained cluster equations converge in Eq. 2.18. This equation covers only the constriction resistance of the contact, and this part is

$$R_{\mathrm{c,ana}} + R_{\mathrm{cl,ana}} = \underbrace{\frac{\rho_1+\rho_2}{4\,n\,a}}_{\text{individual effect}} + \underbrace{\frac{\rho_1+\rho_2}{2\,\pi\,n^2}\sum_{\substack{i=1\\ i\neq j}}^{n}\sum_{j=1}^{n}\frac{1}{S_{ij}}}_{\text{group effect}} \quad . \tag{3.14}$$

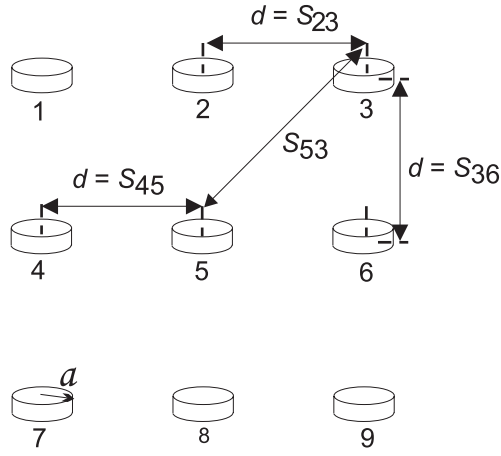

Fig. 3.10: Cluster of spots.

If we add to these constriction resistances the channel resistances, the equation becomes

$$R_{\mathrm{cl,ana}} + R_{\mathrm{c,ana}} + R_{\mathrm{ch}} = \frac{\rho_1 + \rho_2}{2\,\pi\,n^2} \sum_{\substack{i=1 \\ i \neq j}}^{n} \sum_{j=1}^{n} \frac{1}{S_{ij}} \; + \; \frac{1}{n} \left(\frac{\rho_1}{4\,a} + \frac{\rho_{\mathrm{ch}}\, t_{\mathrm{ox}}}{\pi\, a^2} + \frac{\rho_2}{4\,a} \right) \; . \tag{3.15}$$

In this equation, it is clear that the equivalent circuit is a cluster resistance in series with a parallel connection of the n-individual spot constriction resistance and the channel resistance.
The total resistance R_{num} was obtained using the same procedure as in section 3.3.3. The cluster term is our test goal, and the spots term is shared by all the equations. Thus, we can calculate the simulated cluster resistance as

$$R_{\mathrm{num}} = R_{\mathrm{Ohm,br}} + R_{\mathrm{Ohm,rot}} + R_{\mathrm{spots,ana}} + R_{\mathrm{cl}} \quad , \tag{3.16}$$

where $R_{spots,ana}$ is the part of the simulated resistance from the individual spot resistances, $R_{\mathrm{Ohm,br}}$ and $R_{\mathrm{Ohm,rot}}$ have the same definition as in Eq. 3.4, and R_{cl} is the part of the simulated resistance that comes from the group effect. $R_{\mathrm{spots,ana}}$ was tested in the previous sections. Thus, the spot term is

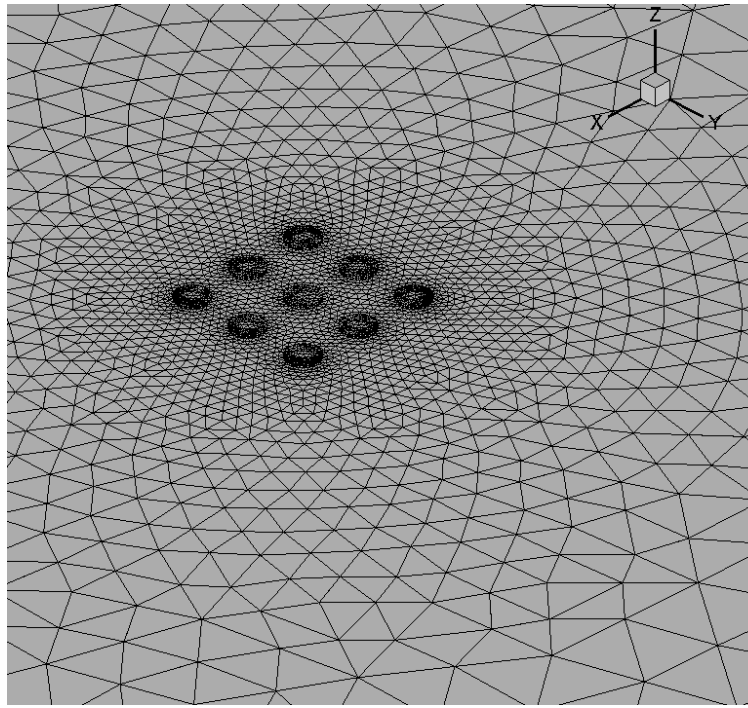

Fig. 3.11: Simulation of the spots cluster between brush and rotor.

assumed as

$$R_{\text{spots,ana}} = R_{\text{c,ana}} + R_{\text{ch}} = \frac{\rho_1 + \rho_2}{4 \cdot n \cdot a} + \frac{\rho_{\text{ch}} \cdot t_{\text{ox}}}{n \cdot \pi \cdot a^2} \quad . \tag{3.17}$$

R_{cl} is obtained from Eq. 3.16 and Eq. 3.17, and the result is given in Table 3.4. The simulation was done for two different distances between the spots in order to see their influence. The total current was obtained from an integration over the top surface. From these results, it can be concluded that the cluster term has a big influence in the total contact resistance. Moreover, it has to be said that the cluster dimension was small in comparison with all the contact area. Thus, its effect is bigger than in a real case. This was done in order to have a bigger cluster resistance value, and a smaller simulation error in it.
Now, the numerical cluster resistance is already obtained. In order to check the analytical cluster resistance, Eq. 3.14 has to be calculated.

d µm	**Total Current** A	R_{num} Ω	$R_{\text{cl,num}}$ Ω
$4{\cdot}a = 20$	3.251	0.31	0.139
$6{\cdot}a = 30$	3.835	0.26	0.091

Table 3.4: Results from the cluster simulation.

The cluster resistance depends on the sum of all the inverses of distances between the different spot couples. We calculated this formula with d as parameter. With our matrix implementation, the result is

$$\sum_{\substack{i=1 \\ i\neq j}}^{n}\sum_{j=1}^{n}\frac{1}{S_{ij}} = \frac{47.198}{d} \quad . \tag{3.18}$$

From Eq. 3.14 and Eq. 3.18, we can express the theoretical cluster resistance as a function of d, and it becomes

$$R_{\text{cl,ana}} = \frac{(\rho_1+\rho_2)}{2\,\pi\,n^2}\sum_{\substack{i=1 \\ i\neq j}}^{n}\sum_{j=1}^{n}\frac{1}{S_{ij}} = \frac{47.198\cdot(\rho_1+\rho_2)}{2\,\pi\,n^2\,d} \quad . \tag{3.19}$$

From this theoretical calculation, we can obtain the cluster resistance on the brush ($R_{\text{cl,Br}}$) and on the rotor ($R_{\text{cl,rot}}$). Moreover, the total cluster resistance is calculated in the theoretical case and in the simulation one (Table 3.5). In this table, the error is calculated using the analytical solution (with the theoretical equations) and the numerical (FEM-simulation), and its percentage becomes

$$\%Error = 100\cdot\frac{R_{\text{cl,ana}} - R_{\text{cl,num}}}{R_{\text{cl,ana}}} \quad . \tag{3.20}$$

d µm	$R_{\text{cl,Br,ana}}$ Ω	$R_{\text{cl,rot,ana}}$ Ω	$R_{\text{cl,ana}}$ Ω	$R_{\text{cl,num}}$ Ω	**Error** %
20	0.139	$8.133{\cdot}10^{-5}$	0.139	0.137	1
30	0.093	$5.422{\cdot}10^{-5}$	0.093	0.091	2

Table 3.5: Cluster resistance comparison between simulation results and analytical calculations.

At first glance, the cluster resistance on the brush side is three orders of magnitude bigger than that on the rotor side. This is the same result as the

one reached in the spots resistance. The cluster resistance increases with decreasing distance, taking into account that the number of spots remains constant. This was already mentioned by Greenwood: if the spots are located closer to each other, they act like one big spot. In this case, the cluster resistance is equivalent to the big spot resistance. The errors are 1 % and 2 %, so they can be assumed as small enough.
The final error is always below the one predicted by Holm (10 %). All these conclusions confirm the results of Nishiyama and Greenwood [30, 56, 15]. These results let us conclude that the constriction resistance theory is applicable to the electric contact problem.

Chapter 4

Test Bench

4.1 Introduction

The investigation in this project is a combination of theoretical basis, experimental measurements, and their application in a contact model. This chapter deals with the experimental set-up, the involved parameters, definition of the test algorithm and the different measurements. At first, the experimental set-up will be introduced, in which the measurement circuit will be explained with special consideration to the signal measurement. This circuit is the origin of all the other experimental characteristics. Our experimental set-up comprises the different test devices, ports used and programs developed. The different test devices will be described, listing the different hardware and software components. Afterwards, the different involved parameters are listed, giving the test ranges for the diverse quantities.
Secondly, the test definition will be elaborated, beginning with the reproducibility test. An experimental set-up has to be checked in order to have reliable measurements, but in our test the environmental conditions also are research parameters. The warm-up time will be defined as the time which the system needs to reach a stable situation. Thus, the warm-up time will be checked. After the warm-up time determination, the test bench reproducibility will be tested. Then, a first test will be done in order to check the special effect of the constriction theory as the hysteresis cycle, and to get familiar with the test process. Then, the error calculation will be explained, taking into account the already introduced measurement characteristics. The test program will be introduced as final step of the test definition.
Finally, the measurements will be presented, introducing the parameter ranges. A measurement example will be explained as first step, in order

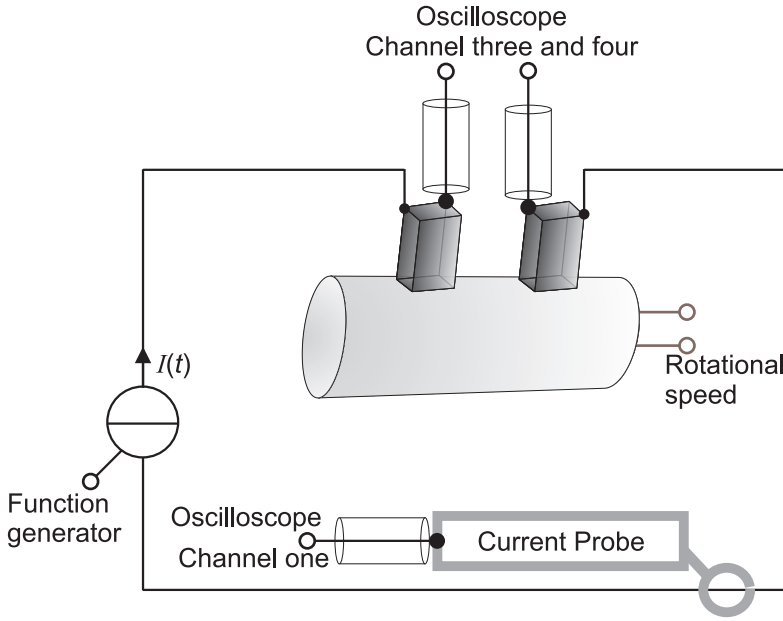

Fig. 4.1: Test circuit.

to describe the measurement characteristics. Afterwards, a presentation of the systematic measurements will be performed. The results also will be presented with a tendency analysis in order to present a synthesis of the result conclusions. The tendency analysis will be introduced with an example. Finally, the results of the tendency analysis will be presented, and the observed tendencies summarised.

4.2 Experimental Set-up

The target of the test is to measure the voltage drop in the brushes. The measurement is done in a moving system with a small range of the voltage drop. Thus, the noise of the signal must be minimised, and in this point the ground of the system is a critical point. With this limitation, all the devices used in the electric circuit are isolated through a transducer. Thus, there are galvanic connections between inputs and outputs. The electric circuit is the base of the test set-up. Fig. 4.1 shows the scheme used in the test. The signals in the channels three and four are the voltages between the brushes and the oscilloscope ground. The voltage is measured in a differential form, so the

Signal	Function
Channel 1	Current in the brushes
Channel 3	Cathode (minus brush)
Channel 4	Anode (plus brush)
Trace A	Current mean
Trace B	Channel 4 - Channel 3
Trace C	Mean of the Trace B

Table 4.1: Oscilloscope set-up

voltage between one brush and the sliding ring is 0.5 times the difference of channel four and three. With this situation, the oscilloscope plays an important role. We are using different functions of the device in order to read the mean voltage drop between the brushes (Table 4.1). Finally, we read out the *Trace A* and *Trace C*, and their statistical errors.
Fig. 4.1 also shows a current source. The output of the current source is isolated from the input through transducers. It is controlled by a DAS (Data Acquisition System), which also has galvanic connections made by transducers.
The measurements have to be time effective due to their quantity and the duration of each test. Automatised tests are a good solution in order to take benefit from all the possible testing time. The automatisation comprises the configuration of the different devices, as well as the value generation of the different parameters for each test. In addition, different parameters can be monitored during the long-time tests in order to avoid possible errors. For example, this is necessary in order to be sure that the environmental situation is constant. Therefore, it is important to automatise all the tasks. The use of one device that performs all these tasks is expensive. A better solution is to have a group of commercial devices, that each one controls different variables. In order to coordinate all these devices, the test bench is controlled by a personal computer. A Labview program was developed in order to regulate and to read out all the different devices. This program has to configure the rotor speed, the climate chamber and the oscilloscope. In addition, it monitors all the environmental parameters in order to assure a constant situation. The program tasks have the following order:

- regulating the desired environmental and electrical parameters
- waiting till the desired time or a desired situation is accomplished
- controlling the constant environmental situation
- measuring all the parameters from our different devices

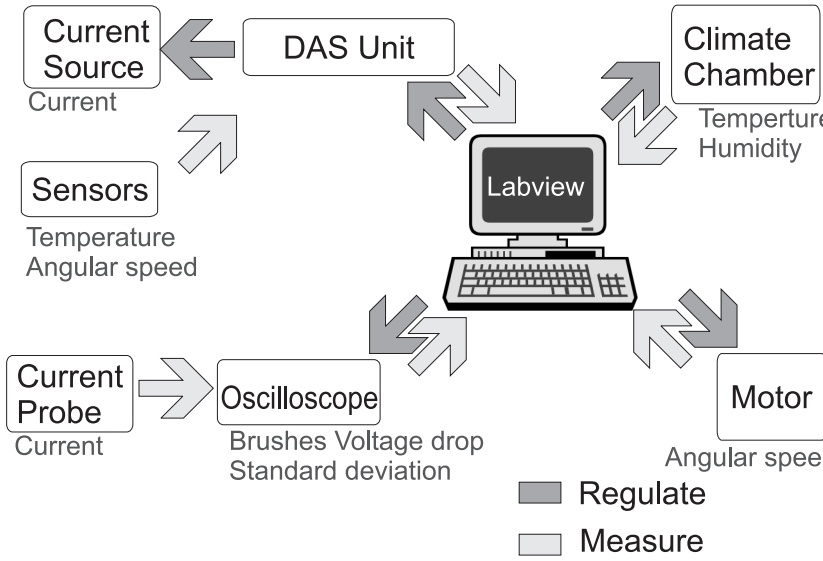

Fig. 4.2: Depict of the different test devices and their connections.

The regulating parameters are: humidity, temperature, rotor speed and current. In order to regulate the desired situation, the computer communicates with the devices presented in Fig. 4.2. The arrows indicate in which mode the devices are operating. The arrows going from the computer to the devices are regulating messages. The arrows going from the devices to the computer are measuring messages. The devices operate as measuring and regulating units depending on the computer messages. Four computer ports are used (USB, two serial ports and GPIB). In the regulating part, the climate chamber plays an important role because it controls the temperature and humidity. In order to generate a desired current value, we use a current source controlled by its analog port. This analog port is controlled by the DAS.

The DAS is a multifunction data acquisition system. This unit can communicate with the PC over the Universal Serial Bus (USB), providing a convenient alternative to plug-in data acquisition boards. This bus supports a wide range of peripherals, and also supports an input-output analog port. After accomplishing a full designed set-up, a first test was done with a specially designed device (Fig. 4.3(a)). This device comprises a copper rotor, the couple of brushes, and their holders. This implementation had not the proper mechanical conditions in order to have a good brush-rotor contact.

The brush holder has to catch the brush, leaving it a little bit loose. This is necessary in order to have a good adaptation of the brush to the rotor surface. Moreover, the brush holder has to avoid the friction-excited vibration range. The friction-excited vibration range produces the brushes chatter of the brushes and a bad contact [71, 34, 36, 37]. The brush has to make contact to the rotor within an angle range, and not in a perpendicular way. This first brush holder did not agree with both requirements. After trying different solutions with this implementation, it was not possible to fix the noise problem. The solution adopted was to use a commercial generator (Fig. 4.3(b)), in which the two slip rings where connected. Thus, the commercial generator has the same electric circuit of the specially designed device (Fig. 4.1).

(a) First implementation: specially designed device.

(b) Second implementation: commercial generator.

Fig. 4.3: Different implementations of brush-slip ring devices.

4.2.1 Involved Parameters

The systematic measurements have to deal with the test bench parameters. Firstly, we will clarify the parameters that we can read. Secondly, we will see the parameters that we can regulate. Table 4.2 shows our measured parameters and the respective devices. So, we can read five parameters with different devices, and by using four computer ports. We can read different types of parameters which complicates the coordination of the program. The

Parameter	Device	Computer Port
Current	Oscilloscope	GPIB
Brush voltage		
Humidity	Climate chamber	LPT1
Ambient temperature	Climate chamber & DAS	LPT1 & USB
Speed	Motor & DAS	LPT2 & USB

Table 4.2: Measuring parameters.

measuring parameters are

- climatic parameters: temperature (10-90 ˚C) and humidity (10-90 %)
- mechanical parameter: angular speed (600-3000 rpm)
- electrical parameters: current (0-5 A) and voltage drop.

We emphasise that there are two parameters controlled by two units. The ambient temperature and angular speed could be read by different devices, while each is regulated by one device. The angular speed is regulated by the motor, and it can be read by the motor and the DAS unit. The ambient temperature is regulated by the climate chamber and can be read by the climate chamber and by the DAS unit. Thus, both parameters are controlled by the DAS unit. This possibility is used by the Labview program to control the proper function of climate chamber and motor.

Parameter	Device	Variation Range
Ambient temperature	Climate chamber	15 to 90 ˚C
Humidity		15 to 90 %
Speed	Motor	0 to 3000 rpm
Current	Current source (through DAS unit)	0 to 20 A

Table 4.3: Regulating parameters.

So the computer is connected to four machines: DAS, climate chamber, motor and oscilloscope. At the same time the DAS is connected to the current source and to two different sensors (temperature and angular speed sensors). The different ports are presented in Table 4.2. The communication with the climate chamber was done with a special cable and a special library function. The handshaking was not a standard one, so it had to be extracted from a C++ example, read directly from the port, and implemented bit to bit in Labview. The oscilloscope was configured with its standard library

functions. That was a good solution in order to have a quick and exact development of the oscilloscope configuration. The DAS could be configured by Labview standard libraries. The motor could be configured with an standard serial port protocol. After controlling the devices, the waiting time, stop and security modules have to be developed. Finally, the result was a big library, comprising more than 100 modules.
The test bench comprises measuring and regulating parameters, Table 4.3 shows the regulating parameters, devices and working ranges. Four parameters can be regulated through three units. Thus, all the regulating units can also read out their regulating parameters. The climate chamber has a range for humidity from 15 to 90 % and for temperature from 15 to 90 °C. The motor can be static and reaches a maximal angular speed of 3000 rpm. The current source has an output range from 0 to 20 A
All the set-up was implemented in order to have an totally automatic test bench, measuring all our results while other research tasks could be completed. Unfortunately, these tests cannot be full automatic because of two reasons: firstly the climate chamber cannot be switched on and switched down through the port, and secondly the motor has not a remote reset. For the first one reason, the climate chamber has to be switched on by hand. Also, there are some errors that don't cause an error message, for example in the case of no water in the tank, there is no remote information message. The second reason can seem a little bit strange but the motor could have a different kind of error as high temperature or too much force moment. Thus after an error occurs, the motor has to be changed by hand.

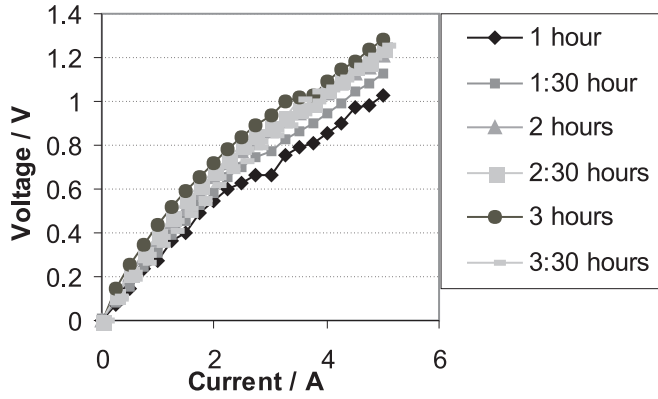

Fig. 4.4: Different UI-curves with different warm-up times.

4.3 Test Definition

The contact model has to be based on several measurements. Each measurement has to be done on the same form as the others. In addition, the analysis of the measurements has to be always exactly the same, in order to compare and interpret the results properly. The measurement steps are prone to human errors, even if the different tests are done within a wide time range. In this section, the different steps done will be explained in order to maximise the test automatisation. Also, a first test is presented as an example. This test was a good experience, in order to plan the systematic measurements, and to test an up to now unchecked point of the theory (hysteresis cycle). Finally, a first measurement example is presented, including the measured values and their analysis.

4.3.1 Warm-up Time and Reproducibility

After determining the test parameter, the goal is to develop a reproducible test. So the first point was to determine which time the system needs in order to have a stable environmental situation. This time is called warm-up time. Different bibliographic values were studied. Fig 4.4 shows different curves at different warm-up times. For warm-up times from one hour to one hour and a half, the voltage drop varies and increases with the waiting time. After more than two hours, the increasing tendency disappears and the voltage drop reaches a constant voltage. The variations are caused by the differences on the contact surfaces. Some other authors developed a similar stabilisation time [63, 21].

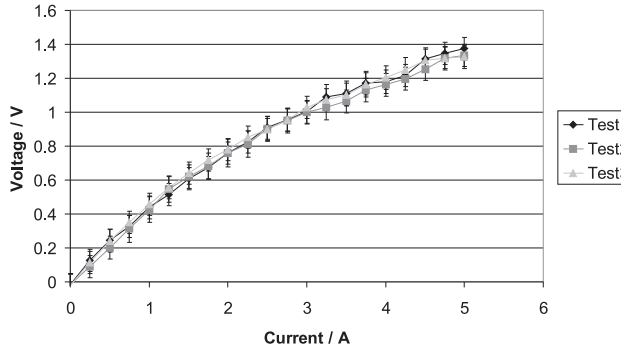

Fig. 4.5: Reproducibility of the data.

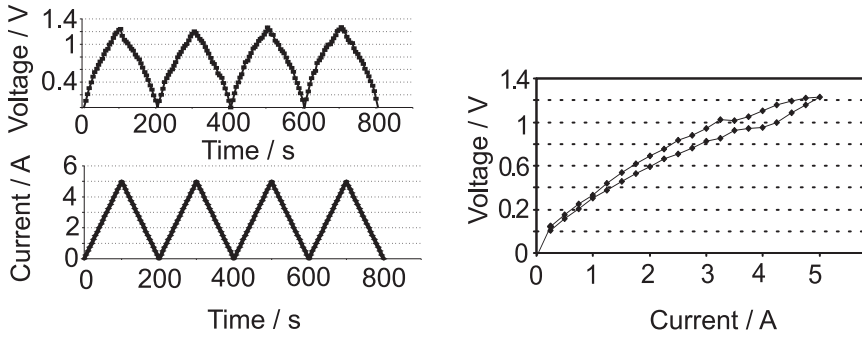

(a) Triangular periodic signal.

(b) UI-Curve.

Fig. 4.6: Test of increasing and decreasing ramps.

From the time where the environment time is established, the reproducibility could be tested. Fig. 4.5 shows different measurements made on different days. The test machine was stopped and switched on for the next test. The time between the first and the second test was one day. The time between the second and the third test was five days. The bigger difference between values is 4 %. Thus, we can reproduce the same measurement on different tests with 4 % of reproducibility.

4.3.2 First Test

A first test was planned in order to become confident with the test bench and its programs. In addition, it is used to check a theoretical point. This theoretical point deals with the creation and disappearance of spots. The spots are created as the electric field increases on the oxide layer. Then, if we make a decreasing ramp the voltage will be smaller than in the increasing ramp [34]. Thus, we decided to measure two UI-curves, one with ascending current and one with descending current. The signal made was a triangular current signal in the time. Finally, the UI-curve will be extracted in order to check the theoretical point. Fig. 4.6(a) shows the current vs. time and the voltage vs. time. Four triangle signals were measured in order to test if there is a difference between the first triangular signal and the following ones. Sometimes, there were some differences between the different triangular ramps but in general, these differences were small. We considered each increasing and decreasing ramp couple as a frame. Finally, we used these four frames in order to calculate the mean value and the statistical variation between frames. This statistical variation between frames can be seen as an

signal error. Fig. 4.6(b) shows the UI-curve from these mean values. This figure presents a hysteresis curve. In all our tests, the upper curve corresponds to the increasing current ramp, and the lower curve corresponds to the decreasing current ramp. This can be explained with the constriction theory as follows: the spots need an electric field value in order to be formed. The number of spots grows as the electric current increases. In the first moment, when the electric current is reduced the spots are already formed, and the resistance is always smaller as in the creating spot case.
After this point, the hysteresis cycle is checked. The UI-curves present on the bibliography are composed by increasing ramps. Then, the measurements will be done only with increasing ramps of current. Thus, the next curves represent the higher curve in the hysteresis cycle.

4.3.3 Error Calculation

The measurement error has to be calculated in order to have a range of accuracy [75, 60, 3]. Fig. 4.7 gives the schematic of the measurements. The measured voltage has a variation due to the movement of the rotor and brushes. Thus, the oscilloscope calculates the mean and the deviation of the measured voltage. This mean voltage is produced by the general contact situation that is determined by the environmental situation. During the time in which the oscilloscope calculates the statistical values, the current is constant. Thus, the current is varied in steps. Each measured value from the oscilloscope is given by

$$U_i \pm \triangle U_i \quad , \tag{4.1}$$

where U_i is the mean voltage value calculated by the oscilloscope, $\triangle U_i$ is its

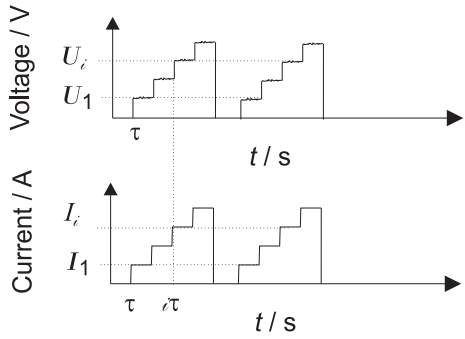

Fig. 4.7: Schematic of the measurement signals.

standard deviation, and i is the index of the measured point (we measure 84 points, 21 in each frame). The mean voltage calculated by the oscilloscope is

$$U_i = \frac{1}{\tau} \int_{i\tau}^{(i+1)\tau} U(t)dt \quad , \tag{4.2}$$

and the standard deviation is

$$\triangle U_i = \sqrt{\frac{1}{\tau} \int_{i\tau}^{(i+1)\tau} (U(t) - U_i)^2 dt} \quad . \tag{4.3}$$

The standard deviation which corresponds to the oscilloscope also was measured in order to have a complete error calculation. The measurements are done with four frames $f = 4$. Firstly, the mean voltage value $\overline{U}$ has to be calculated for each discrete current value as

$$\overline{U(I)} = \frac{\sum_{f=1}^{4} U_i(f, I)}{4} \quad , \tag{4.4}$$

where f is the variable counting the number of frames, and I is regarded current value (in each frame). So, this calculation will be done for the 21 points towards each frame. The statistical error between the frames is defined as

$$\psi(I) = \sigma(I)^2 = \frac{\sum_{f=1}^{4} (U_i(f, I) - \overline{U(I)})^2}{4 - 1} \quad . \tag{4.5}$$

The mean systematic error will be calculated as the mean error of the measurements, as

$$\overline{\triangle U(I)} = \frac{\sum_{f=1}^{4} \triangle U_i(f, I)}{4} \quad . \tag{4.6}$$

The error coefficients were calculated as the quadratic sum of the statistical and systematic errors as following

$$\Lambda(I) = \sqrt{\psi(I)^2 + \overline{\triangle U(I)}^2} \quad . \tag{4.7}$$

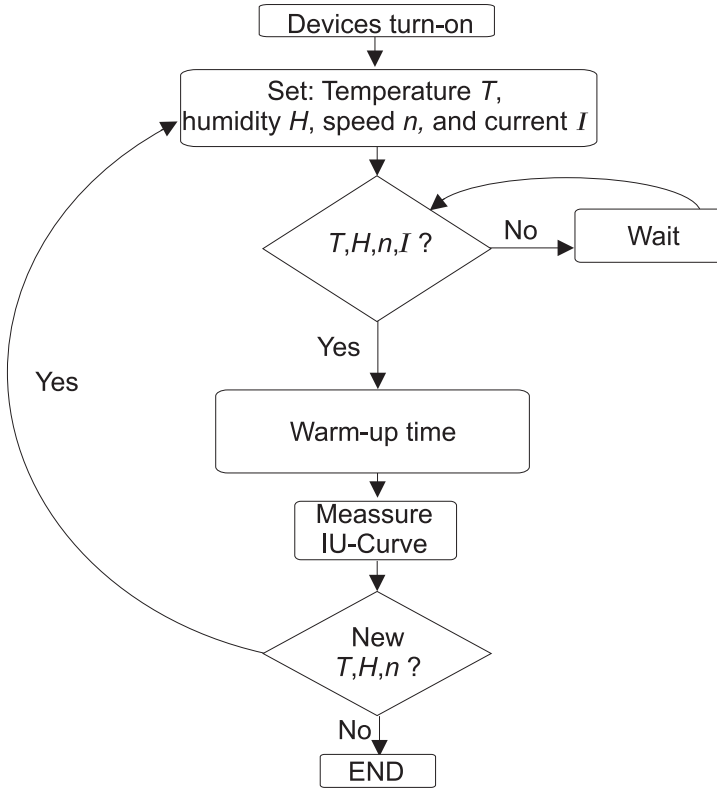

Fig. 4.8: Flow chart of the test.

And in the following sections the results will be present as UI-curves. The values present in those curves are

$$\overline{U(I)} \pm \Lambda(I) \tag{4.8}$$

4.3.4 Test Program

After all these tests and definitions, the standard test has to be established. Fig. 4.8 describes the different steps of the test. So, the test begins with the switch on of all the devices. This step cannot be done automatically by remote control. After switching on, the Labview program sends the configurations to the oscilloscope, motor and DAS. During this initialisation process, the Labview program reminds the user with some messages to the different tasks, which can only been made by hand. Then, the temperature

and humidity values are sent to the climate chamber, the speed to the motor and the current to the DAS unit. The controlling program starts monitoring the current and environmental parameters. The Labview program waits till the desired environmental situation is accomplished and stable. In this point, there is the possibility of a non-reachable environmental situation, because the parameters are on the boundary of the working range of the climate chamber . So, the Labview program monitors the chamber tendencies (temperature and humidity). With this monitoring task, the program determines, if there is not a reachable environmental situation. The name of this situation is "parameters limit" in the figure, because the climate situation is on the limit of the working range. When the Labview program determines the parameters limit situation, it continues with the test in the climate chamber limit. In addition, the program stores the environmental situation, in order to have all the information in the analysing result part.
The Labview program orders a constant current, and waits the warm-up time. During this time, the Labview program continues monitoring the environmental situation. Thus, the test run for 2 hours with a constant current, speed, humidity, temperature, and the controlling task. After this time, an UI-curve is measured. In order to determine an statistical error of the voltage, four current ramps are made. All the measured values are stored in an ASCII file. After that, a new test can be started with new parameters. Furthermore, the number of tests will be great, and the number of files with only one parameter variation with another also will be big. Thus, it is useful to automatise the excel file generation, and the extraction of the test parameters from the header. Thus, different macros were carried out in order to take care of each analyse point.
Finally, a defined test has been developed, combining different programs and concepts. There are different test stages, but in general, there is an automatised test capable to manage a big amount of information.

4.4 Measurements

The different measurements will be presented, beginning with a complete example. In this example, the transformation of the four frames to the UI-curves will be done. Then, the systematic measurements will be shown. The explanation of the different parameter dependencies are given. Then, a tendency analysis is done in order to synthesise the data volume and to be sure of the different parameter influences. In addition, this tendency analysis is clarified in detail through an example. Finally, a short presentation of the tendency analysis results will be given.

4.4.1 Measurement Example

One of the standard measurements will be explained in this section as measurement example. Fig. 4.9 shows the measured curves from the oscilloscope. The test program orders four current ramps as we have already seen. The output voltage between the two brushes is measured, as the mean voltage between the channels four and three of the oscilloscope. The standard deviation of the channel difference also is measured in order to have the signal error. The first ramp is a little bit different in comparison with the others. This difference occurs sometimes, the macro detects this difference and makes the calculations without the first ramp. Another advantage of our automatised test bench is that we can measure with a constant sampling rate. The time between two points is about 5 seconds, because this is the time that the oscilloscope needs to calculate the mean value. Thus, one ramp is obtained in 105 seconds, and the entire wave in 425 seconds, and the voltage values are the mean values calculated by the oscilloscope. With this UI-curve time, the oxide layer has not time to adapt itself to the different current values.

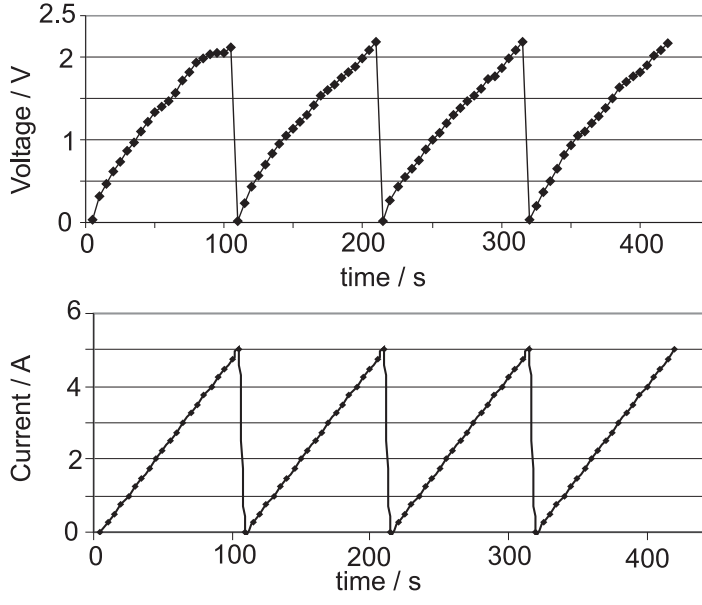

Fig. 4.9: Measured curves in time domain. Curves obtained for $n = 1500\,\text{rpm}$, $H = 60\,\%$ and $T = 50\,^{\circ}\text{C}$.

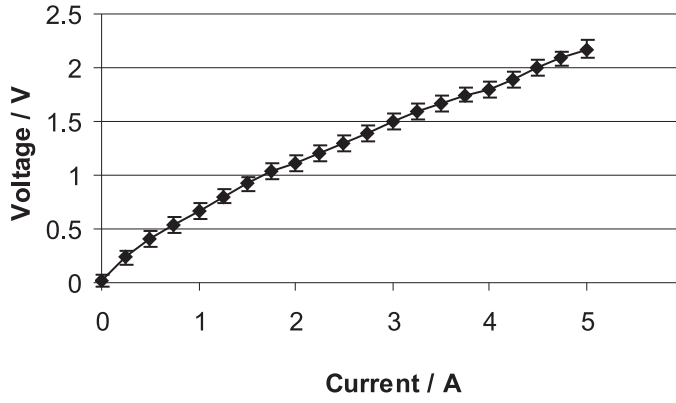

Fig. 4.10: Final UI-curve obtained from three ramps. Curve obtained for $n = 1500\,\text{rpm}$, $H = 60\,\%$ and $T = 50\,^{\circ}\text{C}$.

Thus, the oxide layer is not representative of each current value of the ramp. However, the oxide layer is characteristic of the environmental situation with a current $I_{max}/2$. Because of the big signal unevenness, the mean voltage value represents the voltage drop. The current values were more stable than the voltage values.
The macros transform these four ramps in one composed by the mean values of the ramps. The error also is calculated by the macros as presented in section 4.3.3. Finally, the UI-curve is shown in Fig. 4.10. The curve is obtained for a temperature of 50 °C, an angular speed of 1500 rpm and a humidity of 60 %. The voltage drop is between the two brushes, going from zero to 2.2 V. Focusing on the current values, there is a point each 0.25 A. The error bars are about 200 mV high in all the voltage range. Their influence is big enough to be taken into account. The UI-curve shows a typical behaviour which can be found on every measurement. In the next subsections, we are going to study the parameter variation influence.

4.4.2 Systematic Measurements

After determining the characteristics of the test experiment, we made a series of tests. In this section, the results will be presented. In the following presentation, the parameter names will be changed in order to have a shorter legend. The names are the following

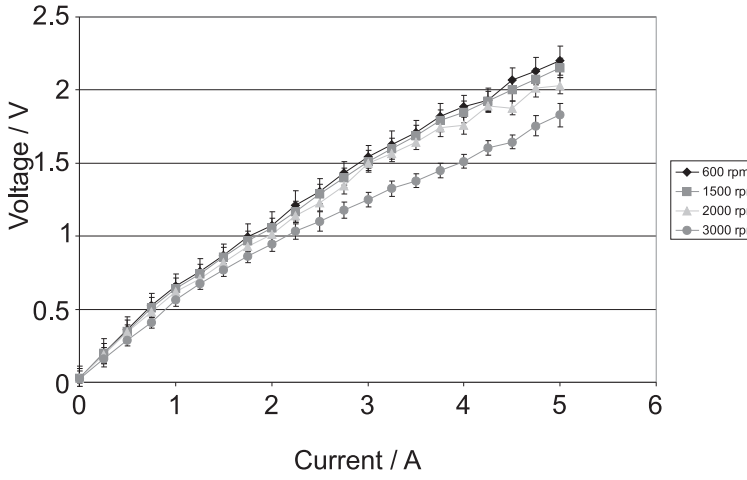

Fig. 4.11: Measurements with T=50°C and H=50 %.

- Temperature → T
- Relative humidity → H
- Angular speed → n.

The measurements comprised a big range of different conditions. The parameters variation is:

T = 10, 20, ... 90°C (9 values)

H = 10, 20, ... 90 % (9 values)

n = 600, 1500, 2000, 3000 rpm . (4 values)

Thus, the total number of measurements are $9 \cdot 9 \cdot 4 = 324$. Some of them could not be taken into account in the analysis phase because of the working range of the climate chamber. The electric test bench influences the chamber room. Thus, the climate chamber has not an exact working range. However, the monitoring property of our program allows us to see when the environmental situation was not stable.
The next examples show the influence of the variation of T,H, and n respectively to the standard situation of T=50°C, H=50 %, and n=3000 rpm.
Fig. 4.11 shows the curves measured with a constant temperature T of 50 °C and a constant relative humidity H of 50 %. The figure shows the UI-curve with the angular speed as parameter. As the angular speed grows,

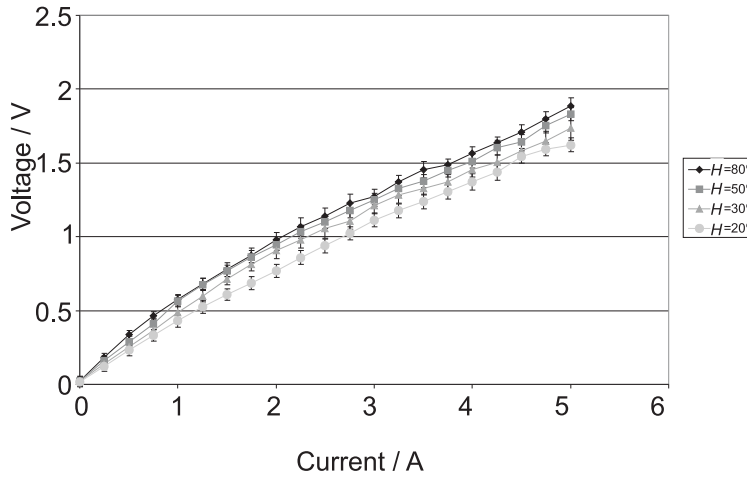

Fig. 4.12: Measurements with T=50°C and n=3000 rpm.

the voltage drop decreases. This effect could be measured in all the other examples. The increase in the speed entails a bigger clearing effect. This results in a thinner oxide layer, a higher electric field, and a bigger number of spots. Also, the oxide resistance decreases as the oxide thickness decreases. Both effects, the bigger number of spots and the smaller oxide resistance, cause a decrease in the contact resistance. There is not a linear decrease, the curve with 3000 rpm has a bigger decrease regarding the curve with 600 rpm than the other curves (1500 and 2000 rpm). This effect is related to the non linearity in the motor vibration with the angular speed. The highest motor noise was observed at an angular speed of 3000 rpm, but its increase with the speed also was not linear.

Fig. 4.12 shows the dependence of the UI-curve with the variation of the relative humidity. All the curves are measurements with angular speed of 3000 rpm and a temperature of 50 ℃. The voltage drop increases as the relative humidity increases. The oxidation increases with growing relative humidity [34, 71]. This produces a thicker oxide layer, a smaller electric field, and a smaller number of spots. This smaller number of spots is equivalent to a bigger resistance value in electric terms. Also, the thicker oxide layer has a bigger channel resistance. The sum of these two effects causes this voltage drop to increase.

Fig. 4.13 shows the UI-curves with the temperature as parameter. All the curves are measured with an angular speed of 3000 rpm and a relative hu-

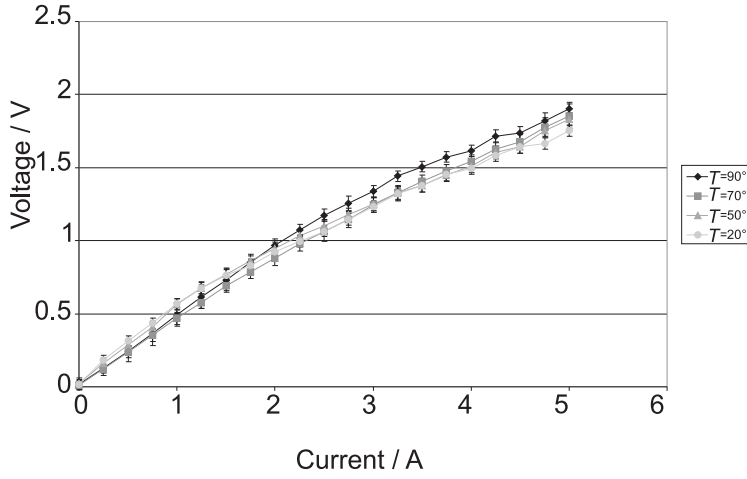

Fig. 4.13: Measurements with n=3000 rpm and H=50 %.

midity of 50 %. There is a growth in the voltage drop when there is an increase in the ambient temperature. The oxidation increases with increasing the temperature. Thus, the effect is similar of the effect of the relative humidity.
A parameter classification can now be done taking into account the variation range of Fig. 4.11, Fig. 4.12 and Fig. 4.13. The biggest variation range is for the angular speed, and the smallest variation range is for the ambient temperature. Thus, the voltage drop is influenced by the angular speed, relative humidity and ambient temperature in this order of importance. This comparison is always inside the variation range of each parameter, perhaps in other variation range appears other classification.
All in one, a decrease in the angular speed generates a bigger voltage. An increase in the relative humidity produces a bigger voltage. An increase in the ambient temperature generates a bigger voltage. The influence of the different parameters has the order: angular speed, relative humidity, and temperature.

4.4.2.1 Tendency Analysis

The volume of measured UI-curves is huge, and we have to be sure that the tendencies are well defined. A tendency analysis was performed in order to clarify the tendencies, but not to model the system. Thus, the analysis is a qualitative tool to guarantee the tendencies.

T °C	U_{max} V	Error V	$G_0 + G_n \cdot n + G_H \cdot H$ V	G_T V / °C
10	–[a]	–		
20	1.55	0.03		
30	1.70	0.04		
40	1.72	0.05		
50	1.62	0.06	1.56	2.85e-3
60	1.66	0.04		
70	1.74	0.04		
80	1.80	0.04		
90	1.81	0.04		

Table 4.4: Example of tendency analysis for n=3000 rpm and H=20 %.

[a]Border range for the climate chamber

A new representation to all the data is done in order to perform better analyses for the full data volume. For example, if the effect of the relative humidity is amplified by the effect of an increasing temperature, the analysis can detect this dependency. This type of second dependencies defines the grade of complexity of the model.
The proposed analysis was done in an individual current value in order to check its variation with the different parameters. Thus, we made a tendency analysis, with the voltage of the UI-curves, at the maximum current of 5 A. This voltage is analysed for two constant parameters and varying the third. Table 4.4 shows an example for constant relative humidity and angular speed. A linear regression is done over the variation of the voltage drop vs. temperature. The linear regression is in accordance with

$$U_{max} = G_0 + G_T \cdot T + G_n \cdot n + G_H \cdot H \quad , \tag{4.9}$$

where G_0 represents the independent term, G_T parameter means the influence of the ambient temperature, G_H represents the influence of the relative humidity, and G_n represents the influence of the angular speed. For example in Fig. 4.14, $G_0 + G_n \cdot n$ is the independent term G_H represents the function of the relative humidity and G_T represents the effect of the ambient temperature.
Fig. 4.14 shows different tendency curves for different relative humidity values and for a constant angular speed (n = 600 rpm). The x-axis is the ambient temperature and the y-axis is the voltage drop at maximal current value of 5 A. The highest tendency line corresponds to the biggest relative

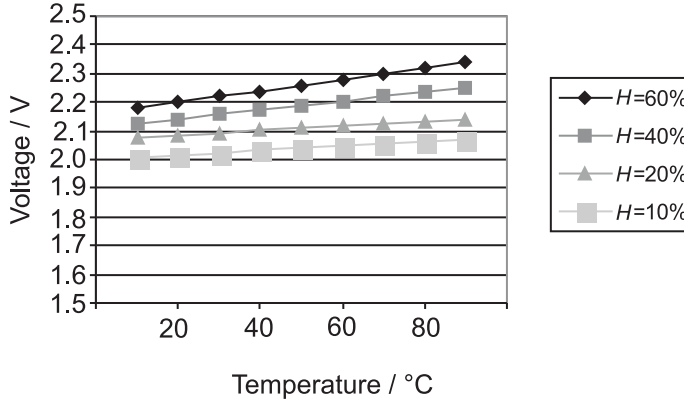

Fig. 4.14: Tendency lines for constant n= 600 rpm and H as parameter.

humidity value. The lowest tendency line matches with the smallest relative humidity value. Furthermore in a constant temperature, the voltage drop order corresponds to the relative humidity order. This is because the G_H parameter is a positive value. Thus, a growing relative humidity produces a succession of bigger voltage drops. The G_T indexes of all the tendency lines are positive, indicating an increase of the voltage drop with a growing ambient temperature.

All in one, an increasing temperature causes a growing voltage drop. Moreover, a rising relative humidity produces a growing voltage drop. However, an influence between both parameters does not appear.

Fig. 4.15 shows another type of tendency analysis. The y-axis is the voltage drop and the x-axis is the ambient temperature. In this case, the relative humidity remains constant ($H = 50\,\%$), and the angular speed is the parameter with a range from 600 rpm to 3000 rpm. Thus, the independent term is $G_0 + G_H \cdot H$. The highest tendency line agrees with the smallest angular speed. Thus, the highest voltage drop corresponds to the slowest angular speed. Moreover, in a constant temperature, the increasing voltage drop order corresponds to the decreasing angular speed order. In this representation, the G_n tendency parameter is negative. An increasing temperature produces a rising voltage drop for measurements with constant relative humidity and angular speed. G_T is always a positive value, indicating the influence of the temperature. G_T cannot be described as a simple function

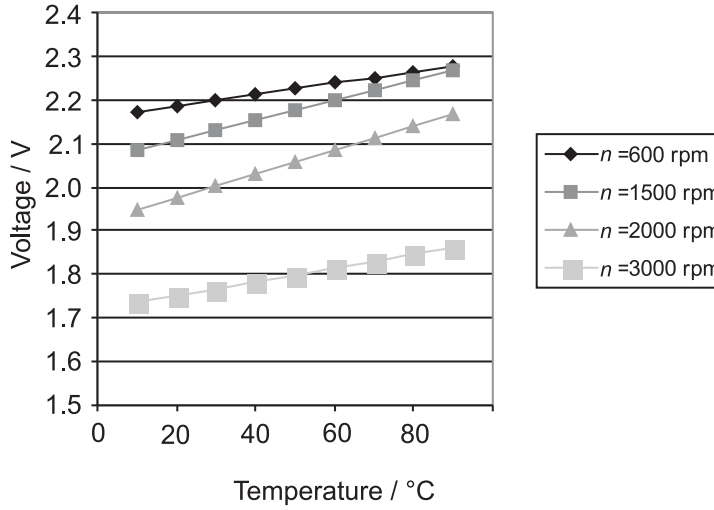

Fig. 4.15: Tendency lines for constant H=50 % and n as parameter.

of the angular speed. This can be caused because the temperature influence is the smaller one, as it was concluded from the analysis of UI-curves. The temperature influence is so small, that it is in the limit of our test bench, and no dependencies between temperature and the other parameters occur.

All in one, Fig. 4.15 points out two parameter influences: an increasing temperature produces a rising voltage drop, and a reduced angular speed causes a rising voltage. The angular speed influence is bigger than the temperature influence, as the succession of values remains only in the angular speed case. Fig. 4.16 shows the influences of angular speed and humidity. The y-axis is the voltage drop and the x-axis is the relative humidity. In this case, the temperature remains constant (T = 50 °C), and the angular speed is the parameter with a range from 600 rpm to 3000 rpm. The angular speed influence is similar to the one in Fig. 4.15. In this representation, the G_n tendency parameter is another time negative. G_H values are practically equal, as it is indicated by the parallel tendency lines in the figure. G_H is always a positive value, indicating the influence of the relative humidity. An increasing relative humidity produces a rising voltage drop for measurements with constant temperature and angular speed.

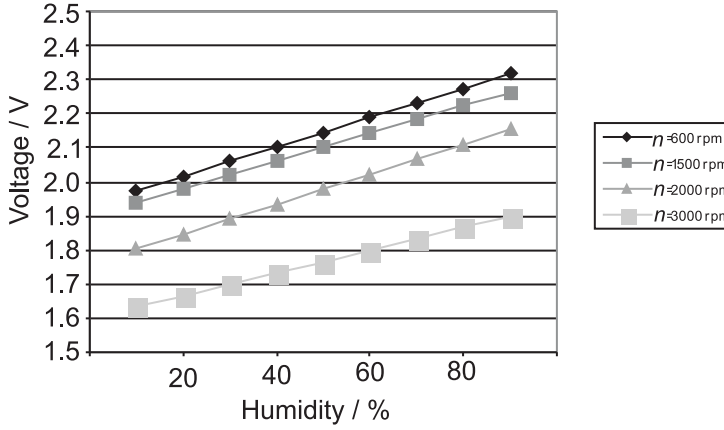

Fig. 4.16: Tendency lines for constant T=50°C and n as parameter.

All in one, Fig. 4.16 points out two parameter influences: an increasing relative humidity produces a rising voltage drop, and in contrast a reducing angular speed causes a rising voltage.
Taking into account the UI-curves and the tendency representations, the parameter tendencies in all the curves were:

- increasing voltage with reducing angular speed
  (Fig. 4.11, Fig. 4.15 and Fig. 4.16)
- increasing voltage with growing relative humidity
  (Fig. 4.12, Fig. 4.14 and Fig. 4.16)
- increasing voltage with growing temperature
  (Fig. 4.13, Fig. 4.14 and Fig. 4.15)

Chapter 5

Model

5.1 Introduction

The final step of the project is the modelling of the contact. In this chapter, the different aspects of the model are explained. Firstly, an equivalent circuit is introduced, explaining each device and its represented effect. Furthermore, the influences taken into account are the oxide thickness, the capacitance between conductors, the temperature increase on the sliding surfaces and the spot radius. Each model device has a corresponding equation, being listed and explained. Additional effects are considered in the model as an temperature increment on the rotor, variable specific resistivity of copper, the spot growth and the oxide thickness equation. Thus, each equation used in the model is presented.
In the equations, there are parameters whose value range is known from the bibliography, for example a is about 3-50µm. In addition, other parameters are used in order to calculate known parameters, for example, the oxide thickness parameters are used to calculate the oxide thickness. In order to adapt the model to the measurements, a hierarchical optimisation was implemented. The variation of the model parameters was always inside the known ranges, or in order to become known magnitude range.
The optimisation task is explained, paying attention to its different phases. Different parameter types are introduced in order to perform the different optimisation phases. There is a first group of parameters that has been used to adapt the model to the general contact voltage drop. These parameters are optimised on the first optimisation phase, remaining constant after this first optimisation. Afterwards, individual modelling parameters are optimised in order to describe the parameter variation range. Then, the final optimised

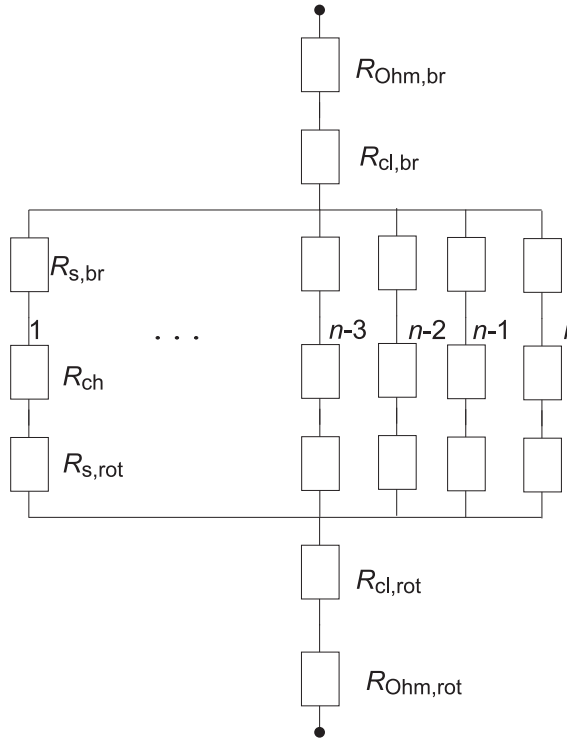

Fig. 5.1: Resistance circuit of the model.

parameter values are given.
The optimisation results are given as UI-curves, depicting always the measured values with the model curves. Firstly, the first optimised curve is shown, clarifying the optimised parameters. After this first optimisation, the tendency optimisation is developed. The three observed tendencies are modelled and the different tendency parameters are optimised in order to describe the varying ranges. Three different UI-curves are presented to show the tendencies optimisation. Finally, the presented range is clarified and discussed.

5.2 Implemented Circuit

The implemented model is realised using an electric circuit. Thus, the equations for the constriction resistance could be used and an easy conceptual

model is carried out. Moreover, we can have the real electric relation between the different parameters related in the contact.
Fig. 5.1 shows the implemented circuit, which includes all the implemented resistances of the circuit. The upper part of the figure corresponds to the brush, and the bottom part is the rotor. The oxide layer is located exactly in the middle of the circuit but it is not present in the electric circuit itself. The electric conduction happens through the channels, so these channels are the bridges between the brush and the rotor.
The top circuit resistance is the ohmic resistance of the brush ($R_{\mathrm{Ohm,br}}$). This ohmic resistance is present on the contact, going from the upper surface till the constriction zone. Below the ohmic resistance part, the constriction resistance starts, but start with the group effect of the spots. Thus, the cluster resistance ($R_{\mathrm{cl,br}}$) is located below the ohmic resistance.
Following the cluster resistance, the individual spot effect becomes the most powerful. Thus, the spreading resistance ($R_{\mathrm{s,br}}$) is placed below the cluster resistance. This spreading resistance belongs to each spot, so the resistance is continued as a parallel connection of resistances. Following the spreading resistance, the channel resistance (R_{ch}) is the next resistance in the circuit as it happens in the real geometry. This channel resistance also belongs to each spot, going on with the parallel circuit. The channel parallel resistances form the horizontal symmetry-axis of the circuit. The resistances up and down from the channel resistances are equivalent, depending only on the composing material. Following the channel resistance, the material changes to the copper of the rotor. The upper resistance on the rotor agrees with the spreading resistance ($R_{\mathrm{s,rot}}$), as the conduction happens through the spots. These spreading resistances are also placed in the parallel circuit. Thus, each parallel circuit branch is the serial connection of the two spreading resistances and the channel resistance.
Fig. 5.1 shows the parallel connection of n branches. The group of branches from the first to the n-1 are spots with a constant spot radius. The n'th spot is the last created spot, having a variable radius. Thus, this spot is the growing spot, suffering from b-fritting.
Below the spreading resistances on the rotor side, the group effect of all these rotor spots influences the total conduction. Thus, the cluster resistance ($R_{\mathrm{cl,rot}}$) in the rotor is located below the spreading resistances. This cluster resistance joins the parallel branches, and the circuit is continued as an individual branch. The parallel circuit is located between the two group effects, or it is located where the individual effects of each spot are the dominating resistance effect. Below the cluster copper resistance, the ohmic copper resistance is located ($R_{\mathrm{Ohm,rot}}$).
To summarise, the model starts and finishes with ohmic resistances. In the

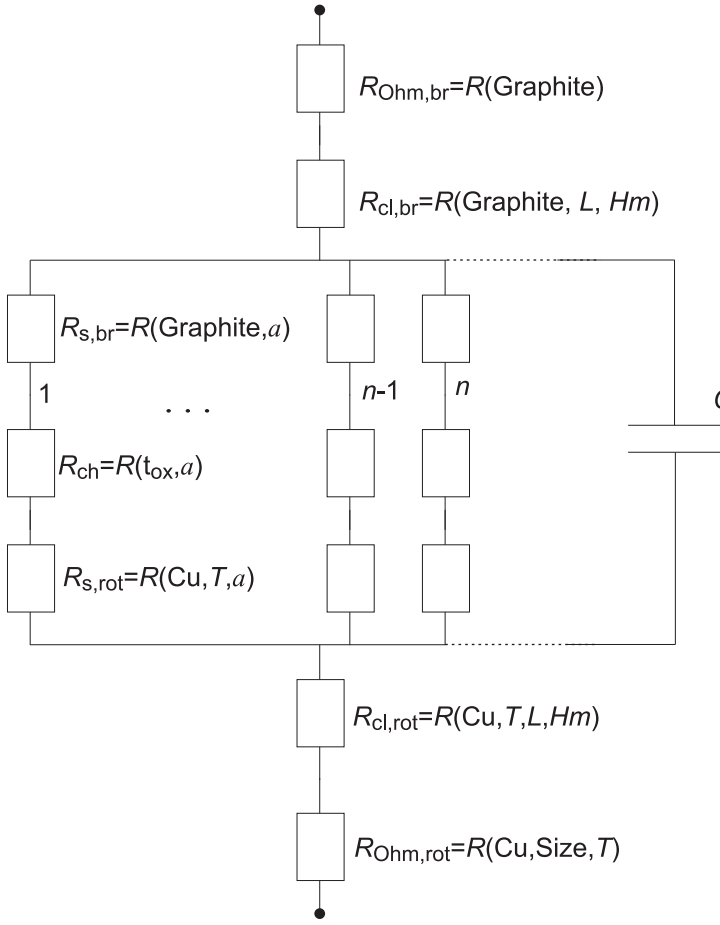

Fig. 5.2: Resistance circuit of the model.

middle part of the circuit, constriction and cluster resistances are present to describe the effects located in the contact surface.
The ohmic resistances located in the rotor and the brushes have to be determined. The geometrical size of the ohmic resistances is determined through the FEM simulations. This was already studied in chapter 3. Fig. 3.5 shows a scheme of the potential lines in a contact composed by one spot. The constriction zone starts when the potential lines could be described as ellipses around the spots. Before this constriction zone, the potential lines are straight lines following the Ohm's law. The potential lines are ellipses

when the current density has a huge x-component. In section 3.3.3, current density integrals were done over horizontal surfaces. The integrations increase their error when the current density has a big horizontal component, giving a bad current value. The FEM integrations are working till a distance $200 \cdot a$ from the spot. With $a = 5\,\mu m$, this distance becomes 1 mm. Thus, the considered ohmic part of the brush will be from the brush top to 1 mm from the brush surface. On the rotor, the ohmic part also is assumed from the bottom surface to 1 mm from the upper rotor surface.

5.2.1 Circuit Influences

The circuit devices are already explained from the point of view of summarising all the used devices. Each device takes into account different influences as rotor temperature increase, or spot radius. In this section, all these influences are explained referring always to the respective device.
Additionally, the circuit capacitance is discussed. The presence of an oxide causes the existence of a capacitance between brush and conducting rotor. This capacitance will be discussed from the simulation and empirical experiences.

5.2.1.1 Circuit Resistances

Fig. 5.2 shows the different resistance dependencies. The explanation will go from top to bottom as the description of Fig. 5.1. The upper resistance part of the figure depends on the type of brush used, or in other words depends on the type of graphite compound. These graphite resistances can be described with a linear negative decrease in their specific resistivity. However, as a significant dependency on specific resistivity was not found, no temperature dependence was implemented. The ohmic brush resistance depends on the sizes of the brush (width and height) and the brush material. The cluster brush resistance also depends on the load pressing the contact and the type of brush material. The spreading brush resistance depends on the size of the spot and the brush material. At this point we leave the brush zone and go inside the oxide zone. The channel resistance depends on the oxide thickness and on the spot radius. The rotor spreading resistance depends on the temperature of the sliding surface, the rotor material and the spot radius. The cluster rotor resistance depends on the temperature on the surface, the load pressing the contact and the rotor material. The ohmic rotor resistance depends on the temperature of the surface, the rotor material, and the size of the rotor.

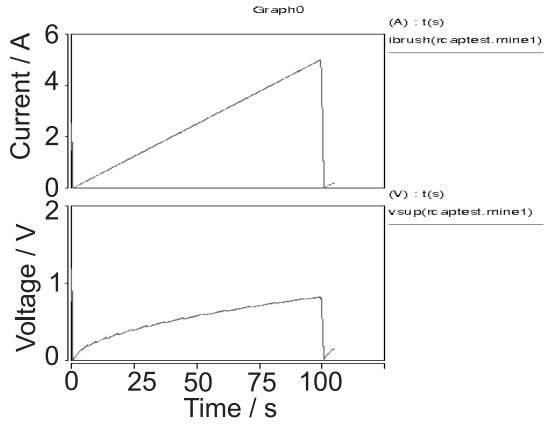

Fig. 5.3: UI-curves for a parametric simulation with an oxide capacitor between 1 pF and 1 µF.

5.2.1.2 Circuit Capacitor

Between the brush and conducting rotor, there is an oxide layer breaking the electric conductivity. In the presence of electric current, channels are formed, within these channels the electric conductance is given. However, this oxide layer causes the existence of a capacitance in the electric circuit. Fig. 5.2 shows the capacitor connected to the rest of the circuit with a non-continuous line. There is no capacitor present in our model, but its possible inclusion was studied. First, a verification was performed to calculate its value, using the geometrical and material characteristics. The capacitor is in the pF range, so it is a tiny value in order to have influence in our measurements. Second, a new constriction model was implemented with a capacitor inside the resistance model. Fig. 5.3 shows a parametric simulation of a model with an oxide capacitor. The ramp time is the same as in our measurements, and the capacitance value is varied from 1 pF to 1 µF. Thus, there is no influence of the capacitance with our test implementation.
Another verification was the empirical observation, that the capacitance effect is not present in our measurement and previous experimental observations. For these reasons, the capacitor was not implemented in the model.

5.3 Implemented Equations

In this section the equations used in the model are listed. The different model equations are classified in two types: the circuit equations and the internal equations. The circuit equations are the resistance formulas from Fig. 5.1 and Fig. 5.2. The internal equations are the remaining equations need to describe the specific effects of a sliding contact.

5.3.1 Circuit Equations

According to Fig. 5.1, the model is a symmetrical. The symmetrical axis is given by the channel resistances. For example, the resistances of the top and bottom are equal with the exception of their specific resistivities. The equation explanation will start as in the previous descriptions (the upper zone), and will progress to the central axis. The resistances of the extremes are the Ohmic resistances. Their equation form is

$$R_{\mathrm{Ohm}} = \frac{\rho \cdot l}{A} \quad , \tag{5.1}$$

where A is the horizontal area, l is the vertical length and ρ is the specific resistivity [51]. All these constants are given by the respective material and the geometry. The length is always the ohmic part of the conductor, in other words far away from the spots. The distance between the spots and the ohmic part was about 1 mm in order to be compatible with the FEM simulations. The next resistance is the cluster resistance or in other words the group effect of the spots. From Eq. 2.19, and Eq. 2.27, and accepting that the cluster radius is equal to

$$\pi \cdot \xi^2 = A_c \quad , \tag{5.2}$$

the cluster resistance is

$$R_{\mathrm{cl}} \; = \; \frac{\rho}{2}\sqrt{\frac{H_m \cdot \pi}{\Upsilon \cdot L}} \quad , \tag{5.3}$$

where ρ is the specific resistivity, H_m is the hardness of the softer contact material, Υ is an empirical parameter equal to 0.1, and L is the load pressing the brush [31, 30, 34, 55, 56, 15, 41].
Afterwards, the remaining circuit is the parallel connection of spot resistances. The spreading resistance in one conductor is

$$R_s = \frac{\rho \cdot f(\gamma)}{4 \cdot a} \quad , \tag{5.4}$$

where the ρ is the specific resistivity of the respective material, a is the spot radius and $f(\gamma)$ is the ellipticity factor [34, 71, 55, 56, 15, 57, 18, 41]. Finally, the remaining circuit resistance is the channel resistance calculated following:

$$R_{\mathrm{ch}} = \frac{\rho_{\mathrm{ch}} \cdot t_{ox}}{\pi \cdot a^2} \quad , \tag{5.5}$$

where ρ_{ch} is the channel specific resistivity, and t_{ox} is the oxide thickness [34, 71, 37, 57, 18, 51, 41]. With these two last equations, we can describe the parallel circuit.

5.3.2 Internal Equations

Up to now the electric circuit has been clarified, going through each individual resistance. However, other equations are used to obtain a proper contact description. The next points will deal with some influences and cases implemented in the model.

5.3.2.1 Temperature Increment

The system is a sliding electric contact with a working angular speed and electric current. Thus, the temperature on the rotor is different from the one in the chamber [34, 71, 62]. The friction and current causes an increase in the temperature. The implemented local temperature of the rotor is

$$\Delta T = \frac{\left(\mu \cdot L \cdot \sqrt{v} + \frac{\overline{I}^2 \cdot R}{\sqrt{v}}\right)}{3.6 \cdot \sqrt{\varrho \cdot c_p \cdot r_{\mathrm{rotor}}^3 \cdot k_{\mathrm{rot}}}} \quad , \tag{5.6}$$

where r_{rotor} is the radius of the rotor, μ is the friction coefficient, L is the normal load, v is the linear speed ($v = 2 \cdot \pi \cdot r_{\mathrm{rotor}} \cdot n$), c_p is the specific heat, ϱ is the material density, k_{rot} is the thermal conductivity of the rotor, $\overline{I}$ is the mean current and R is the mean resistance [62]. With this equation we can calculate the temperature on the rotor surface, and use this increment to calculate the material specific resistivity variation.

5.3.2.2 Specific Resistivity of Copper

For the temperature dependence of the specific resistivity of copper different formulas were found. The most exact formula was given by White & Minges

[81]. They give the specific resistivity as a polynomial as follows

$$\begin{aligned}
\frac{\rho_{\text{copper}}}{\Omega\,\text{m}} &= 1\cdot 10^{-8}\cdot\sum_{j=0}^{5} A_j \left(\frac{T}{1000\cdot\text{K}}\right)^j \qquad (5.7)\\
A_0 &= -3.843\cdot 10^{-1}\\
A_1 &= +7.5319\\
A_2 &= -2.6988\\
A_3 &= +3.9604\\
A_4 &= -2.1106\\
A_5 &= +5.579\cdot 10^{-1}
\end{aligned}$$

where T is the temperature in Kelvin. This expression is valid for a range between 100 and 1000 K. Thus, we can use now a correct specific resistivity of copper and use this variation in our model.

5.3.2.3 Growing Spot

There are two different spot types, the mature spot and the growing one. The mature spots have a constant spot radius that is a function of the materials hardness and the contact load. The growing spot is the last formed spot and it is in a growing phase. It can be affirmed that a spot has a constant current density [34, 30]. The current density in a circular spot is

$$\| \overrightarrow{J_{\text{spot}}} \| = \frac{I_{\text{spot}}}{\pi\cdot r^2} \quad , \qquad (5.8)$$

where r is the growing spot radius, and I_{spot} is the spot current. The growing radius becomes

$$r = \sqrt{\frac{I_{\text{spot}}}{\pi\cdot \| \overrightarrow{J_{\text{spot}}} \|}} \quad . \qquad (5.9)$$

With an increment of I_{spot}, the spot radius will increase. This equation will be implemented in the model, applied to the last formed spot as the constriction theory rules.
The creation of a new spot is calculated through the electric field. This electric field is located inside the oxide layer, so the oxide thickness is used to calculate the electric field as follows

$$\| \overrightarrow{E} \| = \frac{V_{\text{surf}}}{t_{ox}} \quad > \quad \| \overrightarrow{E}_{\text{fritting}} \| = 10^8\ V/m \quad , \qquad (5.10)$$

where V_{surf} is the voltage on the oxide surface, and t_{ox} is the oxide thickness. The voltage on the oxide surface is calculated from the voltage drop in the spots and cluster. When the electric field is bigger than the fritting electric field a new spot comes. The bibliography gives different values for the fritting electric field value, but 10^8 V/m is the most used.

5.3.2.4 Oxide Thickness

The oxide thickness is an important parameter in the contact resistance. Most of the environmental parameters develop their effects in the oxide layer covering the rotor, changing its thickness, composition or structure. There are some bibliographic references, where values for the thickness are given [38, 71, 26, 2, 1], and in [71] an oxide growing equation is presented:

$$t_{ox} = (K(H) \cdot t)^{1/\Gamma} \quad , \tag{5.11}$$

where Γ is a constant between 1 and 3, $K(H)$ is a factor depending on the relative humidity, and t is the formation time. A growing relative humidity increases the value of $K(H)$. Thus, a growing relative humidity produces an acceleration in the oxide formation.
There were no bibliographic resources about growth equations taking into account temperature influences or moving systems. The equation implemented is developed to obtain the bibliographic oxide thickness values, but it is totally new, because nobody has determined the growth of oxide layers in a moving rotor with a controlled atmosphere.
The oxide thickness is a function of the relative humidity. This dependency is on the function $K(H)$ as

$$t_{ox} \sim (K(H))^{1/\Gamma} \quad . \tag{5.12}$$

The model has three parameters H,T,n. The dependency with the other parameters (T,n) was implemented with the form of the dependency on the humidity.
The angular speed has two differences in comparison with the others: an increase in the speed produces a decrease in the voltage drop, and it exists a non-linearity. Thus, in the t_{ox} a function F is introduced to describe the angular speed effect. Fig. 4.15 and Fig. 4.16 show this non-linearity. The F tendency parameter is obtained performing a regression of the U_{max} with T,n constant. The regression is

$$\frac{U_{\max}}{\text{V}} = \cdot \left(-8 \cdot 10^{-8} \cdot \left(\frac{n}{\text{Hz}} \right)^2 + 6 \cdot 10^{-5} \cdot \left(\frac{n}{\text{Hz}} \right) + 2.2449 \right) \quad , \tag{5.13}$$

where n is the angular speed. Thus, the F function becomes

$$\frac{F}{\text{Hz}} = \cdot \frac{(-8 \cdot 10^{-8} \cdot \left(\frac{n}{\text{Hz}}\right)^2 + 6 \cdot 10^{-5} \cdot \left(\frac{n}{\text{Hz}}\right) + 2.2449)}{2} \quad , \tag{5.14}$$

where the 2 factor comes from the transformation from the two contact resistances measured and the individual contact resistance optimised.
Finally, the oxide thickness equation has the parameter dependence from Eq. 5.12, and in this work it is proposed a self equation. The self equation is

$$t_{ox} = 1e^{-9} \cdot C_{\text{glob}} \cdot (C_H \cdot H)^{1/P_H} \cdot (C_n \cdot F)^{1/P_n} \cdot (C_T \cdot T)^{1/P_T} \quad , \tag{5.15}$$

where H is the humidity, n is the angular speed, and T is the temperature. There are two kinds of parameters: the coefficient parameters and the exponential parameters. The variables starting with C are constant coefficient, and the ones starting with P are the exponential coefficients. The C_{glob} is a global coefficient parameter, independent of the humidity, angular speed and temperature. C_H , C_n, and C_T are the coefficients describing the dependencies of the t_{ox} on the humidity, angular speed and ambient temperature respectively. P_H, P_n and P_T are the exponential parameters describing the dependence of the t_{ox} on the humidity, angular speed and ambient temperature respectively. Thus, there are two kinds of parameters in term of dependencies: the ones depending on each variable (C_H and P_H depending on the relative humidity, C_n and P_n depending on the angular speed, C_T and P_T depending on the ambient temperature), and the ones that are one global parameter (C_{glob} depending on the general model adaptation). Other equations were tried but this one was the best one for the optimisation. In the next sections all these oxide thickness parameters will be calculated and optimised.

5.4 Standard Model Parameters

The model is based on theoretical and empirical parameters. Inside the theoretical parameters some of them are not observable in a standard situation. The referred parameters are for example the spot radius, ellipticity, and others. The test device is a commercial model, so all these parameters are non-observable parameters. Most of them depend on the materials, load, geometry sizes, and others. All these non-observable parameters depend on the experiment characteristics. These parameters are studied in the bibliographic sources, resulting a possible variation range of them. In the optimisation, these parameters will be varied inside the bibliographic ranges.

There are other parameters that are not studied until this research. The referred parameters are the ones coming from the oxide thickness equation. Nobody has studied the brush-rotor contact with the environmental situation as parameter. The experiences already done with a controlled environment, were focused on studying different gases and pressures. The parameters used in this investigation are not present in the existing bibliography. In the optimisation, these parameters will be varied in a range which obtains reasonable physical solutions.
The software used to optimise the parameters is the WEVA-tool (*Werkzeug zur Erstellung von Verhaltensmodellen komplexer Analogsysteme*). WEVA-tool is an optimisation tool that can optimise a model with a given set of parameters. The WEVA-tool needs to know the optimal values in order to know which is the target of the optimisation. In our case, the optimal values are the measurements, as the model has to predict the contact voltage drop. The WEVA-tool simulates the model with the initial set of parameters. The user gives this set of parameters. Therefore, it calculates the error of the simulation with the measurements. Then, it varies the set of parameters, and performs a new simulation. Therefore, it calculates the error of this second simulation. At this point, WEVA-tool compares the two errors in order to know which simulation is better. Thus, WEVA-tool calculates another parameter variation trying to improve the simulation results. It performs a new simulation within this last varied parameters. Then, it compares the error of this last simulation with the error of the best one. WEVA-tool selects the best simulation and returns to calculate a possible parameter set. That is repeated until no change in the errors are originated. The optimisation of the model has a big set of involved parameters. Thus, it was divided in steps. Each optimisation step is in charge of a group of variables leaving the other parameters constant. Due to this hierarchical

Type	**Parameter**	**Symbol**	**Range**
Global	Spot radius	a	5-30 µm
	Ellipticity	γ	3-6
	Global coefficient of the t_{ox}	C_{glob}	–
Individual	Humidity coefficient	C_H	–
	Humidity exponential coefficient	P_H	–
	Angular speed coefficient	C_n	–
	Angular speed exponential coefficient	P_n	–
	Temperature coefficient	C_T	–
	Temperature exponential coefficient	P_T	–

Table 5.1: Global and individual modelling parameters.

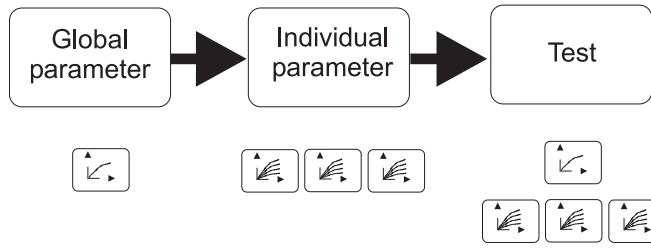

Fig. 5.4: Optimisation Process.

scheme, a classification of the different parameters was done. Thus, the target model will have two types of parameters:

1. global modelling parameters, and
2. individual modelling parameters.

Table 5.1 shows the parameter classification with the respective variation ranges. The global modelling parameters are optimised in order to adapt the model to a selected UI-curve. The selected UI-curve is located in the middle test range in order to avoid a big effect of one parameter. This global optimisation phase regards the first model optimisation. These parameters are a, γ and C_{glob}. a and γ are geometrical parameters, having a bibliographic variation range. C_{glob} is a parameter that adapts the oxide thickness to the bibliographic values. The C_{glob} is a parameter inside the t_{ox} equation, being dependent of the initial value of the individual modelling parameters.
The individual modelling parameters deal with humidity, angular speed and ambient temperature. These three entities are varied in our measurements, inside the testing working range. The individual modelling parameters are optimised for each parameter variation, leaving the global parameters constant. This is the second optimisation, comprising the humidity, angular speed and temperature variation.
Fig 5.4 shows the optimisation scheme, beginning with the global parameter optimisation. This first optimisation stage deals with the calculation of the best global parameter values in order to adjust the parameters value to a real measurement. Thus, the optimal spot radius, ellipticity and C_{glob} are found and classified for next optimisations as constant. Afterwards, three different optimisations are accomplished, one for each parameter variation (temperature, relative humidity and angular speed). On each optimisation phase, the previous already optimised parameters are handled as constant parameters. After all these optimisation phases, Table 5.2 is obtained.

Description	Parameter name	Value
spot radius	a	13 µm
Ellipticity	γ	5
Global thickness	C_{glob}	2.4
Angular speed coefficient	C_n	0.0012
Angular speed exponent	P_n	0.69
Humidity Coefficient	C_H	102.16
Relative humidity exponent	P_H	6
Temperature Coefficient	C_T	2.2
Temperature exponent	P_T	10

Table 5.2: Parameter values of the final model.

Table 5.2 shows the final optimised values. After optimising each parameters set, a final simulation loop was done in order to compare the results with the optimised values.
To summarise, a hierarchical optimisation is performed, addapting the simulation to the measurements. the internal variables of the model are always inside real ranges. These real ranges are based direct or indirect (through calculation) on the bibliographic sources. Some of the results are explained in the next section.

5.5 Model Validation

Now there is an optimised model for the three observed tendencies. A growing relative humidity increases the voltage drop. Also a growing ambient temperature increases the voltage drop. Finally, a growing angular speed decreases the voltage drop. This last tendency has a non linear behaviour as the measurements. All these tendencies are generated by the model.
This model behaves correctly in the optimisation range but what happens in the whole measurements range. The measurements range has to be checked and the error between measurements and simulation computed.
In the modelling stage the optimised range was also tested. However, this doesn't prove the validity of the model in all the test range. Thus, different test points were checked on the boundary corners of the test range (Fig. 5.5). These points have not to be arbitrary, because the system parameters have not the same importance. This importance is measured in the effect of the parameter in the voltage drop. For example, the angular speed has the biggest effect on the voltage drop, and the ambient temperature has the smallest effect on the voltage drop. Thus, the angular speed has the biggest

importance in our test range.
Therefore, the program cornerstone was used to generate the test points. This program uses the parameters of a system and a classification of them to generate the test points. Then, it generates a list of representative points, by which the system can be checked.
The user has to give the dependency of the measured magnitude with the parameters to the program. Also the measured parameter ranges has to be given. With this information the program can calculate where the measured quantity has to be tested in order to have a checked range. The given dependencies are a linear dependency for relative humidity and ambient temperature, and a quadratic dependency for the angular speed.
The points were generated and tested. A relative error was defined as

$$\%E = \frac{\text{Simulated\_value} - \text{Measured\_value}}{\text{Simulated\_value}} \tag{5.16}$$

The mean relative error was about 5%. Thus, the model was validated inside the measuring range.

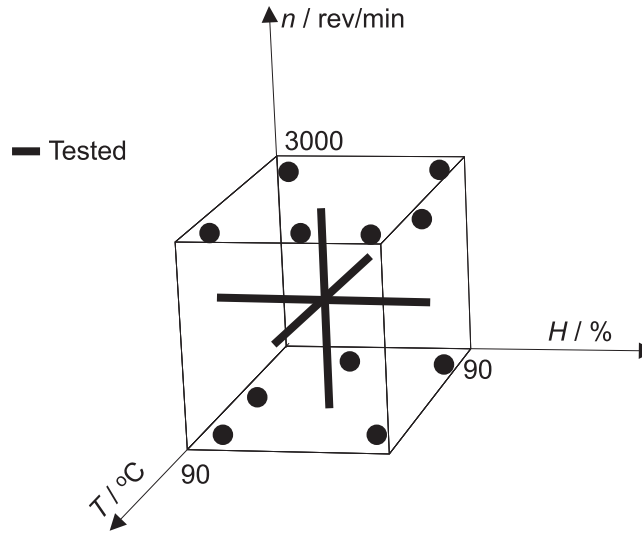

Fig. 5.5: Three-dimensional space of the test range.

5.6 Comparison between Experiments and Simulations

In this section, the results of the optimisation are given. Different UI-curves will be presented, each one having two different components: measured data and simulated data. The order of presentation will be the one used to reach the complete parameter optimisation data. In each UI-curve, there will be measured and simulated, allowing us to compare both results. The measured curves will be presented with symbols without lines connecting the different points. The optimised model curves will be presented with empty symbols connected by lines. For each optimisation phase a UI-curve is given.
In our test bench, the voltage drop between both brushes is measured. The implemented circuit is used for the two contacts (anode and cathode), connected in a serial mode. In a real contact the voltage drop in a cathode and in an anode is different. This difference comes from the different oxide thickness and oxide composition. In our test bench, this polarity difference could not be measured because of the complexity of the ground-rotor connection. Thus, this circuit of two resistances will bring us no extra results as we cannot measure the individual brush-rotor voltage drop. The adopted solution was to implement a circuit with only one contact resistance. This solution brings us a simplified optimisation circuit. Then, the measured voltage drop was divided by two, and then compared with our model results. The parameters become simplified, achieving better parameter values.

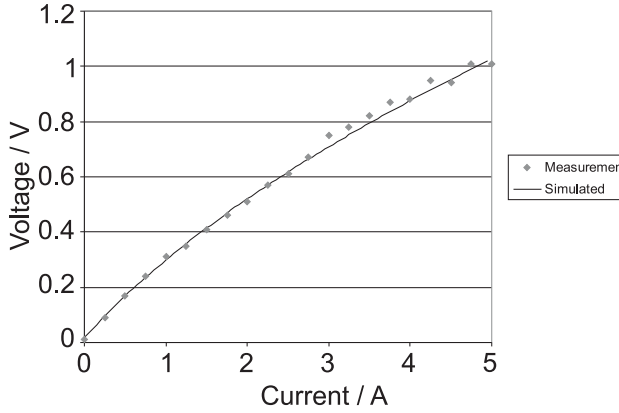

Fig. 5.6: Global parameter optimisation.

The global parameters have to be determined as first step for the model optimisation. The first optimisation attempt was done with an UI-curve without ambient temperature, humidity or angular speed variation. Fig. 5.6 shows this first attempt, depicting the measured and modelled curves. The measurement was done with an angular speed of 2000 rpm, an ambient temperature of 50 ℃, and a relative humidity of 50 %. The optimised parameters were spot radius, ellipticity and C_{glob}. The initial values were a spot radius of 5 µm, an ellipticity of 3, and a C_{glob} of 1. A first sensibility analysis was done in order to set the optimisation priority. The optimisation was done, achieving a good curve fitting. Fig. 5.6 shows that the fitted line is sometimes over and sometimes below the measured data, but a good general agreement is reached. The parameter values correspond to the ones in Table 5.2.
Fig. 5.7 shows one example of modelled UI-curve with the angular speed as parameter. The humidity value was 50 % and the temperature was 50 ℃. The lines with an empty symbol correspond to the simulation curves. The symbols without line correspond to the measurement curves. A parameter value always agrees with the same symbol, differing only in the symbol filling depending on the measured or simulated curve. For example the circle corresponds always to an angular speed of 3000 rpm, while a square corresponds

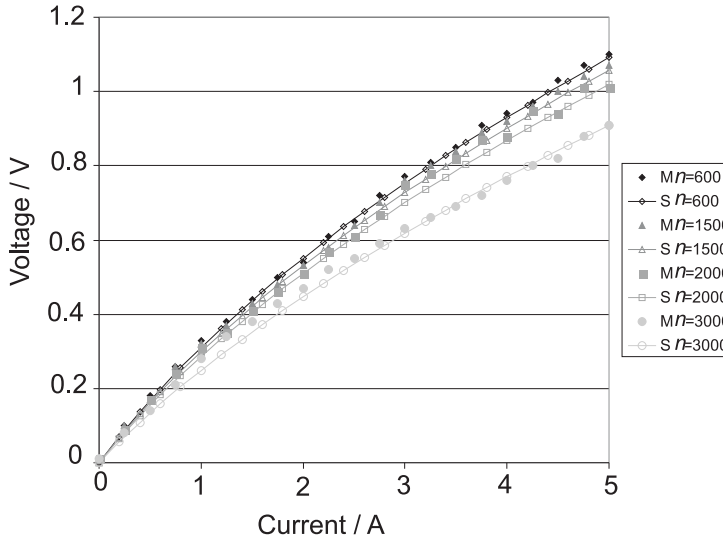

Fig. 5.7: Modelation of the UI-curve with the angular speed as parameter.

always to an angular speed of 2000 rpm. The optimised parameter were C_n and P_n, remaining all the other parameters constant. With these values, the simulated UI-curves behave as the measured values. Thus, it could be concluded that the speed optimisation is accomplished.
Continuing with the optimisation procedure Fig. 5.8 shows one example of modelled UI-curve with the relative humidity as parameter. The ambient temperature was 50 ˚C, and the angular speed was 2000 rpm. The schedule of the graphic is the same as in Fig. 5.7. The optimised parameters were on this case C_H and P_H, remaining all the other parameter values preserved. A growing relative humidity increases the voltage drop, as it was concluded in section 4.4.2.1. After the optimisation, C_H becomes 102.16 and P_H becomes 6. With this configuration, the voltage drop range of the modelling curves is the same of the measured curves. Furthermore, the tendency of the relative humidity can be seen on the optimised values.
The fourth optimisation step deals with the ambient temperature as parameter, Fig. 5.9 shows one example of modelled UI-curve in comparison to the measurement data. The measurements were done with a relative humidity of 50 % and an angular speed of 2000 rpm. The variation range of the ambient temperature is from 20 ˚C to 80 ˚C. The schedule of the graphic is the same as in Fig. 5.7. The optimised parameter were C_T and P_T, remaining

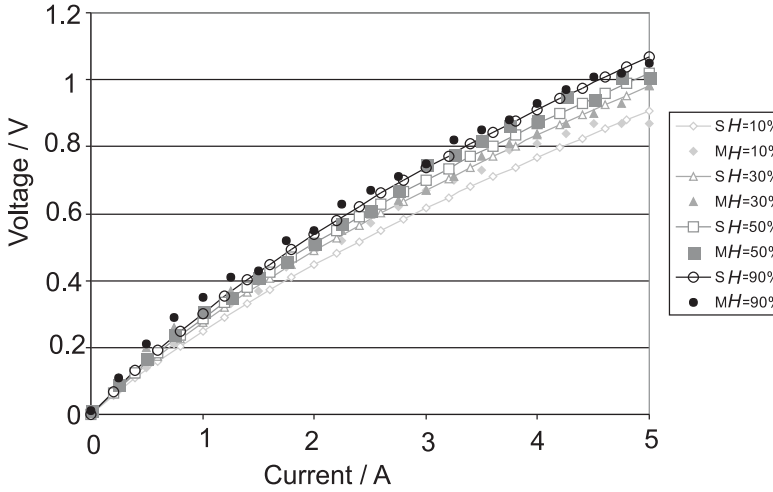

Fig. 5.8: Modelation of the UI-curve with the relative humidity as parameter.

all the other parameter constant. After the optimisation, C_T is 2.2, and P_T is 10. The optimised values show a clear temperature tendency, following the measured values.
Finally, the variation ranges of all the parameters were implemented, achieving a model with a good parameter description. At this point the last optimisation step is done, a simulation without optimisation is done for all the optimised ranges in order to test the simulation with the final parameter set. As a final presentation, Fig. 5.5 shows the experimental range as a cube. The rectangular space is characterised by three axes, differing in their magnitude. The axes are ambient temperature as x-axis, relative humidity as y-axis, and angular speed as z-axis. Thus, a space point is described as (T, H, n). The origin of the system is the (10, 10, 600) point as this point is the minimum test range. The tested range extends itself as a three-dimensional cross from each minimum parameter value till each maximum parameter value. The middle point of the cross corresponds to an angular speed of 1500 rpm,

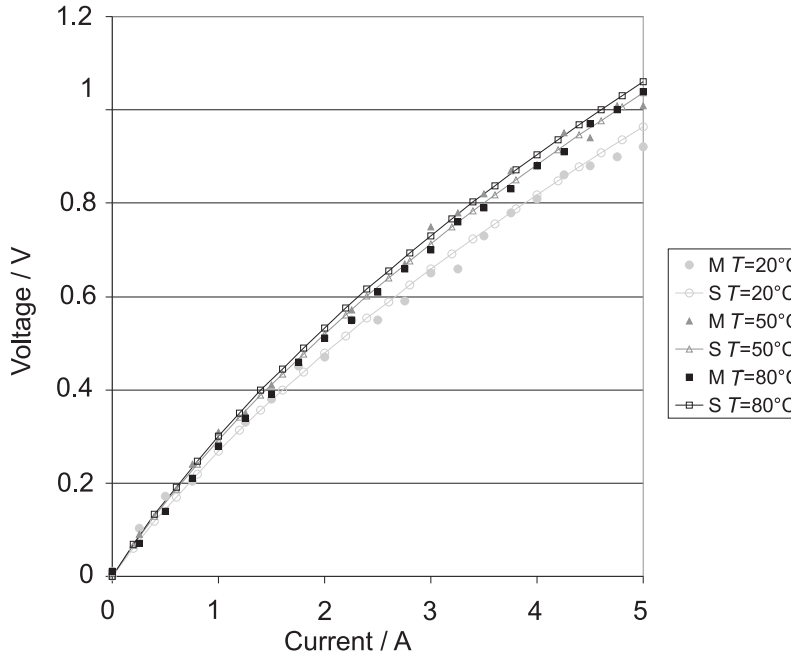

Fig. 5.9: Modelation of the UI-curve with the ambient temperature as parameter.

an ambient temperature of 50 °C, and a relative humidity of 50 %. The presented curves maps a cross (Fig. 5.5), demonstrating a good measurement modelling.
The observed tendencies are implemented in the model inside the oxide thickness equation. The temperature and humidity influences are related with the oxidation effect, increasing the oxide thickness. The angular speed influence is related to the clearing effect, decreasing the oxide thickness. Both effects are introduced in the oxide thickness equation, having the corresponding voltage drop effect. The developed model shows a good prediction of the measured curves, having the ambient temperature, relative humidity and angular speed as parameter.

Chapter 6

Conclusions

The aim of this work is the theoretical and experimental investigation of a sliding contact, regarding the influences of different environmental parameters in a commercial system.
For this aim, the different principles of the constriction contact theory, which extends over the last 80 years, are analysed and evaluated. The evaluation has been performed with a numerical simulator (FEM), comparing the analytical constriction equations with the numerical results. An experimental set-up has been developed to measure the transient constriction resistance under defined environmental conditions like temperature, humidity and angular speed. This was achieved by using a climate chamber and an external controlled motor. The experimental set-up has been automatised in order to assure the test reproducibility and efficiency. Systematic measurements are carried out regarding temperature, humidity and angular speed as parameters. The measurement results show dependencies of the constriction resistance on these varied parameters.
Based on these results and on the constriction theory, a model has been developed which predicts the contact resistance with the observed dependencies. The contact resistance is described by an equivalent circuit of different ohmic resistances. Each resistance represents a particular physical effect present on the sliding contact.
Most of the resistances are given by defined equations. Only a few of them are based on empirical descriptions, so these equations still have grades of freedom. To adjust the model to the measurement results, these free parameters have been optimised in a hierarchical process. On this way, a very good agreement between measurements and modelled results could be achieved.
A probable extension of the research will deal with different other aspects

that could improve the constriction model. The model allows us to vary the contact load, so one extension is to implement another test bench, which controls its variation. In addition, different chemical compose does not react equal to different environmental situations. Thus, one improvement is to model other types of brushes. Another potential extension comes from the polarity effect. The composition and geometry of the oxide in cathode and anode is not the same, and possibly, they will not react equal to variations of the environmental parameters. Thus, a new project extension is to implement a new test bench within the voltage drop in anode and cathode could be measured separately. Another possibility will be the test of a rotor with lamellas, as they are need in real DC motors.

To summarise, the useful facts are the design of reliable motors and a quicker material classification. The prediction of the voltage drop in the brushes allows controlling the behaviour of the electric motor in different environments. This knowledge is also profitable in the prediction of the brushes wear in different climatic zones and operation modes. The brushes wear is the key parameter in the electric motor life. Or in other words, it is the cause of most of the electric motor failures. Another improvement is the quick test of different brush materials. By changing the material properties and adjusting the model parameters, the effect of this material change can be predicted by the model.

One of the concrete facts is to clarify the environmental influences and to perform a first step in a new sliding contact model. The environmental influences actuate over different contact parameters, having sometimes contrary effects. The performance of the sliding contact was not clear in the previous research works. Thus, the exact performance of the system below different environments is now clarified. Not only the systems performance is clarified, but the cause of this effect is clarified and modelled. These environmental conclusions can be used to design better electric motors in the future. A second concrete fact is the verification of the constriction theory, becoming an interesting new approach for the sliding contacts. It is an approach based on the physical effects present on the sliding contact, so with the inclusion of more effects, as the contact polarity, this contact model can finally describe the commercial sliding contact.

Bibliography

[1] W. H. Abbott. The Corrosion of Copper and Porous Gold in Flowing Mixed Gas Environments. *IEEE transactions on Components. Hybrids, and Manufacturing Technology*, 13(1): 40–45, March 1990.

[2] William H. Abbott. The Development and Performance Characteristics of Mixed Flowing Gas Test Environment. *IEEE transactions on Components. Hybrids, and Manufacturing Technology*, 11(1): 22–34, March 1988.

[3] David C. Baird. *Experimentation: An Introduction to Measurement Theory and Experiment Design, 3/E.* Prentice-Hall, 1995.

[4] Yang Baitun, Liufu De, Tu Demin, and Liu Yaonan. Breakdown mechanism of the charged solid dielectric during short circuit discharge. *Proceedings of the 3rd International Conference on properties and applications of dielectric materials*, pages 1048–1051, July 1991.

[5] J. R. Barber. Bounds on the electrical resistance between contact in elastic rough bodies. *Proc. Royal Society*, A(459): 53–66, 2003.

[6] V. A. Belyi, N. K. Myshkin, M. I. Petrokovets, A. I. Sviridenko, and S. A. Chizhik. The influence of the solid-contact surface characteristics on its electrical conductivity. *Phys. Chem. Mech. Surfaces*, 5(6): 1500–1513, 1990.

[7] Ake Öberg and Jan Isberg. Simulations of Transient Thermal and Electrical Behavior of Contact Spots. *Proceedings of the Forty-Fifth IEEE Holm Conference on Electrical Contacts*, pages 141 – 145, October 1999.

[8] M. Beyer, W. Boeck, K. Möller, and W. Zaengl. *Hochspannungstechnik*, chapter Flüssige und feste Isolierstoffe, pages 178–183. Springer-Verlag, 1986.

[9] Kurt Binder. Beitrag zur Dynamik des Kontakts Kohlebürste - Lamelle. *ETZ-A*, 82(2): 46–53, 1961.

[10] Kurt Binder and Dieter W. Heermann. *Monte Carlo Simulation in Statistical Physics*. Solid-State Sciences. Springer-Verlag Berlin Heidelberg, 3 edition, 1997.

[11] F. P. Bowden and D. Tabor. *The Friction and Lubrication of Solids*. Oxford University Press, 1954.

[12] F. P. Bowden and D. Tabor. *The Friction and Lubrication of Solids*, volume 2. Oxford University Press, 1964.

[13] F. P. Bowden and D. Tabor. *The Friction and Lubrication of Solids*. Oxford University Press, 1986.

[14] F. P. Bowden and J. B. P. Williamson. Electrical conduction in solids I. influence of the passage of current on the contact between solids. *Proc. Royal Soc.*, 246(A): 1–12, 1958.

[15] Lionel Boyer. Contact resistance calculations: generalizations of Greenwood's formula including interface films. *IEEE Transactions on Components and Packaging Technologies*, 24(1): 50 – 58, March 2001.

[16] P.P. Budenstein. Toward developing a dynamic theory of electric breakdown in solids. *Conduction and Breakdown in Solid Dielectrics*, pages 522–527, 1989.

[17] Ralph A. Burton and R. gaines Burton. Cooperative interactions of asperities in the thermotribology of sliding contacts. *Proceedings of the Thirty-Sixth IEEE Holm Conference on Electrical Contacts and the Fifteenth International Conference on Electrical Contacts*, 20-24: 256 – 258, August 1990.

[18] M. H. Cocks. *The effect of compressive and shearing forces on the alien films present in metallic contacts*. PhD thesis, The University of Reading, May 1953.

[19] R. Degraeve, G. Groeseneken, R. Bellens, M. Depas, and H.E. Maes. A consistent model for the thickness dependence of intrinsic breakdown in ultra-thin oxides. *Electron Devices Meeting*, pages 863–866, 1995.

[20] Michel Depas, Tanya Nigam, and Marc M. Heyns. Soft Breakdown of Ultra-thin gate Oxide Layers. *IEEE Transactions on Electron Devices*, 43(9): 1499–1504, September 1996.

[21] Sara Dillich and Doris Kuhlmann-Wilsdorf. Two Regimes of Current Conduction in Metal-Graphite Electrical Brushes and Resulting Instabilities. *IEEE Transaction on Components, Hybrids, and Manufacturing Technology*, CHMT-6(1): 45–54, March 1983.

[22] D. J. Dumin. *Oxide Reliability: a summary of silicon oxide wearout, breakdown, and reliability.* World Scientific Publishing Co. Pte. Ltd., 2002.

[23] J. Dyson and W. Hirst. The True Contact Area Between Solids. *Proceedings of the Physical Society*, 67: 309–312, 1954.

[24] Donald G. Fink and Donald Christiansen. *Electronics Engineers' Handbook*, chapter Dielectric and insulating materials, pages 6–33 to 6–34. Mcgraw-Hill Book company, second edition, 1988.

[25] Prof. Dr. Helmut Föll. Electronic materials. Technical report, Christian-Albrechts-Universität zu Kiel, www.tf.uni-kiel.de/matwis/amat/elmat_en/index.html, 1999.

[26] Chao Gao and Doris Kuhlmann-Wilsdorf. Absorption Films, Humidity, Stick-Slip, and Resistance of Sliding Contacts. *IEEE Transactions on Components, Hybrids, and Manufacturing Technology*, 14(1): 37–44, March 1991.

[27] E. W. Glossbrenner. The life and times of an a-spot. *Proceedings of the thirty-Eighth IEEE Holm conference*, pages 171–177, October 1992.

[28] Robert Bosch GmbH. *Kraftfahrtechnisches Taschenbuch.* Verlagsgesellschaft mbH, 23 edition, 1999.

[29] Dwight E. Gray. *American Institute of Physics Handbook.* McGraw-Hill Book Company, 2nd edition, 1963.

[30] J. A. Greenwood. Constriction resistance and real area of a contact. *Brit. J. Applied Physics*, 17: 1621–1632, July 1966.

[31] J. A. Greenwood and J. B. P. Williamson. Electrical conduction in solids II. theory of temperature-dependent conductors. *Proceedings Royal Society*, 246: 13–31, 1958. Series A.

[32] Jin Jin Gu, Keith Warner, Shu Qin, and Chung Chan. Constriction Resistance of Microcone-Based Contacts. *IEEE Transactions on components packaging, and manufacturing technology*, 18(2): 385–389, June 1995.

[33] Ragnar Holm. Über metallische Kontaktwiderstände. *Wissenschaftliche Veröffentlichungen aus dem Siemens-Konzern*, 7: 217–271, 1928-1929. Verlag von Julius Springer in Berlin.

[34] Ragnar Holm. *Electric Contacts: Theory and applications*. Springer-Verlag, 4th edition, 1967.

[35] Chenming Hu and Qiang Lu. A unified gate oxide reliability model. *IEEE international reliability physics symposium*, pages 47–51, 1999.

[36] Erle I. Shobert II. *Carbon Brushes: The Physics and Chemistry of Sliding Contacts*. Chemical publishing company Inc, New York, 1965.

[37] Erle I. Shobert II. Sliding Electrical Contacts. *Proceedings of the Thirty-Ninth IEEE Holm Conference on Electrical Contacts*, pages 123–134, September 1993.

[38] J. L. Johnson and J. Schreurs. High current brushes viii: Effect of electrical load. *wear*, 1-2(78): 219–232, 1982.

[39] John L. Johnson. Sliding monolithic brush systems for large currents. *Electrical Contacts*, October 1986.

[40] Kenichi Kataoka, Toshihiro Itoh, and Tadatomo Suga. Characterization of fritting phenomena on a electrode for low contact force probe card. *IEEE transactions on components and packaging technologies*, 26(2): 382–387, June 2003.

[41] A. Keil, W. A. Merl, and E. Vinaricky. *Elektrische Kontakte und ihre Werkstoffe*. Springer, 1984.

[42] F. Kottler. *Elektrostatik der Leiter. Handbuch der Physik von Veiger und Scheel*, volume 12, pages 14–15. Springer, Berlin, 1927.

[43] I. V. Kragelskii and N. B. Demkin. Determination of the true contact area. *Friction and wear in machinery*, 14: 30–53, March 1960.

[44] Doris Kuhlmann-Wilsdorf and David D. Makel. On the two modes of Operation of monolithic Ag-c brushes. *Proceedings of the Thirty Fourth Meeting of the IEEE Holm Conference on Electrical Contacts*, pages 213–222, September 1988.

[45] D. K. Lawson and T. A. Dow. The sparking and wear of high current density electrical brushes. *Wear*, 102: 105–125, 1985.

[46] H. C. Lin, D. Y. Lee, C. Y. Lee, T. S. Chao, T. Y. Huang, and T. Wang. New Insights into Breakdown Modes and Their Evolution in Ultra-Thin Gate Oxide. *International Symposium on VLSI Technology*, pages 37–40, 2001.

[47] Horng-Chih Lin, Da-Yuan Lee, and Tiao-Yuan Huang. Breakdown Modes and Their Evolution in Ultrathin Gate Oxide. *Japanese Journal of Applied Physics*, 1(10): 5957–5963, October 2002.

[48] L. R. Ludwid and R. M. Baker. Influence on Commutation of Brush Contact Drop. *Transactions of the AIEE*, 51: 959–965, 1932.

[49] Robert D. Malucci. Dynamic Model of Stationary Contacts Based on Random Variations of Surface Features. *IEEE Transactions on components, Hybrids, and Manufacturing Technology*, 15(3): 339–347, 1992.

[50] Nancy R. Mann, Ray. E. Schafer, and Nozer D. Singpurwalla. *Methods for Statistical Analysis of Reliability and Life Data.* Wiley series in Probability and Mathematical Statistics. John Wiley & Sons, 1974.

[51] James Clerk Maxwell. *A Treatise on Electricity and Magnetism*, volume 1 of *Oxford Classics Series.* Oxford Universtiy Press, 2 edition, 1998.

[52] Martin Mayr and Ulrich Thalhofer. *Numerische Lösungsverfahren in der Praxis: FEM BEM FDM.* Studienbücher der technischen Wissenschaften. Carl Hansen Verlag, 1993.

[53] Udo F. Meißner and Andreas Maurial. *Die Methode der finiten Elemente.* Springer, 2 edition, 2000.

[54] Günter Müller and Clemens Groth. *FEM für Praktiker - Band 1: Grundlagen.* Expertsoft 23 Edition. Expert Verlag, 7 edition, 2002.

[55] Mitsunobu Nakamura and Isao Minowa. Computer Simulation for the Conductance of a Contact Interface. *IEEE transactions on components, Hybrids, and Manufacturing technology*, CHMT-9(2): 150–155, June 1986.

[56] H. Nishiyama and I. Minowa. A Study of the Approximate Expressions for Constriction Resistance of Multitude Conducting Spots. *IEICE Trans. Electron.*, E82-C(1): 25–32, January 1999.

[57] Eberhard Paulig. *Der Kohlebürstengleitkontakt im Elektromaschinenbau.* PhD thesis, Technishen Universität Dresden, Juli 1980.

[58] K. Prasad, X. L. Yuan, C. Y. Li, and Rakesh Kumar. Evaluation of diffusion barrier layers in Cu interconnects. *Conference on Optoelectronic and Microelectronic Materials and Devices*, pages 373 – 376, December 2002.

[59] James Prendergast, John Suehle, Prasad Chaparala, Eammon Murphy, and Malcom Stephenson. TDDB Characterisation of Thin SiO_2 Films with Bimodal Failure Populations. *IEEE International Reliability Physics Symposium Proceedings*, 4-6: 124–130, April 1995.

[60] E. M. Pugh and G. H. Winslow. *The Analysis of Physical Measurements*. Addison-Wesley, 1966.

[61] D. Qian and D. J. Dumin. The Electric Field, Oxide Thickness, Time and Fluence Dependences of Trap Generation in Silicon Oxides and Their Support of the E-model of Oxide Breakdown. *Proceedings of the 1999 7th International Symposium on the Physical and Failure Analysis of Integrated Circuits*, pages 145–150, July 1999.

[62] Ernest Rabinowicz. The Temperature Rise at Sliding Electrical Contacts. *Wear*, 78: 29–37, 1982.

[63] Markus Rolfes. Untersuchung der Patina auf den Schleifringen von Kfz-Generatoren. Diplomarbeit 1442078, Univertität Hannover, Institut für Elektrische Maschinen und Antriebe, July 1997.

[64] M. Runde, E. Hodne, and B. Tøtdal. Experimental Study of the Conducting Spots in Aluminium Contact Interfaces. *IEEE Transactions on Components, Hybrids, and Manufacturing Technology*, 13(4): 1068 – 1073, 1990.

[65] M. Runde, Helge Kongsjorden, and B. Tøtdal. Detection of a-Spots in Aluminum Contacts. *IEEE Transactions on Components, Hybrids, and Manufacturing Technology*, CHMT-9(1): 77–85, March 1986.

[66] George J. Russ. Electrical Characteristics of Contacts Contaminated with Silver Sulfide Film. *IEEE Transactions on Parts, Materials and Packaging*, 6(4): 129–137, December 1970.

[67] G. V. Samsonov. *The Oxide Handbook*. Plenum Data Corporation, 1973.

[68] J. Schreurs and J. L. Johnson. Characterization of Thick films formed on Slip Rings During High Current Density Operation. *IEEE Transaction on Components, Hybrids and Manufacturing Technology*, CHMT-4(1): 30–35, March 1981.

[69] Klaus F. Schuegraf and Chenming Hu. Hole Injection SiO_2 Breakdown Model for Very Low Voltage Lifetime Extrapolation. *IEEE Transactions on Electron Devices*, 41(5): 761–767, 1994.

[70] Schunk & Ebe GmbH Gießen. *Kohlebürsten : Untersuchungsergebnisse Erfahrungen Empfehlungen*, 1980.

[71] Paul G. Slade. *Electrical Contacts; Principles and Applications*. Marcel Dekker, Inc., http://www.dekker.com, 1999.

[72] William R. Smythe. *Static and Dynamic Electricity*. International Series in Pure and Applied Physics. New York: McGraw-Hill, 2 edition, 1968.

[73] J. H. Stathis. Physical and predictive models of ultra thin oxide reliability in CMOS devices and circuits. *39 Annual International Reliability Physics Symposium*, pages 132–149, 2001.

[74] Jordi Suñé. New Physics-Based Analytic Approach to the Thin-oxide Breakdown Statistics. *IEEE Electron Device Letters*, 22(6): 296–298, June 2001.

[75] J.R. Taylor. *An Introduction to Error Analysis: The Study of Uncertainties in Physical Measurements*. University Science Books, 2 edition, 1996.

[76] S. P. Timoshenko and J. N. Goodier. *Theory of Elasticity*. Engineering Societies Monographs. McGraw-Hill Book Company, 3rd edition, 1970.

[77] R. S. Timsit. Electrical contact resistance: properties of stationary interfaces. *IEEE Transactions on Components and Packaging Technologies*, 22(1): 85–981, March 1999.

[78] Roland S. Timsit. On the evaluation of contact temperature from potential-drop measurements. *IEEE Transactions on Components, Hybrids, and Manufacturing Technology*, CHMT-6(1): 115–121, 1983.

[79] Roland S. Timsit. Electrical instabilities in stationary contacts: Al/plated-brass junctions. *IEEE Transactions on Components, Hybrids, and Manufacturing Technology*, 11(1): 43 – 53, March 1988.

[80] T. Ueno, N. Morita, and K. Sawa. Influence of Surface Roughness on Voltage Drop of Sliding Contacts under Various Gases Environment. *Proceedings of the Forty-Ninth IEEE Holm Conference on Electrical Contacts*, pages 59–64, September 2003.

[81] G. K. White and M. L. Minges. Thermophysical properties of some key solids: An uptate. *Int. J. Thermophys.*, 18(5): 1269 – 1327, 1997.

[82] Zbigniew Zlonkiewicz. The performance analysis of low - current contacts modelled by numerical methods. *Proceedings of 20th International Conference on Electrical Contact ICEC*, pages 251–254, June 2000.

Appendix A

The A_c Equation

This appendix has been added in order to clarify the equation 2.26, and the explanation presented in section 5.3.1. The Eq. 2.26 is not intuitive, because the relation is as follows

$$A_{c,tot} = \frac{L}{H_m} \qquad \equiv \qquad A_{c,tot} \neq f(A) \quad , \tag{A.1}$$

where $A_{c,tot}$ is the total contact area, A is the apparent contact area, L is the applied load, and H_m is the hardness of the softer material in the contact. The clarification will be done by using two different contacts with two different apparent contact areas A_1 , A_2 respectively (Fig. A.1). If we prove that the total contact areas of the two contacts are equal, then the Eq. 2.26 is correct.

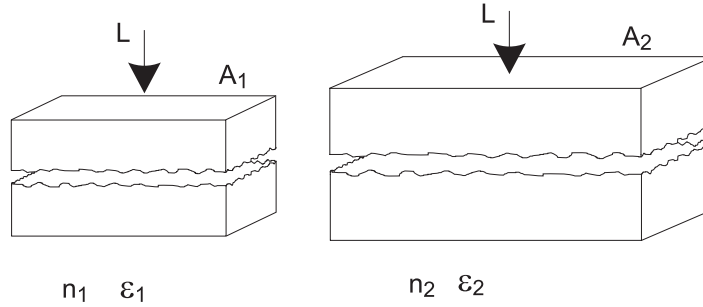

Fig. A.1: Two contacts with different areas, number of spots and waviness.

The situation is the presence of two physical contacts, having each contact an apparent area of A_1 and A_2. Both contacts happen between the same materials. Fig A.1 shows both contacts with their related dimensions. Both contacts are pressed by a load L, and both have a respective density of spots n_1 and n_2, and a waviness of ε_1 and ε_2 .
In order to follow with the demonstration, all the magnitudes will be equal except the apparent areas, so we are in the situation:

- waviness ε_1 and ε_2 and both are equal

$$\Rightarrow \varepsilon_1 = \varepsilon_2 \quad , \tag{A.2}$$

- the density of spots is the same

$$n_1 = n_2 = n \quad . \tag{A.3}$$

With this situation on each contact, Z_i is the number of spots in the respective area of contact. The number of spots on each contact is

$$Z_1 = n_1 \cdot A_1 = n \cdot A_1 \quad \text{, and} \tag{A.4}$$
$$Z_2 = n_2 \cdot A_2 = n \cdot A_2 \qquad , \tag{A.5}$$

where A_1 and A_2 are the apparent areas of each contact. Dividing both equations, the result is

$$Z_2 = Z_1 \cdot \frac{A_2}{A_1} \quad . \tag{A.6}$$

As the load L is distributed on the Z_i spots, and these spots are equal in dimensions, the spot load in both contacts is

$$F_i = \frac{L}{Z_i} \quad . \tag{A.7}$$

In order to be more explicit, the spot loads for each contact are

$$F_1 = \frac{L}{Z_1} \quad \text{and} \quad F_2 = \frac{L}{Z_2} \quad . \tag{A.8}$$

The respective true contact areas are $A_{c,tot,1}$ and $A_{c,tot,2}$, and they are described by

$$A_{c,tot,1} = Z_1 \cdot \pi \, \overline{a}_1^2 \, , \text{ and} \tag{A.9}$$
$$A_{c,tot,2} = Z_2 \cdot \pi \, \overline{a}_2^2 \, , \tag{A.10}$$

where $\overline{a}_1$ is the mean spot radius in the contact 1, and $\overline{a}_2$ is the mean spot radius in the contact 2. It is generally accepted that the true contact area is controlled by the plastic deformation of the surface asperities of the softer material [34, 71, 30, 13]. Under this assumption, the total area of mechanical contact $A_{c,tot}$ is related to the load L as follows

$$A_{c,tot} = \frac{L}{H_m} \quad , \tag{A.11}$$

where H_m is the hardness of the softer material of the contact. Applying Eq. A.11 to the first contact, it is transformed by using Eq. A.9 and Eq. A.8 as follows

$$Z_1 \cdot \pi \overline{a}_1^2 = \frac{Z_1 F_1}{H_m} \tag{A.12}$$

$$\iff \quad \pi \overline{a}_1^2 = \frac{F_1}{H_m} \tag{A.13}$$

$$\iff \quad \pi \overline{a}_1^2 = \frac{L}{Z_1 \cdot H_m} \tag{A.14}$$

$$\iff \quad \pi \overline{a}_1^2 = \frac{L}{n \cdot A_1 \cdot H_m} \quad . \tag{A.15}$$

Eq. A.15 is true for both contacts changing 1 indexes to 2 indexes. Including Eq. A.15 and A.4 into Eq. A.9, we find

$$A_{c,tot,1} = \frac{L}{H_m} \quad . \tag{A.16}$$

Thus, the contact area of the contact 1 does not depend on its apparent contact area. Since we obtain Eq. 2.26, we can conclude that the assumption was true.
In addition, we are going to demonstrate that both contact areas are equal. To demonstrate this, the contact area in one spot is

$$A_{c,1} = \pi \cdot \overline{a}_1^2 = \frac{F_1}{H_m} \quad \text{and} \quad A_{c,2} = \pi \cdot \overline{a}_2^2 = \frac{F_2}{H_m} \quad , \tag{A.17}$$

where $\pi \cdot \overline{a}_i^2$ is the area of one spot in contact i, as well as $A_{c,i}$. Applying Eq. A.8 and A.6, the force on each spot is

$$F_1 = \frac{L}{Z_1} = \frac{L}{\frac{A_1}{A_2} \cdot Z_2} \quad . \tag{A.18}$$

Thus, the interaction of Eq. A.17 results in

$$A_{c,1} = \frac{L}{H_m \cdot \frac{A_1}{A_2} \cdot Z_2} \quad \text{, and} \quad A_{c,2} = \frac{L}{Z_2 \cdot H_m} \quad . \tag{A.19}$$

Now, dividing the two functions we obtain

$$\frac{A_{c,1}}{A_{c,2}} = \frac{L \cdot A_2}{A_1 \cdot Z_2 \cdot H_m} \cdot \frac{Z_2 \cdot H_m}{L} = \frac{A_2}{A_1} \quad . \tag{A.20}$$

If we calculate the total areas of contact applying Eq. A.6, the relation is

$$A_{C,tot,1} = Z_1 \cdot A_{c,1} = Z_1 \cdot \frac{A_2}{A_1} \cdot A_{c,2} = Z_2 \cdot A_{c,2} = A_{c,tot,2} \quad . \tag{A.21}$$

The final expression is

$$A_{c,tot,1} = A_{c,tot,2} = \frac{L}{H_m} \quad . \tag{A.22}$$

Finally, the contact areas are the same in both cases, even if each case has a different apparent area. Thus, the Eq. 2.26, and the explanation presented in section 5.3.1 are correct.

Lebenslauf

Marcos Fraile Gomez

Geburtsdatum:	24.05.1975
Geburtsort:	Huesca, Spanien

Ausbildung:

1980 - 1989	Volksschule San Vicente de Paul Palma de Mallorca
1989-1993	Gymnasium Instituto Politècnic de Mallorca Palma de Mallorca
1993-1999	Studium der Physik Universitat Autònoma de Barcelona Abschluss: Diplom
1995-1998	Studium der Elektrotechnik Universitat Autònoma de Barcelona Abschluss: Diplom
2000-2001	Studium der Elektrotechnik Universität Autònoma de Barcelona Abschluss: Master